CZECH TECHNICAL UNIVERSITY IN PRAGUE

Faculty of Electrical Engineering

Department of Cybernetics

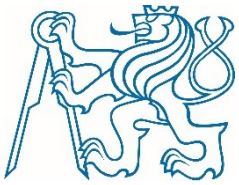

Study Program: Biomedical Engineering and Informatics

Specialization: Biomedical Informatics

Diploma Thesis

RELATIONSHIP OF HEART'S PUMPING FUNCTION AND PRESSURE-FLOW PATTERNS IN REDUCED ARTERIAL TREE

Student: Karel Kalecký

Supervisor: Ing. Filip Ježek

Žďár nad Orlicí 2015

ČESKÉ VYSOKÉ UČENÍ TECHNICKÉ V PRAZE

Fakulta elektrotechnická

Katedra kybernetiky

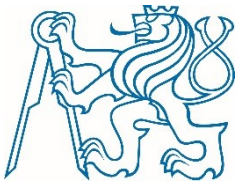

Studijní program: Biomedicínské inženýrství a informatika

Studijní obor: Biomedicínská informatika

Diplomová práce

ZÁVISLOST ČERPACÍ FUNKCE SRDCE NA TLAKOVÝCH A TOKOVÝCH POMĚRECH V ARTERIÁLNÍM STROMĚ

Student: Karel Kalecký

Vedoucí: Ing. Filip Ježek

Žďár nad Orlicí 2015

Czech Technical University in Prague
Faculty of Electrical Engineering

Department of Cybernetics

DIPLOMA THESIS ASSIGNMENT

Student: Bc. Karel K a l e c k ý

Study programme: Biomedical Engineering and Informatics

Specialisation: Biomedical Informatics

Title of Diploma Thesis: Relationship of Heart's Pumping Function and Pressure-Flow Patterns in Reduced Arterial Tree

Guidelines:

- Sum available models of pulsatile heart mechanics and heart's revolution and power.
- Develop a simplified mathematical model of heart's pulsatile mechanics, based on availiable models.
- Create a simplified mathematical model of arterial tree with at least first level of branching.
- Connect those two models, evaluace its validity and use it to study the effect of VA ECMO setting on pulsating heart.
- Discuss other usage possibilities and extensions to simulating patological states (vascular stenosis, constriction or rigidity, heart failure etc.)

Bibliography/Sources:

[1] Pironet, Antoine et al. Simulation of Left Atrial Function Using a Multi-Scale Model of the Cardiovascular System. PLoS ONE, 2003.
[2] Lumens, Joost et al. Three-Wall Segment (TriSeg) Model Describing Mechanics and Hemodynamics of Ventricular Interaction. The Journal of the Biomedical Engineering Society, 2009.
[3] Stergiopulos, Nikos et al: Total arterial inertance as the fourth element of the windkessel model. American Journal of Physiology - Heart and Circulatory Physiology, 1999.

Diploma Thesis Supervisor: Ing. Filip Ježek

Valid until: the end of the summer semester of academic year 2015/2016

L.S.

doc. Dr. Ing. Jan Kybic
Head of Department

prof. Ing. Pavel Ripka, CSc.
Dean

Prague, February 9, 2015

České vysoké učení technické v Praze
Fakulta elektrotechnická

Katedra kybernetiky

ZADÁNÍ DIPLOMOVÉ PRÁCE

Student: Bc. Karel K a l e c k ý

Studijní program: Biomedicínské inženýrství a informatika (magisterský)

Obor: Biomedicínská informatika

Název tématu: Závislost čerpací funkce srdce na tlakových a tokových poměrech v arteriálním stromě

Pokyny pro vypracování:

- Diskutujte nutná zjednodušení reality v modelu vzhledem k požadavku optimalizace.
- Shrňte dostupné modely pulsatilní srdeční mechaniky a srdečního stahu a výkonu.
- Z dostupných modelů sestavte a upravte matematický model pulsatilní srdeční mechaniky
- Sestavte zjednodušený mechanistický model arteriálního stromu, s alespoň první úrovní větvení.
- Propojte modely a zhodnoťte validitu vytvořeného modelu a pokuste se ho uplatnit při studiu vlivu ECMO přístroje ve V-A zapojení.
- Diskutujte další možnosti uplatnění při simulaci patologických stavů (stenózy, zaškrcení či rigidita cév, srdeční selhání etc.)

Seznam odborné literatury:

[1] Pironet, Antoine et al. Simulation of Left Atrial Function Using a Multi-Scale Model of the Cardiovascular System. PLoS ONE, 2003.
[2] Lumens, Joost et al. Three-Wall Segment (TriSeg) Model Describing Mechanics and Hemodynamics of Ventricular Interaction. The Journal of the Biomedical Engineering Society, 2009.
[3] Stergiopulos, Nikos et al: Total arterial inertance as the fourth element of the windkessel model. American Journal of Physiology - Heart and Circulatory Physiology, 1999.

Vedoucí diplomové práce: Ing. Filip Ježek

Platnost zadání: do konce letního semestru 2015/2016

L.S.

doc. Dr. Ing. Jan Kybic
vedoucí katedry

prof. Ing. Pavel Ripka, CSc.
děkan

V Praze dne 9. 2. 2015

DECLARATION

I certify that this thesis is a result of my work and that I have listed all information sources in compliance with Methodical Guidelines of Honoring Ethical Principles for Writing and Composition of Diploma Theses.

In _____ on _____ _____

Karel Kalecký

PROHLÁŠENÍ AUTORA PRÁCE

Prohlašuji, že jsem tuto práci vypracoval samostatně a že jsem uvedl veškeré použité informační zdroje v souladu s Metodickým pokynem o dodržování etických principů při přípravě vysokoškolských závěrečných prací.

V(e) _____ dne _____ _____

Karel Kalecký

ACKNOWLEDGEMENTS

I would like to express my deep appreciation to Mr. Filip Ježek for his patient guidance and provision of stimulating ideas and commentaries.

I also wish to thank my parents for their never-ending support and encouragement.

ABSTRACT

In this thesis, an integrative lumped parameter model of human cardiovascular system – Cardio – is presented. Adopting multiple partial models, it encompasses sarcomere mechanics, ventricular interaction, valve dynamics, systemic and pulmonary circuits, and coronary circulation. Systemic arteries have been implemented in several versions, ranging from simple windkessel models up to an arterial tree with 128 segments. This complex tree has been derived based on physiological dimensions and structure listed in literature. Chronic adaptation of heart and vessel geometry can be simulated. Further, implantation of IABP and connecting to ECMO circuit is supported. For this purpose, a simplified version of the ECMO device has been designed.

Several simulations have been performed for both physiological and pathological scenarios. The results seem to be plausible, capturing well-known phenomena including the Frank-Starling law. This indicates further applicability of the model in research, although first, quantitative validation by a medical expert is desired.

Effects of cardiac supports have been studied with respect to their settings. For IABP, the best results are obtained with inflation set to the dicrotic notch and deflation set right before the onset of systole. For ECMO, connection into ascending aorta in a pulsatile mode is superior, supposing proper timing.

The model has been developed in the Modelica language and provides compatibility with the Physiolibrary framework.

Keywords: Cardiovascular system modeling, heart mechanics, arterial tree, extra-corporeal membrane oxygenator pulsatility, intra-aortic balloon pump timing, Modelica

ABSTRAKT

V rámci této práce byl sestaven lumped parameter model kardiovaskulární soustavy – Cardio. Integruje v sobě některé dosavadní modely a zahrnuje mechaniku sarkomer, interakci srdečních komor, dynamiku chlopní i systemický, pulmonární a koronární oběh. Systemické artérie byly implementovány v několika verzích – od jednouchého windkessel modelu až po komplexní strom se 128 arteriálními úseky. Tento strom je v práci odvozen podle fyziologických rozměrů a struktury uvedených v literatuře. V modelu je možné simulovat chronickou adaptaci geometrie srdce a cév. Dále je podporována implantace IABP a napojení na zařízení ECMO, které bylo k tomuto účelu ve zjednodušené verzi namodelováno.

Byly provedeny simulace fyziologického stavu i několika patologií. Výsledky vypadají věrohodně a zřetelně demonstrují některé známé jevy včetně Frank-Starlingova zákona. Vše nasvědčuje vhodnosti dalšího využití modelu ve výzkumu, nejprve by však měly být výsledky kvantitativně zhodnoceny lékařským expertem.

Dále byly zkoumány vlivy nastavení srdečních podpor. IABP je nejvíce efektivní při synchronizaci inflační fáze s dicrotickým zářezem a deflace těsně před nástupem systoly. ECMO se ukázalo vhodnější při zapojení do vzestupné aorty v pulzatilním módu.

Pro vývoj byl použit jazyk Modelica za vytvoření kompatibility s knihovnou Physiolibrary.

Klíčová slova: Modelování kardiovaskulárního systému, srdeční mechanika, arteriální strom, pulzatilita mimotělního oběhu, časování intraaortální balónkové kontrapulzace, Modelica

TABLE OF CONTENTS

LIST OF CHARTS

LIST OF FIGURES AND TABLES

LIST OF ABBREVIATIONS

#D	#-dimensional
AA	ascending aorta
ECMO	extra-corporeal membrane oxygenator
EDV	end-diastolic volume
IABP	intra-aortic balloon pump
LA	left atrium
LV	left ventricle
LW	left ventricular wall
PDE	partial differential equations
SW	sepal wall
RA	right atrium
RV	right ventricle
RW	right ventricular wall
TA	thoracic aorta

INTRODUCTION

Life is impressive. Every living creature is composed of a few fundamental building blocks, identical across the species. Every human being stems from a single cell. And yet, everybody is so different that sometimes one is urged to deny any conceivable relationship to the other one. Despite its initial simplicity, our physical form develops into the most complex system in the Universe[1] – as far as we know.

A body is a dynamic set of continuously interacting elements (with each other as well as the environment), forming basic functional units (organs) and higher subsystems (organ systems). They follow the common objective of maintaining natural homeostasis[2] via comprehensive auto-regulation mechanisms. Malfunction of a part may be compensated for but may also result in a serious disruption in the regulatory processes and endanger the vital functions.

The cardiovascular system represents such a critical part. In Europe, a cardiovascular disease is a cause of death in 30 % of people deceased under the age of 65 and 46 % in total (Nichols et al., 2014). Therefore, research in this field has the potential of affecting lives of millions of people worldwide.

Factors contributing to cardiovascular diseases are relatively well comprehended (World Health Organization, 2015). Proper treatment is, however, still an open issue – in the United States, 29 % of all heart attacks are of patients who have already experienced a heart attack before (Centers for Disease Control and Prevention, 2015). Acute conditions followed by a cardiogenic shock, requiring connection to an extra-corporeal membrane oxygenator (ECMO) device, are notorious with high mortality – e.g. Ko et al. (2002) have reported 39% mortality during receiving the ECMO support. Combes et al. (2012) have analyzed several studies and detected mortality rates between 25 and 50 %.

Having patients connected to ECMO, there is no much space for experimenting. Medical experts are presented with a set of measurements and are required to make straight decisions. The measurements, and especially their time progress, are a basis for inferring the real condition in the patient's body (solving the inverse problem) and predicting its future development.

In this situation, modeling can be particularly advantageous. Computational models provide the opportunity to study behavior in the section of interest including valid laws and mutual dependencies. Various scenarios can be simulated and their results evaluated, selecting the optimal approach for further treatment. The experiments can be performed relatively fast, and obviously, not affecting the patient's condition nor requiring any animal sacrifice.

However, every model has its range of validity due to assumed simplifications. This is an intrinsic characteristic of models – without any simplification, it would no longer be a model but the modeled object itself, losing all the initial benefits. The amount of simplifications needs to be balanced with the applicability and plausibility of the model to be able to answer the researched questions correctly. In

[1] This, of course, depends on the point of view. Strictly, the Universe itself is more complex than any of its constituents is.

[2] Although this is not necessarily the only purpose, and possibly, not even the primary one.

recent years, increase in computing capacities and advances in availability of modeling tools have occurred, promoting the feasibility of building meaningful models.

The main objective of this thesis is to construct an integrative model of human cardiovascular system including heart mechanics, and subsequently, study arterial pressure-flow patterns and ventricular behavior in several pathological situations and an effect of application of the ECMO support with respect to its settings.

In Chapter 1, the assignment is discussed more thoroughly and a selected approach is formulated. Chapter 2 comprehensively describes the entire model part by part including a literature review for the main components. Performed simulations and their graphical outcomes together with a commentary regarding their physiological feasibility are presented in Chapter 3. Final summary, limitations of the model and its possible enhancements are stated in Conclusion.

1) BASIC CONCEPT

Nature is multifarious. And so is the human body. And so is its modeling. There are various views on how to represent a particular organ, often with a different level of abstraction, primary assumptions, and simplifications. There are diverse modeling methods and software tools, providing miscellaneous possibilities for model development, and simultaneously, imposing fundamental constraints on the problem formulation. Finally, there are also several architectonic styles that can be applied to the model design, each suitable best for a certain task, leading to a different degree of flexibility, reusability and extendibility.

To make a reasonable selection among the multitude of alternatives, the task itself has to be specified in more detail.

1.1) Model Requirements

Generally, any requirements can be classified as either qualitative or quantitative – i.e. aimed at presence of an entity of interest or at numerical quantification and description of an object or a variable.

1.1.1) Qualitative Analysis

For the domain of biomedical engineering, Meurs (2011) suggests a method of specifying qualitative requirements in the following 9 categories:

- ***Physiological system***

  The main interest is in the cardiac circulation system with an emphasis on left ventricle mechanics and systemic arterial tree hemodynamics.

  To compose a closed-loop model, other organs should also be included – remaining parts of the heart, rest of the systemic circuit, and pulmonary circuit.

- ***Population***

  The model should be abstract enough to capture general hemodynamic phenomena and represent an average adult human.

- ***Physiological states***

  By default, the model should mimic the resting condition in the natural environment.

- ***Pathologies***

  Several common pathologies should be able to be simulated, e.g. cardiac ischemia and arterial stenosis.

- ***Clinical signs and monitored variables***

  Standard hemodynamic variables should be monitored within the circuit – these include pressure and flow waveforms, especially. In the left ventricle, the length of sarcomeres and myofiber stress should be computed.

  Furthermore, an index related to the heart's work and power should be calculated.

- ***Critical incidents***

  No scenarios with time-dependent incidents are required.

- ***Interventions***

  The model should provide a possibility for connection of the cardiovascular circuit to an ECMO device. Other types of a cardiac support may be implemented.

- ***Overall block diagram***

  With respect to the above-mentioned requirements, the basic structure of the model should be (at the minimal level of description, at least) as depicted in Figure 1.

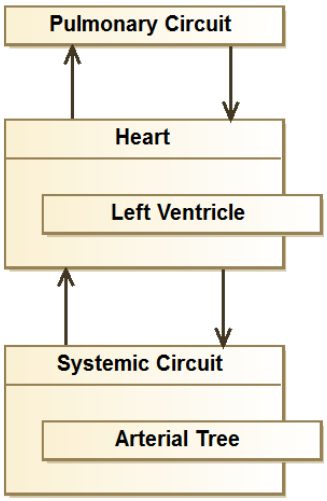

Figure 1: Minimal Required Scheme of the Model

- ***Internal structures and functions***

  Most importantly, the model should describe the beat-to-beat dynamics rather than a static steady-state solution.

  Pressure and blood flow waveforms should be monitored at different places in the arterial tree; thus, the arterial tree has to be composed of individual arteries. The resulting waveforms should also plausibly portray basic hemodynamics phenomena such as a dicrotic notch within the pressure waveform.

1.1.2) Quantitative Analysis

Although average normal values of physiological variables have been well determined and documented in literature, together with either their typical range or variance across the population, similar precise numbers will not be specified here explicitly.

Instead, I refer back to the formulation of representing an average adult human in the resting condition, which should implicitly cover all values for desired variables.

1.2) Selected Approach

Based on the task specification, the final concept has been selected.

1.2.1) Model Paradigm

Lumped parameter modeling has been found the most suitable approach. In lumped parameter models, characteristics and functions of individual parts of the system are confined to single boxes constituting the minimal resolution modeled, which is sufficient for the task assigned. This also allows for abstraction from spatial variations within tissues, leaving time to be the only dimension for differential calculus.

In contrast, 4D models[3] are concerned with exact topology and geometrical properties of tissues, leading to a very accurate spatial description of the system. These models, however, involve much more initial conditions and parameters, and therefore, they are less generalizing. Besides, since they consist of sets of partial differential equations (PDEs), they are computationally demanding.

Similarly, 2D and 3D models can be defined – e.g. in case of modeling development in both time and "forward" dimension in the arterial tree (2D) and considering also angles between arteries at bifurcations (3D). These can be especially useful as an interface between 4D and lumped parameter components, as they are commonly coupled together in one model (Vosse & Stergiopulos, 2011) to reach a precise resolution in one segment of the system while maintaining adequate simplicity in other parts.

Favoring the lumped parameter approach frequently implies a need for a substantial number of simplifications and assumptions. Some of them can be of virtually no impact whereas others can be noticeably reflected in simulated results. Even then, the deviations may still be systematic with a prospect of being reconstructed to a feasible form (using a scaling transformation etc.) – or the dissonance may be totally irreparable.

In such cases, any unexpected results – in discrepancy with qualitative or quantitative requirements – should be well explained and justified with respect to possible propagation of an error across the whole model. Otherwise, all results could be discredited.

[3] Note that in literature, this class of models is typically denoted as 3D. Since there is no practical reason to omit the time dimension (but on the contrary, it is perhaps the most important one in dynamic systems), I prefer to include it in the #D labeling. Likewise, the lumped parameter models are often referred to as 0D, but in reality, there are 1D. Note that sometimes, the dimension depends on one's perspective and resolution – a sequence of 1D models can be regarded as an additional, emergent dimension or not.

As mentioned earlier, a significant simplification is intrinsic to lumped parameter models: all spatially local properties of tissues are regarded as homogenous. Nevertheless, this assumption is expected to be of little importance as far as the required resolution of details is considered.

Other simplifications are more subordinated to particular realizations of the model components. It can be expected that these will completely omit advanced concepts of the "big physics" – both relativistic and quantum phenomena. While relativistic mechanics is of no additional benefit comparing to classical mechanics in the description of human body, quantum mechanics may be crucial in explaining brain processes and consciousness (Sahu et al., 2014, Ghosh et al. 2014), no evidence of any substantial effect on the cardiovascular circulation has been found though (and will likely not be – due to its nature).

Individual parts of the model will be based on research by other authors, as it is reasonable to expect that existing models are well-validated, and thus, providing sufficiently firm ground for fulfilling the quantitative criteria. However, there is a danger hidden in this approach. It can lead to generating additional inaccuracies due to possible inconsistencies between parameters and assumptions of each adopted submodel.

1.2.2) Implementation

For a formal definition of the model, the Modelica language has been selected. Its main advantage is the concept of acausal modeling: a system is modeled as a set of equation that are required to be valid all simultaneously rather than evaluating them sequentially one at a time (as in the MATLAB environment). In other words, Modelica is a domain-neutral declarative language, in which equations represents real equality and can contain complex expressions on both sides of an equation, not an imperative language with sequences of plain assignments to variables.

This is much closer to the actual thinking about physical systems without a need for additional conversion into a sequence of consistent programing commands, which is also likely to considerably save time during the model development.

The only significant constraint of Modelica is its inability to encompass PDEs as user friendly as for ordinary differential equations[4]. Considering lumped parameter models, however, this constraint is no barrier.

Modelica is also an object-oriented language. It allows for both inheritance and object composition, which is very valuable in terms of code reusability and maintenance. Objects can encapsulate their logic and expose desired variables only (e.g. leaving auxiliary variables hidden). Interconnection of individual objects is realized through a connector, which is a special type of an object that carries necessary information for implicit construction of interconnecting equations.

Other features of Modelica include a support for checking unit compatibility in equations, some constructs typical for imperative languages (loops, conditional expressions, arrays etc.), and a method of mapping code to the graphic user interface.

[4] Somewhat "manual" implementation of PDEs is still possible via arrays.

The model is to be constructed within the Dymola editor, commercially developed by Dassault Systèmes. Dymola offers full Modelica support and a basic graphic editor coupled to models. There are several numerical solvers, some of them specially crafted for stiff conditions. Results can be plotted according to desired settings and exported as an image or raw data.

Today, advanced numerical methods provide reasonable precision comparing to an analytical solution (which is practically impossible to derive for complex systems, obviously). Nevertheless, one has to be aware of possible inaccuracies stemmed from the numerical approximation of derivations. The deviation can even be high enough to shift simulation solution from stable to an unstable one.

The model will be compatible with Physiolibrary, created and maintained by Marek Matěják at Institute of Pathological Physiology, Charles University in Prague (2015). This framework is an extension to the standard Modelica library specifically aimed at the domain of physiology – beside others, it contains a basic infrastructure and components suitable to be incorporated into new models (connectors, sensors, sources etc.), a set of thematic icons, semantic variable types, and improves unit conversion by accepting commonly used non-SI units.

2) MODEL DESCRIPTION

Following the task assignment, a cardiovascular model has been composed, including several enhancements. In this section, its structure is described along with a brief literature review for the main parts of interest, additional simplifications and assumptions made in each component, and justification for their adoption.

Initially, a model core has been created. It consists of mechanical model of ventricles, atria based on the identical myofiber concept, and a basic circuit distinguishing between arteries, veins, and peripheral resistance in systemic as well as pulmonary circuit. Moreover, there are heart valves and a coronary circuit incorporated.

Second, several alternatives for a more detailed characterization of systemic arteries have been implemented. These range from a simple 4-compartment windkessel model to a complex physiological arterial tree.

Finally, two heart supports have been formed. These are an ECMO device, allowing for simulation of both pulsatile and non-pulsatile blood flow, and an intra-aortic balloon pump (IABP) with adjustable timing of inflation and deflation.

2.1) Model Core

2.1.1) Heart Mechanics

In recent years, many high-dimensional models of a human heart have been suggested and composed in relation to the advances in computing technologies – e.g. Talbot et al. (2013), Chapelle et al. (2009), and Nordsletten et al. (2011). Despite impressive visualization, which they can output, this class of models has been forbidden earlier as not feasible for the purpose of this project and will no longer be considered.

Literature Review

Caruel et al. (2013) have demonstrated a dimensional reduction of a 4D ventricle model and have reached reduced formulations in 2D and 1D. The latter version, however, assumes spherical symmetry – which is rather a strong simplification – and is meant more like a simulation tool without a physiological accuracy.

Pironet et al. (2013) have proceeded from various previously published models and have created a multi-scale model of heart chamber mechanics. There are three levels of resolution clearly differentiated and interconnected – intracellular calcium concentration, sarcomere mechanics, and chamber geometry.

Chambers are assumed to be hemispheric and their deformation in the radial direction is assumed to be equal to the deformation of a sarcomere. Both active and passive force are generated by sarcomeres, the passive force is, however, approximated only linearly with respect to the length of a sarcomere. In addition, a series elastic element, which is usually embedded within the sarcomere

model to comply with the sliding filament theory – see e.g. Huxley (2004) – has been omitted for simplicity.

Although both left ventricle and atrium follows this concept, the paper primarily targets the left atrium only and only its results are validated.

A similar modular approach has been chosen by Bhattacharya-Ghosh et al. (2012). They consider an organ level with the left ventricular hemodynamics, a protein level with the sarcomere mechanics, and a cellular level with the intracellular calcium dynamics.

Detail of the cellular and protein levels is high, as they include ion channel function, action potential, and cross-bridges kinetics with attachment and detachment of myosin heads. Cardiac muscle energy is assumed to depend on the length of a sarcomere and a proportion of attached cross-bridges. Unfortunately, the left ventricle hemodynamics is said to be simplified and is not fully explained. Also, model parameters adopted from literature have been adjusted in order to help results fit the physiological values and the authors admit that the model requires further validation.

Deserranno et al. (2007) have built a mechanical model of ventricles with an action-myosin cross-bridging and calcium binding model. No assumptions regarding the model and real physiology are discussed although it is obvious from the equations that – at least with respect to ventricular hemodynamics and geometry – substantial simplifications have been made. It is concluded that the model performs more realistic comparing to classical lumped parameter models without the cross-bridging mechanism.

Shim et al. (2008) and Kim et al. (2013) have composed an integrative model of hemodynamics and sarcomere mechanics with cross-bridge dynamics, both controlled by a model of the autonomic nervous system. Although incorporation of baroreflexes providing feedback to the vascular tone, contractility and heart rate is impressive, the geometry of the heart chambers is again simplified as spherical, which is “the main drawback of their study” as the authors say themselves (but try to marginalize its significance in the latter paper).

Lumens et al. (2009) have constructed a model of the ventricular hemodynamics and sarcomere mechanics, in which the left and right ventricles emerge from an immediate position of three spherical heart walls (left free wall, right free wall, and septal wall).

The sarcomere mechanism is based on experiments with rat cardiac muscles and is represented by a passive element coupled in parallel with a series of a contractile element and an elastic element. In addition, wall tension is calculated in both radial and axial directions.

Adoption

Based on the presented literature review, the model of Lumens et al. (2009) – TriSeg – has been found most suitable for the purpose of this project. Although the heart walls are spherical, the septal wall simulates the mutual interaction between the left and right ventricle, which is a phenomenon not comprehended by other models. As a result, the ventricle geometry can appear much more realistic.

Furthermore, there is a long history of research in this field of biomedical modeling by Theo Arts and his collaborators – see e.g. Arts et al. (1971), Arts et al. (1991), Arts et al. (2004), and Lumens et al.

(2008). The model seems to be well validated and together with the model of human cardiovascular circuit CircAdapt (Arts et al., 2004), into which TriSeg has been developed as a module, is currently applied by other authors as a core model platform for their research – e.g. Tobon-Gomez et al. (2012).

Ventricular Geometry

The exact geometrical concept of ventricles and related characteristics are depicted in Figure 2.

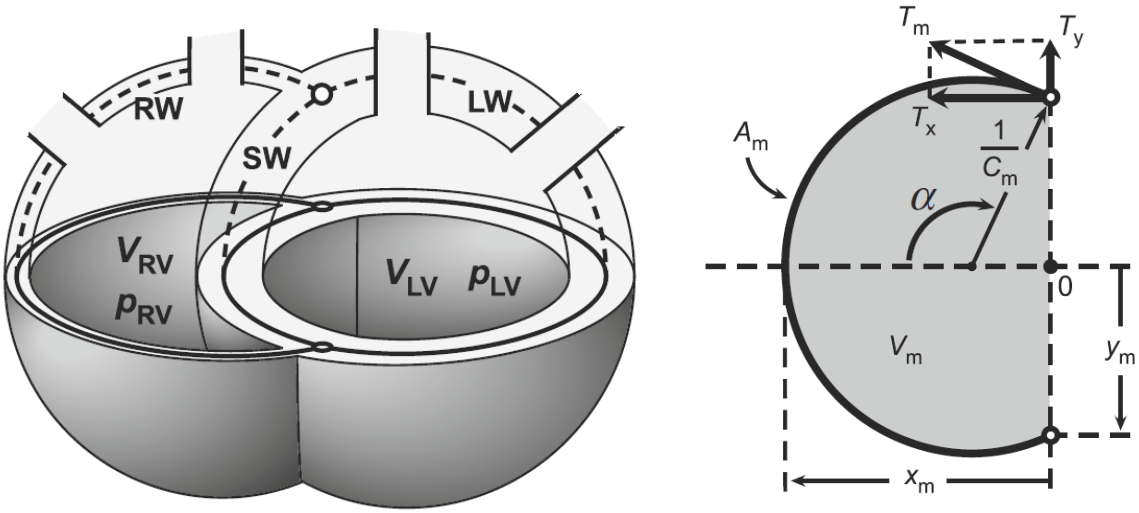

Figure 2: Ventricular Geometry in TriSeg model

Source: Lumens et al. (2009); Legend: RW/SW/LW – right/sepal/left wall, RV/LV – right/left ventricle, V – volume, p – pressure, T – wall tension, C – curvature, A – area, α – angle of spherical surface, x/y – extension along the axis, m in subscript denotes a variable computed with respect to the middle of a heart wall

The following equations, which have been used in the model, are based on those in Lumens et al. (2009) but are modified according to source codes of the latest version of CircAdapt, which can be downloaded for free (Maastricht University – Department of Biomedical Engineering, 2013).

For the simplified ventricular wall geometry, these relations between mid-wall volume V_m, area A_m, curvature C_m, and extension x_m, y_m hold:

$$V_m = \frac{\pi}{6} x_m (x_m^2 + 3y_m^2)$$

$$A_m = \pi (x_m^2 + y_m^2)$$

$$C_m = \frac{2x_m}{x_m^2 + y_m^2}$$

Transmural pressure p_t is related to curvature and mid-wall tension T_m, which can be decomposed into tension in axial T_x and radial T_y direction:

$$p_t = \frac{T_x}{y_m} = 2T_m C_m$$

$$T_x = T_m \sin(\alpha) = T_m \frac{2x_m y_m}{x_m^2 + y_m^2}$$

$$T_y = T_m \cos(\alpha) = T_m \frac{y_m^2 - x_m^2}{x_m^2 + y_m^2}$$

Mid-wall tension is approximated by the relation to wall volume, mid-wall area and myofiber stress σ_f (with z being an auxiliary variable and $A_{m,0}$ dead space mid-wall area):

$$T_m = \frac{V_w \sigma_f}{2A_m}(1 + 0.27z^2)$$

$$z = \frac{1.5 C_m V_w}{A_m - A_{m0}}$$

Sarcomere Mechanics

Length of a sarcomere is determined by a reference length at zero strain $L_{s,ref}$ and natural myofiber strain ϵ_f, which depends mainly on effective mid-wall area and reference mid-wall area $A_{m,ref}$:

$$L_s = L_{s,ref} e^{\epsilon_f}$$

$$\epsilon_f = 0.5 \log\left(\max\left(10^{-9}, \frac{A_m - A_{m,0}}{A_{m,ref}}\right)\right) - \frac{1}{12}z^2 - 0.019z^4$$

The sarcomere length is also divided into a length of an elastic part L_{se} and a contractile part L_{sc}, which are further normalized with a reference length of an isometrically stressed elastic element $L_{se,iso}$ and a reference length of the contractile element with zero active stress $L_{sc,0}$:

$$L_s = L_{se} + L_{sc}$$

$$L_{se,norm} = \max\left(-0.02, \frac{L_{se}}{L_{se,iso}}\right)$$

$$L_{sc,norm} = \max\left(10^{-4}, \left(L_{sc} - L_{sc,0}\right)10^6\right)$$

Myofiber stress stems from a combination of a passive and an active component. Passive stress $\sigma_{f,pas}$ is linked to reference passive stress $\sigma_{f,pas,ref}$, sarcomere length, sarcomere length with zero passive stress $L_{s,pas,0}$ and a stress coefficient $dL_{s,pas}$. Active stress results from reference active stress $\sigma_{f,act,ref}$, normalized lengths of contractile and elastic sarcomere elements, calcium concentration factor C and reference diastolic calcium concentration factor C_R:

$$\sigma_f = \sigma_{f,act} + \max(0.2\sigma_{f,pas}, \sigma_{f,pas})$$

$$\sigma_{f,pas} = \begin{cases} \sigma_{f,pas,ref}\left(0.12\left(\cosh\left(5\frac{L_{s,pas,0}}{dL_{s,pas}}\ln\left(\frac{L_s}{L_{s,pas,0}}\right)\right)-1\right)+\left(\ln\left(\frac{L_s}{L_{s,ref}}\right)+0.1\right)\right); & if\ L_s > L_{s,pas0} \\ \sigma_{f,pas,ref}\left(\ln\left(\frac{L_s}{L_{s,ref}}\right)+0.1\right); & if\ L_s \leq L_{s,pas0} \end{cases}$$

$$\sigma_{f,act} = \sigma_{f,act,ref} L_{sc,norm}((C + C_R)L_{se,norm} - C_R)$$

Contraction of the contractile sarcomere element is driven by reference velocity v_{max}, normalized length of elastic component as well as calcium factor and passive myofiber stress:

$$\frac{\mathrm{d}L_{sc}}{\mathrm{d}t} = \max\left(L_{se,norm} - 1, \left(L_{se,norm} - 1\right)\tanh(10C + \max(0, 10^{-4}{\sigma_{f,pas}}^2))\right) v_{max}$$

Calcium concentration factor follows time t (with 0 being the beginning of contraction), normalized length of the contractile element, and time parameters for rise and decay phases (with a_R and a_D being auxiliary variables), which are derived from time scaling parameter τ_s and activation duration τ_a:

$$\frac{\mathrm{d}C}{\mathrm{d}t} = \frac{\tanh\left(4{L_{sc,norm}}^2\right)0.02a_R^3(8 - a_R)^2 e^{-a_R}}{\tau_R} - \frac{C(0.5 + 0.5\sin(\mathrm{sign}(a_D)\min(0.5\pi, \mathrm{abs}(a_D))))}{\tau_D}$$

$$a_R = \min\left(8, \max\left(0, \frac{t}{\tau_R}\right)\right)$$

$$a_D = \frac{t - \tau_s(0.65 + 0.7L_{sc,norm})}{\tau_D}$$

$$\tau_R = 0.55\tau_s\tau_a$$

$$\tau_D = 0.33\tau_s\tau_a$$

Emergence of Ventricles

Interconnection of all three walls is realized by enforcing the identical position of intersection junction and equality of axial and radial tension, assuming the sepal wall being convex with respect to the left ventricle:

$$y_{m,LW} = y_{m,SW} = y_{m,RW}$$

$$T_{x,LW} = T_{x,SW} + T_{x,RW}$$

$$T_{y,LW} = T_{y,SW} + T_{y,RW}$$

Then, resulting ventricular volume and pressure (pericardial pressure p_P including) can be computed as:

$$V_{LV} = V_{m,LW} - 0.5V_{w,LW} + V_{m,SW} - 0.5V_{w,SW}$$

$$V_{RV} = V_{m,RW} - 0.5V_{w,RW} - V_{m,SW} - 0.5V_{w,SW}$$

$$p_{LV} = p_{t,LW} + p_P$$

$$p_{RV} = p_{t,RW} + p_P$$

Pericardial pressure is derived from reference pericardial pressure $p_{P,ref}$, reference pericardial volume $V_{P,ref}$, current pericardial volume V_P, and stiffness non-linearity parameter k_P:

$$p_P = p_{P,ref}\left(\frac{V_P}{V_{P,ref}}\right)^{k_P}$$

Volume of heart pericardium is a summation of all inner volumes – ventricles, ventricular walls, atria (V_{LA}, V_{RA}), and atrial walls ($V_{w,LA}$, $V_{w,RA}$).

$$V_p = V_{LV} + V_{RV} + V_{w,LW} + V_{w,SW} + V_{w,RW} + V_{LA} + V_{RA} + V_{w,LA} + V_{w,RA}$$

Atria

Heart atria follow the identical concept of sarcomere mechanics, only their geometry is simplified as an ideal sphere:

$$C_m = \sqrt[3]{\frac{4\pi}{3V_m}}$$

$$A_m = \frac{4\pi}{C_m^2}$$

Since there is no interaction between multiple walls in atria, the inner cavity volume is simply a mid-wall volume without the respective wall volume and pressure is a sum of transmural and pericardial pressure; in case of left atrium, however, pericardial pressure is only half (as it is only half around it):

$$V_{LA} = V_{m,LA} - 0.5V_{w,LA}$$

$$V_{RA} = V_{m,RA} - 0.5V_{w,RA}$$

$$p_{LA} = p_{t,LA} + 0.5p_P$$

$$p_{RA} = p_{t,RA} + p_P$$

Parametrization

The model also incorporates parameters for a delay in chamber activation with regard to the cardiac cycle (t_c), simulating physiological (or pathological) delays in transmission of neural signals along the heart tissue.

Values of predefined fixed parameters are provided in Table 1.

Limitations

Authors of the TriSeg module argue that it is a very reasonable model, results of which can – assuming energy conservation and fiber stress homogeneity in a wall – well correspond to conditions in real heart geometries. Cavity dimensions may be underestimated as a result of neglecting non-contractile

basal sheet around ventricles. Numerical approximation of mid-wall tension is deviated less than 2% comparing to an analytical solution (Lumens et al., 2009).

Parameter	Value	Unit
C_R	0.02	–
$dL_{s,pas}$	0.6 (ventricle), 0.8 (atrium)	µm
$L_{s,pas,0}$	1.8	µm
$L_{s,ref}$	2.0	µm
$L_{sc,0}$	1.51	µm
$L_{se,iso}$	0.04	µm
$\sigma_{f,act,ref}$	120 (ventricle), 84 (atrium)	kPa
τ_s	0.25 (ventricle), 0.5 (atrium)	s
v_{max}	7 (ventricle), 10.5 (atrium)	µm / s

Table 1: Fixed Parameters Used in the Heart Model

2.1.2) Vessels

Closed-loop systemic and pulmonary circuits have been also modeled according to CircAdapt (Maastricht University – Department of Biomedical Engineering, 2013). The reason for this selection is not only a guarantee of compatibility with the heart model (because any model parts should be mutually compatible via hemodynamic interaction as long as they are physiologically relevant) but its favorable characteristics: Stiffness of vessels reflects its non-linear nature, and furthermore, the whole circuit contains adaptation rules, which can simulate organ adaptation to chronic conditions (see Section 2.2).

Simultaneously, the circuit remains lumped and is of a reasonably low complexity (arterial tree is to be embedded further). Both systemic and pulmonary circuits consist of three parts – a vessel block for arteries, a controlled resistor for capillaries, and another vessel block for veins.

Arteries and Veins

Vessel blocks are represented by a cylindrical cavity, leading to a direct link between volumes and cross-sectional areas (of cavity and wall as well as reference cavity values) with vessel length l:

$$V = Al$$

$$V_{ref} = A_{ref} l$$

$$V_w = A_w l$$

The relation between volume and pressure is similar to the one of pericardium and is based on referential values, wall volume and stiffness non-linearity coefficient:

$$p = p_{ref} \left(\frac{V_w + 3V}{V_w + 3V_{ref}} \right)^{\frac{k}{3}-1}$$

Vessel cavities are connected to the circuit with a controlled resistor (one ending of which is connected to the circuit and the other one is attached to the cavity). Its resistance R is calculated as (with ρ denoting blood density):

$$R = \frac{\sqrt{\rho\left(\frac{k}{3} - 1\right)\max(1, p)}}{A + \frac{A_w}{3}}$$

Resistors combine blood flow q with pressure difference over the resistor Δp by its resistance according to the fundamental equation:

$$\Delta p = qR$$

Capillaries

Pressure gradient in capillary resistors is not taken directly from the location of the component. Instead, the pressure gradient depends on the pressure inside the vessel cavities. This approach is well described in Arts et al. (2012b) and provides a clear physiological interpretation – capillary resistance corresponds to the true peripheral resistance and resistance in the vessel block represents the true wave impedance.

Also, the pulmonary capillary resistor is modeled with a non-linearity using a reference pulmonary pressure drop $\Delta_{p,pulm,ref}$ as follows:

$$\Delta p = \frac{\Delta_{p,pulm,ref}}{\Delta p} qR$$

Parametrization

Values of predefined fixed parameters are provided in Table 2.

Parameter	Value	Unit
$\boldsymbol{\Delta_{p,pulm,ref}}$	1.5	kPa
$\boldsymbol{\rho}$	1060	kg / m^3

Table 2: Fixed Parameters Used in the Vessel Models

2.1.3) Heart Valves

Valves have not been adopted from the CircAdapt system. Rather, a model of Maynard et al. (2012) has been applied. Its main advantage is a realistic simulation of closing and opening times, which is in contrast to valves in CircAdapt represented as an ideal diode. In addition, valve pathologies can be easily simulated.

Pressure drop over a valve incorporates Bernoulli resistance B, which reflects pressure losses due to convective acceleration and diverging flow, and inertance L, which depends on blood density, valve cross-sectional area, and valve length:

$$\Delta p = Bq\,\mathrm{abs}(q) + L\frac{\mathrm{d}q}{\mathrm{d}t}$$

$$B = \frac{\rho}{2A^2}$$

$$L = \frac{\rho l}{A}$$

Throughout the valves, Poiseuille viscous loses are of little importance, and therefore, are not considered (Mynard et al., 2012).

Immediate cross-sectional area depends on continuous state s (with 1 meaning maximally open and 0 maximally closed valve) and maximal and minimal cross-sectional areas A_{max} and A_{min}, which are given by reference cross-sectional area A_{ref} and coefficients for valve stenosis M_{st} (leading to narrowing of maximal cross-section) and regurgitation M_{rg} (leading to broadening of minimal cross-section), (also note the term for numerical stability avoiding division by zero area in the previous equations):

$$A = (A_{max} - A_{min})s + A_{min}$$

$$A_{max} = (1 - M_{st})A_{ref}$$

$$A_{min} = M_{rg}A_{ref} + 10^{-10}$$

Valve state is changing exponentially with the rate given by coefficients K_o (for opening) and K_c (for closing) up to the boundary values whenever the pressure difference over the valve is higher than reference pressure for opening $\Delta_{p,o}$ or lower than reference pressure for closing $\Delta_{p,c}$:

$$\frac{\mathrm{d}s}{\mathrm{d}t} = \begin{cases} (1-s)K_o(\Delta p - \Delta_{p,o}); & if\ \Delta p > \Delta_{p,o} \\ sK_c(\Delta p - \Delta_{p,c}); & if\ \Delta p < \Delta_{p,c} \\ 0; & otherwise \end{cases}$$

This model is applied for all of the four heart valves (mitral, tricuspid, aortic, and pulmonary valve). Moreover, two additional valves are placed in the circuit into venous inlets of atria. Their purpose is to model complementary resistance and inertance so that their closing mechanism is inactivated by setting M_{rg} to 100 % (full regurgitation). This concept is adopted from the CircAdapt model (Arts et al., 2004).

2.1.4) Coronary Circuit

For the coronary circuit, a model by Bovendeerd et al. (2006) has been implemented. Although Theo Arts is a co-author, the model is not directly connected to CircAdapt. It has been selected for its being lumped and following physiological properties of coronary flow wave, e.g. generally higher flow during heart diastole than during systole.

The circuit is based on fundamental elements in the spirit of electrical analogy – it consists of a series of four resistors representing coronary arterial, two myocardial, and venous resistances interlaced with three capacitors corresponding to arterial, myocardial, and venous compliances.

The myocardial capacitor is, however, not grounded as the other ones but its pressure gradient is co-created by intramyocardial pressure p_{im} at a representative position m, which is defined as a surface

around ventricle volume and one third of its wall volume. p_{im} depends on a passive wall stress in the radial axis $\sigma_{pas,r}$ at the same position and a fraction of left ventricular pressure effective in that position:

$$p_{im,m} = \sigma_{pas,r,m} + p_{LV,m}$$

Knowing radial positions at the inner surface of ventricle wall r_i, at the outer surface r_o, and at the representative surface r_m, the contribution of ventricular pressure to the intramyocardial pressure is expressed as:

$$p_{LV,m} = p_{LV}\frac{r_o - r_i}{r_o - r_i}$$

$$r_o = \sqrt[3]{3\left(V_{LV} + V_{w,LV}\right)}$$

$$r_i = \sqrt[3]{3V_{LV}}$$

$$r_m = \sqrt[3]{3\left(V_{LV} + \frac{V_{w,LV}}{3}\right)}$$

Using the TriSeg model, the ventricle wall volume consists of two walls:

$$V_{w,LV} = V_{w,LW} + V_{w,SW}$$

Passive radial wall stress is derived from a radial fiber stretch ratio λ_r at the representative position:

$$\sigma_{pas,r,m} = \begin{cases} 0; \ \ if\ \lambda_{r,m} < 1 \\ 200\left(e^{9(\lambda_{r,m}-1)} - 1\right); \ \ if\ \lambda_{r,m} \geq 1 \end{cases}$$

$$\lambda_{r,m} = \sqrt[3]{\left(\frac{V_{LV} + \frac{V_{w,LW} + V_{w,SW}}{3}}{V_{0,LV} + \frac{V_{w,LW} + V_{w,SW}}{3}}\right)^{-2}}$$

The input of the coronary circuit is connected to the outlet of the aortic valve and outputs into the right atrium.

2.2) Adaptation

As already mentioned, the parts adopted from the CircAdapt model can be adapted to chronic conditions, which is its significant advantage. The adaptation is realized as a set of update rules executed after each cardiac cycle, which are based on real physiological processes within tissues and experimental observations (Arts et al., 2004, Arts et al., 2012a). These include dilatation of vessel diameter according to average shear stress, adaptation of vessel wall thickness to internal pressure, adaptation of chamber walls and others.

The rules involve average values of state variables that are calculated with regard to the last cardiac cycle. Similarly, maximal values of state variables are used (note the difference between max function with two arguments returning the greater one and max function with one argument returning the maximal value of the argument during the last cycle).

The CircAdapt routine can be launched with three different settings of adaptation – minimal adaptation (although the authors refer to is as no adaptation), resting adaptation, and adaptation during exercise.

Minimal Adaptation

With the minimal adaptation, both systemic and pulmonary capillary resistances are adjusted according to reference pressure in systemic arteries $p_{SA,ref}$, reference blood flow q_{ref}, and reference pressure drop over lungs $\Delta_{p_p,ref}$:

$$R_{s,new} = \frac{p_{SA,ref} - \mathrm{avg}(p_{SV})}{q_{ref}}$$

$$R_{p,new} = \frac{\Delta_{p,pulm,ref}}{\mathrm{avg}(q_p)}$$

Resting Phase

Resting adaptation includes the minimal adaptation and further adaptation of reference cross-sectional area and reference pressure in each vessel segment:

$$A_{ref,new} = A_{ref}\left(\frac{0.17\,\mathrm{avg}(A)}{\mathrm{abs}(\mathrm{avg}(q))}\right)^{-0.5}\left(\frac{p_{ref}}{\sqrt{\mathrm{avg}(p^2)}}\right)^{-\frac{0.5}{\frac{k}{3}-1}}$$

$$p_{ref,new} = \left(\frac{p_{ref}}{\sqrt{\mathrm{avg}(p^2)}}\right)^{0.5}\sqrt{\mathrm{avg}(p^2)}$$

In addition, reference cross-sectional areas of valves A_{ref} are adjusted[5] to fit the average cross-sectional area of connected vessels, or are rescaled to 150% of area of the appropriate arterial valve in case of atrioventricular valves respectively.

These modifications are also reflected in changes to dead area $A_{m,0}$ of heart chambers – for free ventricular walls (left and right, not sepal), it is a sum of areas of their atrioventricular valve and arterial valve, and for atria, it is a sum of areas of their atrioventricular valve and venous pseudo-valve.

Exercise Phase

Adaptation in exercise state is more complex and proceeds in several stages. First, the minimal adaptation is performed just as in case of resting adaptation. Then, wall cross-sectional area (and thereby wall volume) is adjusted (with v_i being impact velocity, to which the body is a subject during movements, e.g. running and jumping):

[5] Although the valves used in this project are not from CircAdapt as already explained, this adaptation mechanism can be applied to them as easily.

$$A_{w,new} = A_w \left(\frac{0.5\text{e}6}{\max\left((p + RAv_i)\left(1 + \frac{3A}{A_w}\right)\right)} \right)^{-0.5}$$

A heuristic correctional factor for reference mid-wall area of sepal wall $E_{A_{m,ref},SW}$ is calculated in order to model heart geometry more reliably (for other walls including atrial walls, it is zero):

$$E_{A_{m,ref},SW,new} = 5 \ln\left(\frac{A_{m,ref,LW} A_{m,ref,RW}}{A_{m,ref,SW}\left(A_{m,ref,LW} + A_{m,ref,RW}\right)} \right)$$

Further, wall volume, reference mid-wall area, and reference passive myofiber stress are recomputed for each chamber wall (here, the correctional factor is employed) according to values and relations found by best fit and sensitivity analysis (note that the entire expressions "0.5(…+…+…)" are in the exponent of e); for more details, see Arts et al. (2012a)):

$$V_{w,new} = V_w e^{0.5\left(\frac{0.3957}{2}\tanh\left(0.5\ln\left(\frac{1\text{e}6\left(L_{s,max,ref} - L_{s,min,ref}\right)}{\sqrt[3]{\frac{\text{avg}\left(\max(0,\sigma_{f,act})\left(1\text{e}6 L_{sc} - \frac{\text{avg}(\max(0,\sigma_{f,act}) 1\text{e}6 L_{sc})}{\text{avg}(\max(0,\sigma_{f,act}))}\right)^2\right)}{\text{avg}(\max(0,\sigma_{f,act}))}}} \right)\right) - \frac{0.3066}{2}\tanh\left(0.5\ln\left(\frac{\sigma_{f,pas,ref,adapt} e^{-E_{A_{m,ref}}}}{\max(\max(0,\sigma_{f,pas}))} \right)\right) - \frac{0.235}{2}\tanh\left(0.5\ln\left(1\text{e}6\left(L_{s,min,ref} + 0.6\left(L_{s,max,ref} - L_{s,min,ref}\right)\right)\frac{\text{avg}(\max(0,\sigma_{f,act}) 1\text{e}6 L_{sc})}{\text{avg}(\max(0,\sigma_{f,act}))} \right)\right)\right)}$$

$$A_{m,ref,new} = A_{m,ref} e^{0.5\left(\frac{-0.4571}{2}\tanh\left(0.5\ln\left(\frac{1\text{e}6\left(L_{s,max,ref} - L_{s,min,ref}\right)}{\sqrt[3]{\frac{\text{avg}\left(\max(0,\sigma_{f,act})\left(1\text{e}6 L_{sc} - \frac{\text{avg}(\max(0,\sigma_{f,act}) 1\text{e}6 L_{sc})}{\text{avg}(\max(0,\sigma_{f,act}))}\right)^2\right)}{\text{avg}(\max(0,\sigma_{f,act}))}}} \right)\right) - \frac{0.0433}{2}\tanh\left(0.5\ln\left(\frac{\sigma_{f,pas,ref,adapt} e^{-E_{A_{m,ref}}}}{\max(\max(0,\sigma_{f,pas}))} \right)\right) + \frac{1.3028}{2}\tanh\left(0.5\ln\left(1\text{e}6\left(L_{s,min,ref} + 0.6\left(L_{s,max,ref} - L_{s,min,ref}\right)\right)\frac{\text{avg}(\max(0,\sigma_{f,act}) 1\text{e}6 L_{sc})}{\text{avg}(\max(0,\sigma_{f,act}))} \right)\right)\right)}$$

$$\sigma_{f,pas,ref,new} = \sigma_{f,pas,ref} e^{0.5\left(\frac{-0.3338}{2}\tanh\left(0.5\ln\left(\frac{1\text{e}6\left(L_{s,max,ref} - L_{s,min,ref}\right)}{\sqrt[3]{\frac{\text{avg}\left(\max(0,\sigma_{f,act})\left(1\text{e}6 L_{sc} - \frac{\text{avg}(\max(0,\sigma_{f,act}) 1\text{e}6 L_{sc})}{\text{avg}(\max(0,\sigma_{f,act}))}\right)^2\right)}{\text{avg}(\max(0,\sigma_{f,act}))}}} \right)\right) + \frac{0.2091}{2}\tanh\left(0.5\ln\left(\frac{\sigma_{f,pas,ref,adapt} e^{-E_{A_{m,ref}}}}{\max(\max(0,\sigma_{f,pas}))} \right)\right) - \frac{1.3101}{2}\tanh\left(0.5\ln\left(1\text{e}6\left(L_{s,min,ref} + 0.6\left(L_{s,max,ref} - L_{s,min,ref}\right)\right)\frac{\text{avg}(\max(0,\sigma_{f,act}) 1\text{e}6 L_{sc})}{\text{avg}(\max(0,\sigma_{f,act}))} \right)\right)\right)}$$

Finally, reference volume of pericardium is adjusted:

$$V_{P,ref,new} = \frac{V_{P,ref}}{\left(\frac{p_{P,ref}}{\max(p_P)}\right)^{0.3/k_P}}$$

Parametrization

List of additional predefined fixed parameters is provided in Table 3.

Parameter	Value	Unit
$L_{s,max,ref}$	2.2	µm
$L_{s,min,ref}$	1.75	µm
$p_{SA,ref}$	12.2	kPa
$\sigma_{f,pas,ref,adapt}$	7.5 (ventricle), 52.5 (atrium)	kPa
v_i	3	m / s

Table 3: Fixed Parameters Used for Adaptation

All of these adaptation mechanisms have been implemented and can be set in Settings block within the model. Also, true "no adaptation" option (i.e. without adaptation of capillary resistances) is included for completeness.

Adaptation Protocol

The adaptation, as used by the authors of CircAdapt, is to follow an adaptation protocol of repetitive alternating between adaptation at rest and adaptation during exercise – the adaptation state is switched after convergence (when only minimal adjustments are made to the parameters being adapted) and the switching should continue until the convergence persists after switching (in both directions).

Nevertheless, this protocol is not implemented in CircAdapt and the routine has to be manually re-launched each time if one wants to switch between adaptation states. In the presented model, a more convenient approach has been built-in, which can automatically alternate between adaptation states at run-time and finish in the resting state after reaching persistent convergence.

The convergence criterion is a sum of square differences between values before and after a cardiac cycle for mean aortic flow (in milliliters), mean aortic pressure (in mmHg), and mean pulmonary pressure drop (in mmHg). Although these values are not parameters being adapted, they represent global characteristics of the circuit and are expected to reflect changes in adapted parameters, thereby convergence.

The adaptation states switches whenever the convergence criterion declines below 0.01 (as a result of compromise between adaptation time and reasonable accuracy). After switching, there is an inter-phase of minimal adaptation to balance the sudden jump in hemodynamic conditions (the circuit needs some time to absorb the changes and converge). Understandably, these inter-phases are not counted towards the criterion of persistent convergence.

In CircAdapt, blood volume is constantly regulated with respect to the value of aortic pressure. This leads to fluctuations in blood volume within cardiac cycle. In the presented model, blood volume is

fixed and has been slightly increased at rest comparing to CircAdapt (0.95 vs. 0.87 l; in literature, various values for stressed blood volume are used, e.g. 0.88 l (Kaye et al, 2014), 0.95 l (Morley et al., 2007), and 1.5 l (Pettersen et al., 2014)). Unstressed volume is not incorporated.

Overview of the basic hemodynamic parameters related to a simulated condition is provided in Table 4.

Parameter	Value	Unit
q_{ref}	85 (rest), 255 (exercise)	ml / s
t_c	0.85 (rest), 0.425 (exercise)	s
V	0.95 (rest), 1.3 (exercise)	l

Table 4: Hemodynamic Parameters Dependent on Condition and Adaptation Profile

2.3) Systemic Arteries

After the basic model had been built, construction of a more detailed version of systemic arteries was necessary. Again, various multi-dimensional models exist (a summary of various types is described in Vosse & Stergiopulos (2011)), but only lumped parameter models are considered to be embedded into the presented model.

Generally, all such models are based on decomposition of vessel properties into three fundamental characteristics – hemodynamic resistance R, inertance L, and compliance C. These are related to blood flow and pressure gradient by the following equations (which are identical to those for resistance, inductance, and capacitance in the electrical domain):

$$R = \frac{\Delta p}{q}$$

$$L = \frac{\Delta p}{\frac{\mathrm{d}q}{\mathrm{d}t}}$$

$$C = \frac{q}{\frac{\mathrm{d}\Delta p}{\mathrm{d}t}}$$

Blood, being a suspension of plasma and blood cells, is known to be a non-Newtonian fluid (in which shear rate and shear stress are not linearly dependent) flowing not only in a laminar manner but also with occasional local turbulences. The material of vessel walls is not only elastic but also viscous thereby viscoelastic (with a non-trivial relation between viscosity and elasticity). Inevitably, the characteristics R, L, and C are dynamic in relation to pressure, blood wave velocity etc.

Neglecting some of these facts, e.g. by assuming entirely constant R, L, and C, may result in deformations of blood flow and pressure waveforms (Segers et al., 1997).

The most elemental lumped parameter models for human vessels are windkessel models, which describe the whole part of interest globally. The inner structure of the model varies; Shi et al. (2011) mentions i.a. the following examples (here, "-" denotes serial connection, "/" represents parallel connection, and "\" returns back from a parallel branch; the compliance element is always grounded):

$$\rightarrow R -/C\backslash\rightarrow$$

$$\rightarrow R -/C\backslash -R \rightarrow$$

$$\rightarrow R -/(R - C)\backslash\rightarrow$$

$$\rightarrow R - L -/C\backslash -R \rightarrow$$

$$\rightarrow (R/L) -/C\backslash -R \rightarrow$$

After subdividing the whole vessel system into individual arteries, or veins respectively, the idea of windkessel models can be easily applied to each segment. Such lumped parameter models are called distributed (as referred to by Vosse & Stergiopulos (2011), Shi et al. (2011) label them as multi-compartment).

Usually, the total number of segments is subordinated to the purpose being pursuit. Examples for systemic arteries include Ferrari et al. (2000) with 19 segments, Abdolrazaghi et al. (2010) with 30 segments, Mirzaee et al. (2009) with 36 segments, Naik & Bhathawala (2014) with 91 segments, and Avolio (1980) with 128 segments.

With increasing complexity of the arterial tree, the model can be more accurate and can provide more information about blood pressure and flow in arteries. The longer time, which is required for simulation, can be, however, an unnecessary obstacle whenever detailed information is not needed. To provide higher flexibility and a possibility of comparison, several models of systemic arteries with various complexity have been implemented.

2.3.1) Four-element windkessel model

The last example of windkessel types mentioned above is of a distinguished position due to a close relation of its parameters to real characteristics of the vessel system: L is a summation of all its inertances, C reflects total compliance, the first (parallel) R corresponds to characteristic resistance (R_c), and the second R matches peripheral resistance (R_p) (Stergiopulos et al. 1999).

Although it is not an arterial tree and is likely to bring little improvement comparing to the basic vessel block, it can help validate the selected approach of substituting the block of systemic arteries with independent sub-models, supposing its results are similar to the original ones.

Values of the characteristics are set as given in Stergiopulos et al. (1999) and are listed in Table 5.

Parameter	Value	Unit
$\boldsymbol{C}$	1.37	ml / mmHg
$\boldsymbol{L}$	0.007	mmHg s^2 / ml
$\boldsymbol{R_c}$	0.057	mmHg s / ml
$\boldsymbol{R_p}$	1.05	mmHg s / ml

Table 5: Windkessel Model Parameters Used by Stergiopulos

The Physiolibrary framework (Institute of Pathological Physiology, Charles University in Prague, 2015) also contains this type of windkessel model. For the purpose of comparison, it has been implemented as well. Its parameter values are provided in Table 6.

Parameter	Value	Unit
C	1.4	ml / mmHg
L	0.005	mmHg s^2 / ml
R_c	0.005	mmHg s / ml
R_p	0.926	mmHg s / ml

Table 6: Windkessel Model Parameters Used in Physiolibrary

2.3.2) Simple Aortic Model

Ferrari et al. (2000) have designed a 1-level model of aorta (which has been also constructed physically) with 8 aortic segments in the form of:

$$\rightarrow R - L - /C \backslash \rightarrow$$

Values of resistance, inertance, and compliance are computed with respect to physiological dimensions of each aorta segment (length l, average radius r, average wall thickness h) with the following equations:

$$R = 8\frac{\mu l}{\pi r^4}$$

$$L = \frac{\rho l}{\pi r^2}$$

$$C = 1.5\frac{\pi r^3 l}{Eh}$$

However, values for compliance listed in the paper do not correspond to the equation. Instead, compliance is scaled by the factor of approximately 0.235 without any explanation or even a mention. Using the original equation leads to very unfavorable results. Therefore, the real equation used by the authors is:

$$C = 0.353\frac{\pi r^3 l}{Eh}$$

Material properties of blood (density ρ and viscosity μ) slightly differ across various models (e.g. 1050 vs. 1060 kg/m3), impact of the variations is minimal and the circulation model presented in this thesis consistently uses values which are given in Table 7.

Constant	Value	Unit
μ	4	mPa s
ρ	1060	kg / m^3

Table 7: Blood Physical Properties

Elastic property of the vessel wall – Young's modulus E – is in this aorta model specified as:

$$E = 4.08\ gf/mm^2 = 40.011\ kPa$$

This is a suspicious values – 10 times lower comparing to other studies, e.g. Wang and Parker (2004), Avolio (1980), and Naik & Bhathawala (2014). We may argue that this error is connected with the

undocumented change in the previous equation. Assuming the right value of E, the equation used is in reality:

$$C = 3.53\frac{\pi r^3 l}{Eh}$$

To the aorta, 11 branches are connected. These are represented by a resistive load or by one of the following combination with compliance:

$$\rightarrow R -/C\backslash\rightarrow$$

$$\rightarrow R -/(R - C)\backslash\rightarrow$$

Values of their characteristics are given. Their origin, however, remains unclear.

The complete model is illustrated in Figure 3.

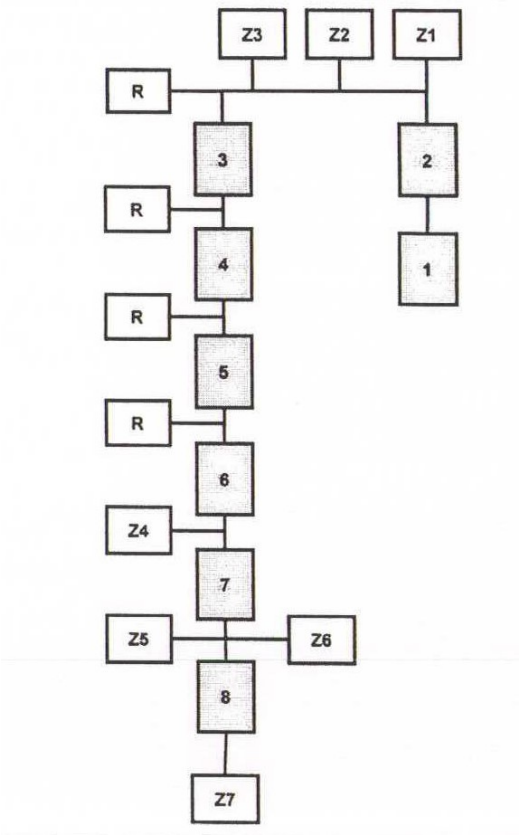

Figure 3: Block Scheme of Simple Aortic Model

Source: Ferrari et al. (2000); Individual segments of aorta denoted: 1 – ascending aorta, 2, 3 – aortic arch, 4, 5, 6 – thoracic aorta, 7, 8 – abdominal aorta; other blocks represent peripheral loads across the body

2.3.3) Simple Arterial Tree

Abdolrazaghi et al. (2010) model the entire cardiovascular circuit with accent to both systemic and pulmonary arteries. From this, only the part with systemic arteries has been implemented. The tree consists of 30 compartments of one of the following types:

$$\rightarrow/C\backslash-L-R\rightarrow$$

$$\rightarrow/C\backslash-R-L\rightarrow$$

$$\rightarrow/C\backslash-(L/R)-R\rightarrow$$

$$\rightarrow/C\backslash-R-(L/R)\rightarrow$$

Values of the characteristics are said to be based on physiological dimensions according to those equations (with the resistance in parallel with inertance being denoted R_c as the characteristic resistance):

$$R = 8\frac{\mu l}{\pi r^4}$$

$$R_c = 8\left(\frac{\lambda_q}{\lambda_q} - 1\right)\frac{\mu l}{\pi r^4}$$

$$L = 8\left(\lambda_q - \lambda_p\right)\frac{\rho l}{\pi r^2}$$

$$C = 1.5\frac{\pi r^3 l}{Eh}$$

Scaling parameters λ_q and λ_p are dependent on a radius of each segment:

$$\lambda_q = \begin{cases} 0.1729; & if\ r < 2\ mm \\ 0.2057; & if\ r \geq 2\ mm \end{cases}$$

$$\lambda_p = \begin{cases} 0.0075; & if\ r < 2\ mm \\ 0.0392; & if\ r \geq 2\ mm \end{cases}$$

The assumed physiological values are not mentioned, only computed resistances, inertances, and compliances are given. However, the physiological values can be traced back by solving for the set of equations above (r, l and h can be discovered knowing R, L and C).

Unfortunately, the revealed physiological values for ascending aorta are non-sense (with length 44 cm and thickness 22 cm). The following equations from the original paper, which are used to compute stiffness (inverse of compliance) in parts of the circuit that are not central to the arterial tree, can shed some light on the issue:

$$S_{LD} = 4.5\ mmHg \times 1332\ /\ 120\ ml = 49.5\ gm/cm^4 s^2$$

$$S_{LS} = 90\ mmHg \times 1332\ /\ 48\ ml = 2497.5\ gm/cm^4 s^2$$

First, pressure in mmHg can be converted to Pa by multiplication with 133.32 (101325/760 by definition), not with 1332 – note the difference in both order and digits. Although the result of the conversion is correct (with gm being an old and deprecated alternative for grams), the style of interfering with extra auxiliary variables into a conversion equation is formally wrong and dangerous. Second, 4.5 × 1332 / 120 is not 49.5 but 49.95. It can be inferred that the authors are not overly thorough and make mistakes and typos in critical parts of the paper.

After a further investigation (a series of experiments), the given values were found to be 10 times higher (in case of R and L) and lower (in case of C) comparing to the right ones. It suggests that the authors have propagated the constant 1332 into other conversion equations and corrupted the results (it agrees – the unit of R and L contains mmHg and their values are 10× higher, whereas the unit of C contains mmHg-1 and its values are 10× lower).

Thereafter, the pressure waveforms correspond to the result in the paper and the "reverse-engineered" physiological values are sensible (ascending aorta with length 4.4 cm, radius 1.58 cm, and wall thickness 0.22 cm, which is relatively close to dimensions used by other authors – Ferrari et al. (2000), Avolio (1980), and Naik & Bhathawala (2014); possibly, a little higher coefficient such as 11.3× instead of 10× would give even better fit but this could result in overfitting and also no interpretation offers, using 13.3× produces worse results than 10×).

The adopted part of the circuit is vizualized in Figure 4.

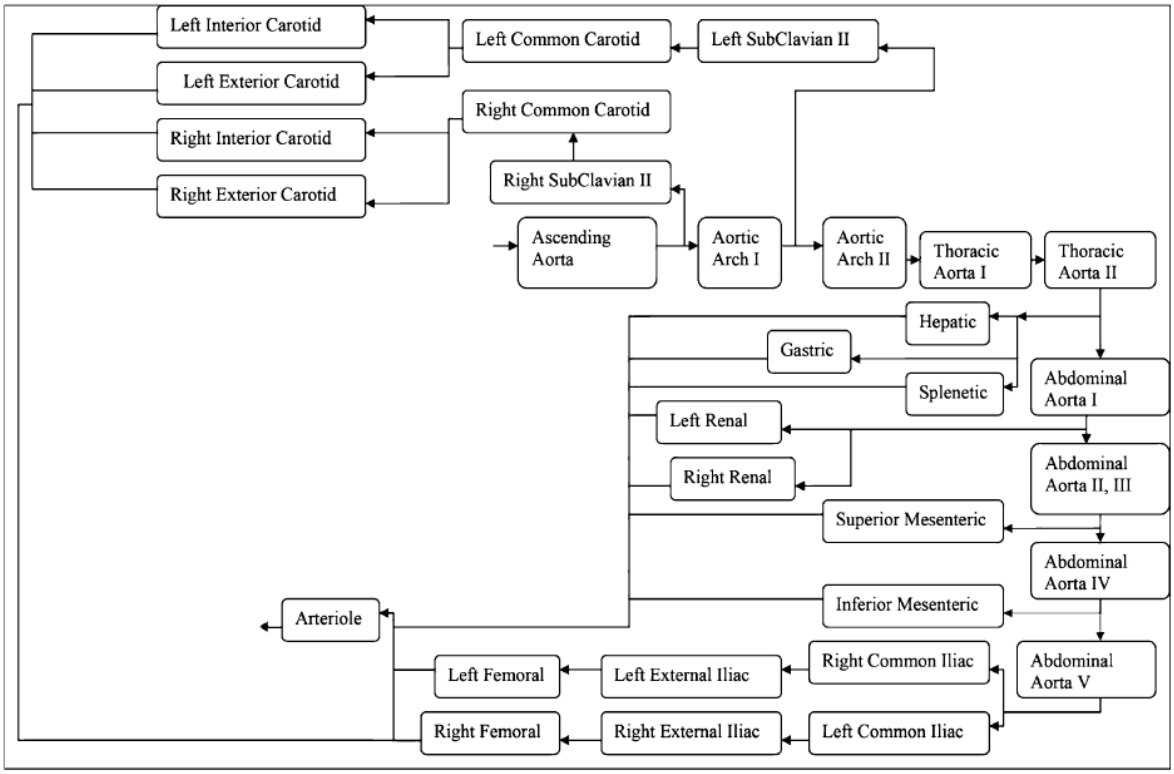

Figure 4: Block Scheme of Simple Arterial Tree

Source: Abdolrazaghi et al. (2010)

2.3.4) Complex Arterial Tree

Since the previous implementation are not entirely credible, a further attempt has been made to provide a physiologically relevant arterial tree. Calculations of Naik & Bhathawala (2014) are also discredited, since their values of inertances do not correspond to their equations (by approximately 11%).

On the other hand, Avolio (1980) has constructed a complex arterial tree (see the structure in Figure 5), which is directly based on physiological dimensions and has been well explained and validated (O'Rourke & Avolio, 1980). It is regarded as one of the most realistic arterial models (Shi et al., 2011). Calculation of its characteristics is, however, complex and involves frequency analysis of incoming flow wave so as to account for viscoelastic effects and dynamic Young's elastic modulus of arteries.

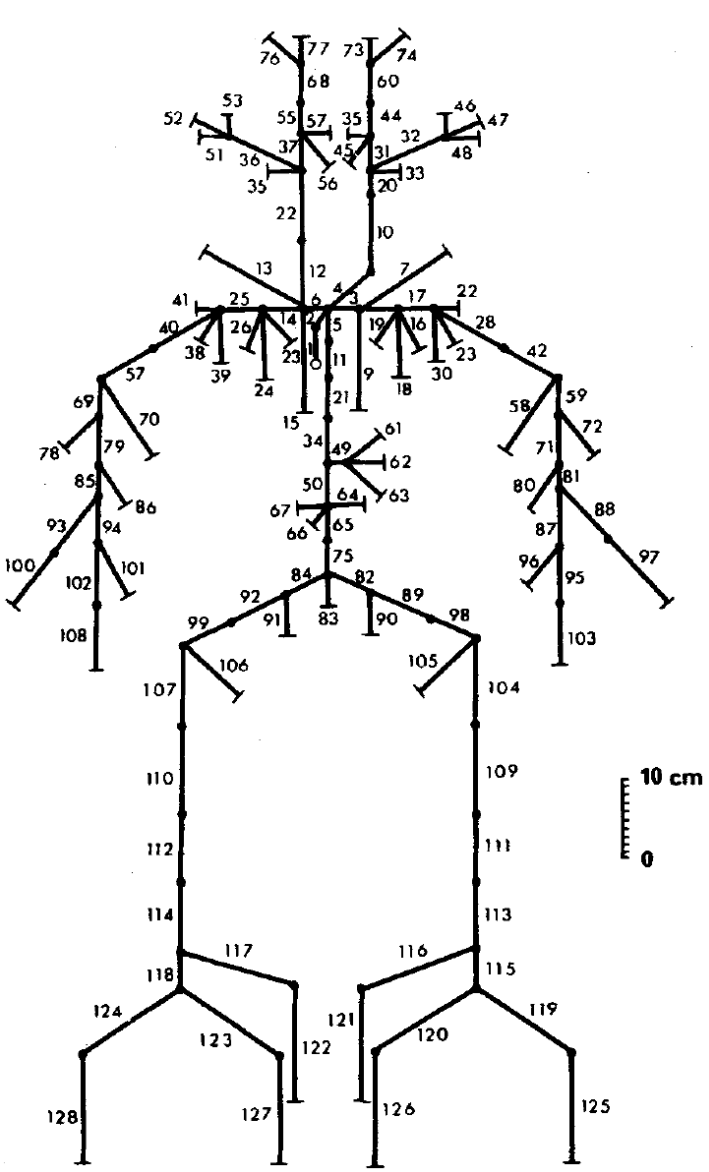

Figure 5: Scheme of Complex Arterial Tree

Source: Avolio (1980); Description of individual segments can be found in Avolio (1980); Note typos in this original illustration – e.g. segments 22 and 35 are doubled whereas 29 and 43 are missing…

Therefore, an own simple implementation of an arterial tree has been derived based on tree structure and physiological dimensions as used by Avolio (1980). (During the process of adoption, several mistakes were revealed in the original paper including typos in values of arterial dimensions and mislabeling arterial segments in the tree figure. All found problems have been resolved.)

Method of Derivation

Each artery is represented by the segment:

$$\rightarrow R - L - /C \backslash \rightarrow$$

Values of resistance, inertance, and compliance are computed according to equations (with R_b being branching resistance and q_C compliance numerical coefficient):

$$R = 8\frac{\mu l}{\pi r^4} + R_b$$

$$L = 8\left(\lambda_q - \lambda_p\right)\frac{\rho l}{\pi r^2}$$

$$C = q_C\frac{\pi r^3 l}{Eh}$$

For total resistance, branching resistance R_b is considered for segments located immediately after a branching junction (or using technical terminology, if they have siblings).

R_b is set to be proportional to the fraction of h/r, which is based on the geometrical view that the area making a barrier to the blood flow is directly proportional to the wall thickness and vessel radius (hr), whereas the open area is proportional to a square of the vessel radius (r^2). This ratio is multiplied with reference value $R_{b,ref}$, which has been heuristically set to 100 Pa×s/ml:

$$R_b = \begin{cases} R_{b,ref}\dfrac{h}{r}; & if\ after\ branching \\ 0; & otherwise \end{cases}$$

Coefficients λ_q and λ_p are used as in the previously described arterial tree for arteries larger than 2 mm (Abdolrazaghi et al., 2010). These values have been originally derived by Olufsen & Nadim (2004) as a second-order approximation of Navier-Stokes flow equations and are said to be applicable for arteries with radius less than 1.5 cm – which is satisfied for all segments. Note that there is no need to employ a different set of coefficients (representing only a first-order approximation) for arteries with radius below 2 mm as Abdolrazaghi et al. (2010) do.

The total numerical coefficient in the inertance equation thus equals 1.332. It describes an assuming profile of the flow wave, for which 1 means a completely flat profile (as used in the first described tree by Ferrari et al. (2010)), which is obviously not the real case. 1.332 corresponds to values used by other authors – it is practically identical to 4/3 used by Stergiopulos et al. (1999) and originally derived by Jager et al. (1965).

Neglecting non-linearities, arterial viscoelasticity, and non-real components of peripheral impedance leads to severe underestimation of arterial compliance, which can have significant effects (even

several tenths of mmHg), especially in distant parts of the tree (Segers et al., 1997). Therefore, using the original form of the compliance equation (i.e. with q_C equal to 1.5) would be unwise.

The modification used by Ferrari et al. (2000) as discovered and explained in the first described aortic model behaves surprisingly well. Perhaps, this match is not a coincidence and their undocumented variant of the equation is of a rational origin.

Summary of the constants used in this tree model along with the origin of their values is listed in Table 8.

Constant	Value	Unit	Origin
$\boldsymbol{\lambda_p}$	0.0392	–	Literature (Olufsen)
$\boldsymbol{\lambda_q}$	0.2057	–	Literature (Olufsen)
$\boldsymbol{q_C}$	3.53	–	Literature (Ferrari)
$\boldsymbol{R_{b,ref}}$	100	Pa s / ml	Heuristic

Table 8: Constants Used in the Derived Arterial Tree Model

2.4) Heart supports

Finally, intra-aortic balloon pump and extra-corporeal membrane oxygenation have been incorporated into the model.

2.4.1) IABP

The balloon pump has been implemented according to Schampaert et al. (2013). It is based on representation of the pump as an additional compliance object, which is connected in parallel to the compliance in each relevant aortic segment and terminated with a pressure control (instead of being grounded). The compliance value is not mentioned in the paper, however, the balloon is expected to be rather stiff. Therefore, it has been scaled 0.1 times comparing to the segment compliance.

Pressure inside the balloon oscillates between $p_{IABP,inf}$ when fully inflated and $p_{IABP,def}$ when deflated. Transition between both phases occurs linearly throughout the interval τ.

$$\frac{\mathrm{d}p_{IABP}}{\mathrm{d}t} = \begin{cases} \dfrac{p_{IABP,inf} - p_{IABP,def}}{\tau}; & when\ inflating \\ \dfrac{p_{IABP,def} - p_{IABP,inf}}{\tau}; & when\ deflating \\ 0; & otherwise \end{cases}$$

Also, the balloon radius r_{IABP} is linearly dependent on the balloon pressure, therefore:

$$\frac{\mathrm{d}r_{IABP}}{\mathrm{d}t} = \begin{cases} \dfrac{r_{IABP,inf} - r_{IABP,def}}{\tau}; & when\ inflating \\ \dfrac{r_{IABP,def} - r_{IABP,inf}}{\tau}; & when\ deflating \\ 0; & otherwise \end{cases}$$

Furthermore, original values of resistance and inertance in concerning segments needs to be modified with respect to the immediate radius of the balloon (with ξ denoting its proportion to the segment radius):

$$R = \frac{R_{original}}{1 - \xi^4 - \frac{(1-\xi^2)^2}{\ln(\xi)}}$$

$$L = \frac{L_{original}}{1 - \xi^2}$$

$$\xi = \frac{r_{IABP}}{r}$$

IABP has been installed into the complex arterial tree derived in the previous section, affecting four aortic segments. Placement and dimensions of the pump (resulting in the length of 20.9 cm and volume 42 ml) have been selected to correspond with real devices as stated by Krishna & Zacharowski (2009). Balloon pressure and duration of phase transition are given by Schampaert et al. (2013). Values of the constants are listed in Table 9.

Constant	Value	Unit
$p_{IABP,def}$	-200	mmHg
$p_{IABP,inf}$	200	mmHg
$r_{IABP,def}$	0.5	mm
$r_{IABP,inf}$	8	mm
τ	80	ms

Table 9: Constants Used in the IABP Model

Time points of inflation and deflation phases can be set with respect to the cardiac cycle.

2.4.2) ECMO

No lumped parameter model for a pulsatile ECMO device has been found in literature. Therefore, an own simplified version has been designed, which should be flexible enough for desired purposes while maintaining its basic characteristics comparable to real data.

The model can be parametrized by setting a reference mean flow $q_{mean,ref}$ and indicator of pulsatility. If using pulsatile ECMO, the duration of a pulse, cycle period, and time delay with respect to the period need to be specified.

Focusing on the inner structure, there are two basic units – a pump and an oxygenator – and three connective tubes (one 20cm long interconnecting the pump and the oxygenator and two 50cm long for connection to a patient, each with a diameter of 1 cm). The tubes are considered resistive only, following the same Poiseuille equation as defined earlier:

$$R = 8\frac{\mu l}{\pi r^4}$$

Both ends of the circuit are connected to resistive segments simulating cannulas (with length 15 cm, outer diameter 7 mm, and inner diameter 5 mm – based on Royal Children's Hospital – Victorian Paediatric Cardiac Surgical Unit (2004)) and ideal valves to prevent backward blood flow. The complete structure is schemed in Figure 6.

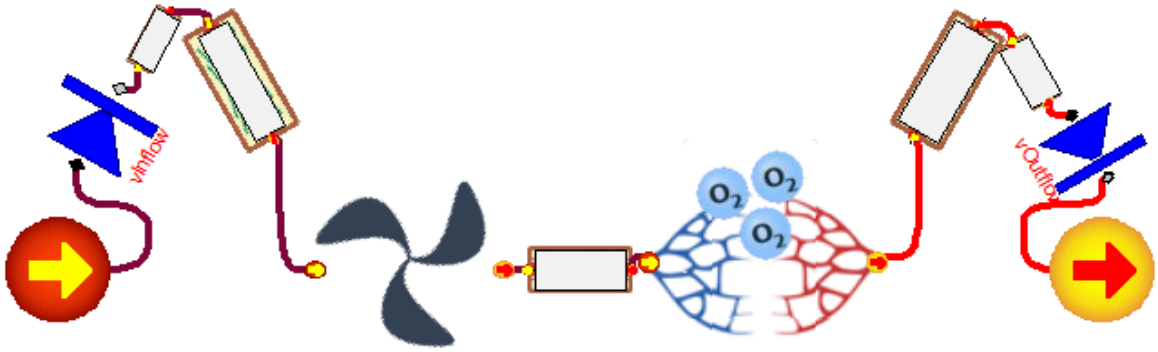

Figure 6: Modelica Scheme of Designed ECMO Model

The oxygenator module is modeled as a bunch of 80000 fibers with a diameter of 200 µm, wall thickness 50 µm, and length 15 cm. The dimensions are based on Kawahito et al. (2002) and the count of fibers has been selected so that pressure drop over the oxygenator is 110 mmHg for a blood flow of 4.5 l/min as measured by Gu et al. (2002) (which can be, however, very variable among different oxygenator devices).

The pump is located before the oxygenator, supplying additional pressure p_{ECMO} to the input pressure according to an adaptation coefficient a_ε and a difference between reference flow q_{ref} and immediate flow q through the ECMO circuit:

$$\frac{\mathrm{d}p_{ECMO}}{\mathrm{d}t} = a_\varepsilon\left(q_{ref} - q\right)$$

The coefficient a_ε has been set to 4 kPa/ml so as to delay the adaptation process a little, in an attempt to simulate real flow non-idealities (should the pump pressure really be flow controlled, the delay would represent the time needed for blood flow measurements, signal transmission, signal processing, and performing pump pressure change).

Reference flow q_{ref} depends on pulsatility of the ECMO device. In case of pulsatile flow, pulses with the duration τ_p are modeled either as square pulses (i.e. repeated switching the pump on and off) or as a parabola parametrized by peak reference flow $q_{max,ref}$ and scaling coefficient s_q:

$$q_{ref} = \begin{cases} q_{mean,ref};\ \ if\ not\ pulsatile \\ \begin{cases} q_{max,ref}\dfrac{t_c}{\tau_p};\ \ if\ t \le \tau_p \\ 0;\ \ if\ t > \tau_p \end{cases};\ \ if\ square\ pulses \\ \max\left(0, q_{max,ref} - s_q\left(t - \dfrac{\tau_p}{2}\right)^2\right);\ \ if\ parabolic\ pulses \end{cases}$$

Both parabola parameters can be found by solving for the following equations ensuring that the mean flow corresponds to the reference mean flow (with t_c being the cycle period):

$$q_{max,ref} = s_q\left(\frac{\tau_p}{2}\right)^2$$

$$q_{mean,ref} = \frac{\int_{t=0}^{\tau_p} q_{max,ref} - s_q \left(t - \frac{\tau_p}{2}\right)^2 \, \mathrm{d}t}{t_c}$$

The ECMO is attached to the cardiovascular circuit in the veno-arterial mode, i.e. draining from the end of systemic veins (corresponding to inferior vena cava) and injecting into one of supported locations – ascending aorta, aortic arch (for either of two segments), and thoracic aorta (for either of two segments). This is, however, valid only for arterial trees; simpler versions of systemic arteries are always connected via ascending aorta. In addition, extra resistance in the cannulated arterial segment is considered (in case of the derived tree only) according to insertion depth of the cannula (set to 7 mm).

By default, the ECMO device is deactivated.

2.5) Putting it Together

The model architecture has been designed in the spirit of object-oriented programing. Via the mechanism of inheritance, unnecessary code repetitions have been avoided and model components can be maintained more easily (see Appendix I for a class diagram of the main package).

2.5.1) System Integration

Interoperability between components is accomplished by Modelica connectors – special interfaces, which impose equality constraints within a group of interconnected connectors. In total, three types of connectors are used, all of them being inherited from a basic hydraulic connector in Physiolibrary, enforcing equality of pressures and equality between blood inflow and outflow. The three connectors differ only in their semantics and graphical representation, facilitating orientation in a visual editor. See an example with the model of heart in Figure 7.

All components encapsulate their logic with an exception of adaptation equations; the entire adaptation process is controlled centrally from the main model “Cardio”. This class contains all submodels assembled together and provides an entry-point for simulations.

2.5.2) Cardiac Indicators

In addition, the main model monitors a set of basic cardiac indicators (see Table 10) evaluated after each cardiac cycle. For assessment of energetic performance of the heart, cardiac power output has been selected due to its high predictive power with respect to a future treatment outcome, especially survivability, comparing to other indicators – see Fincke et al. (2004), Mendoza et al. (2007), and Lang et. al (2009).

Cardiac power output and stroke work are calculated in two variants – first, according to a mean aortic pressure as a non-invasive estimate, and second, according to a mean pressure in the left ventricle during the ejection phase. This approach should be more reliable, since the former tends to underestimate the real exerted work and power Klabunde (2014).

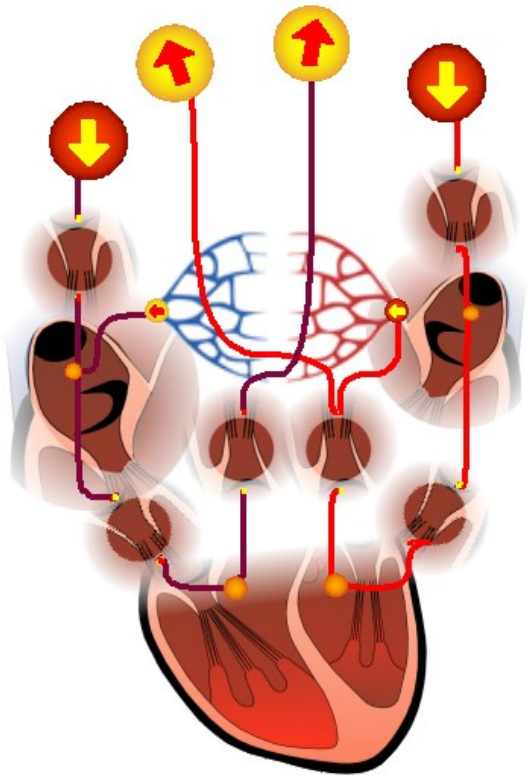

Figure 7: Modelica Scheme of Heart

Connectors of inner parts (coronaries, ventricles, atria, and valves including psudo-valves for atria venous inlets) are linked with red and dark-red-purple lines. The four big connectors at the top allows for connection to the outside environment (vessel blocks).

Variable	Indicator
HR	Heart rate
MAP	Mean aortic pressure
SVol	Stroke volume
CO	Cardiac output
SWest	Stroke work (estimate)
SW	Stroke work
CPOest	Cardiac power output (estimate)
CPO	Cardiac power output

Table 10: List of Computed Cardiac Indicators

Still, these indicators consider only mechanical energy exerted by the heart, not other forms (chemical energy, transferred heat etc.) neither real oxygen consumption, as these domains are not comprehended by the current version.

2.5.3) Graphical User Interface

Inner appearance of the main model is captured in Figure 8.

The component of systemic arteries is “replaceable” (a Modelica keyword allowing for polymorphism) and can be changed by right clicking on the component and following the context menu path “Change Class…” → ”All Matching Choices” → and selecting the desired realization (using Dymola 2014 or 2015); see Figure 9.

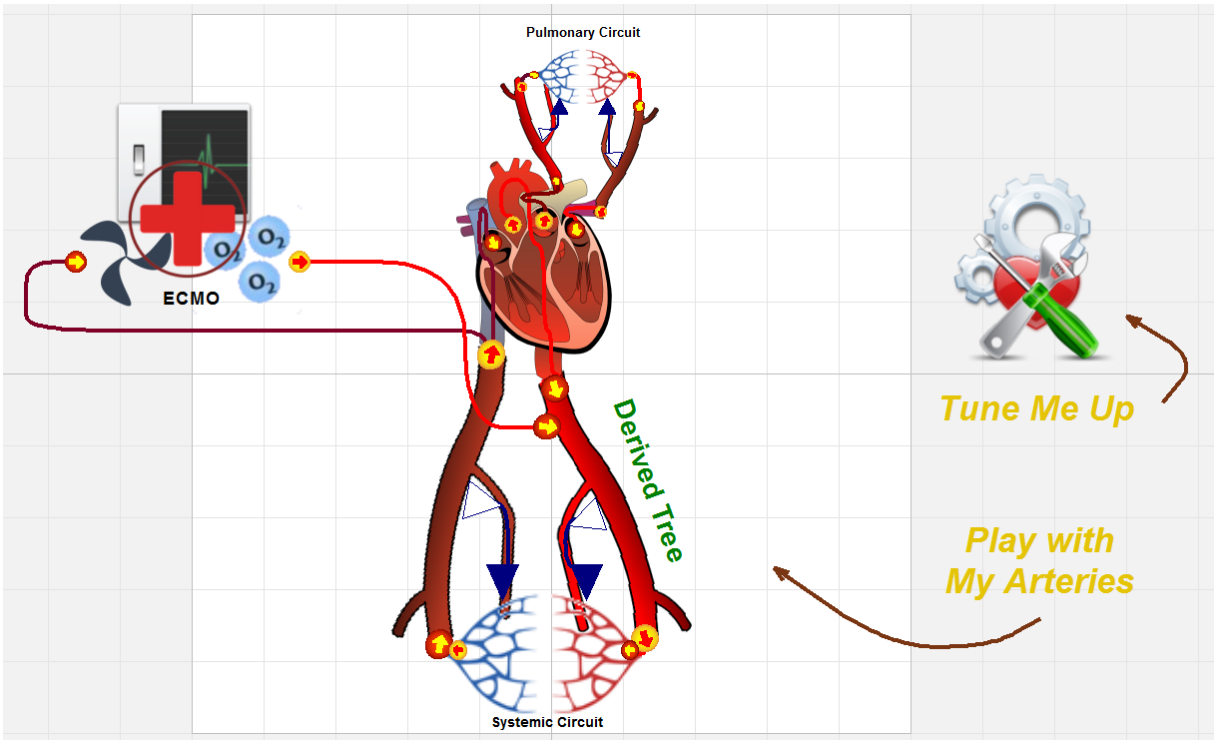

Figure 8: Modelica Scheme of the Main Model

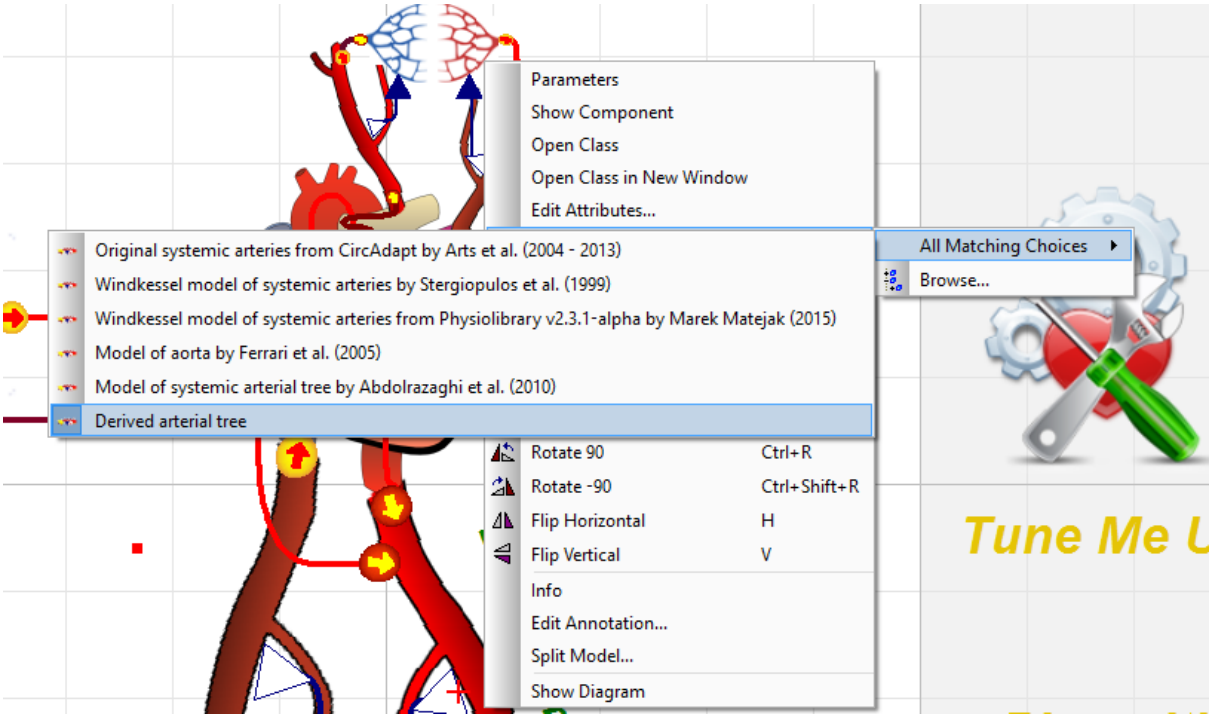

Figure 9: Selecting Component of Systemic Arteries

All other configuration is available in the Settings block, parametrized by four types of settings:

- ***Condition*** – global hemodynamic reference values, some pathologies, and adaptation
- ***Supports*** – settings for ECMO and IABP
- ***Initialization*** – specific parameters for individual instances of components
- ***Constants*** – relatively fixed values used across more instances

For each type, a pre-defined set of parameters can be selected from a drop box menu and further adjusted (see Figures 10 and 11). Parameters prefixed with "_DT_" are only supported by the derived tree version of systemic arteries. Complete overview of parameters is listed in the model documentation (see Appendix II for more information).

Alternatively, specific settings may be stored into the model code by inheriting from one of the pre-defined set or its base class and rewriting desired parameters. Afterwards, this new option will automatically appear in the selection menu. In a similar manner, new types of systemic arteries may be incorporated into the model.

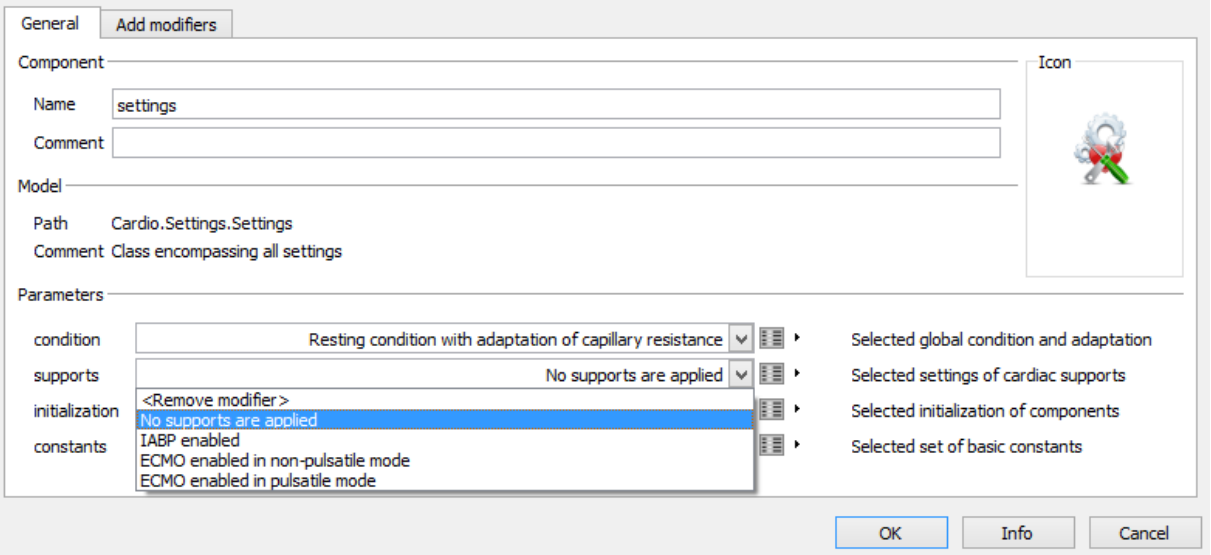

Figure 10: Selecting Settings from Pre-Defined Sets

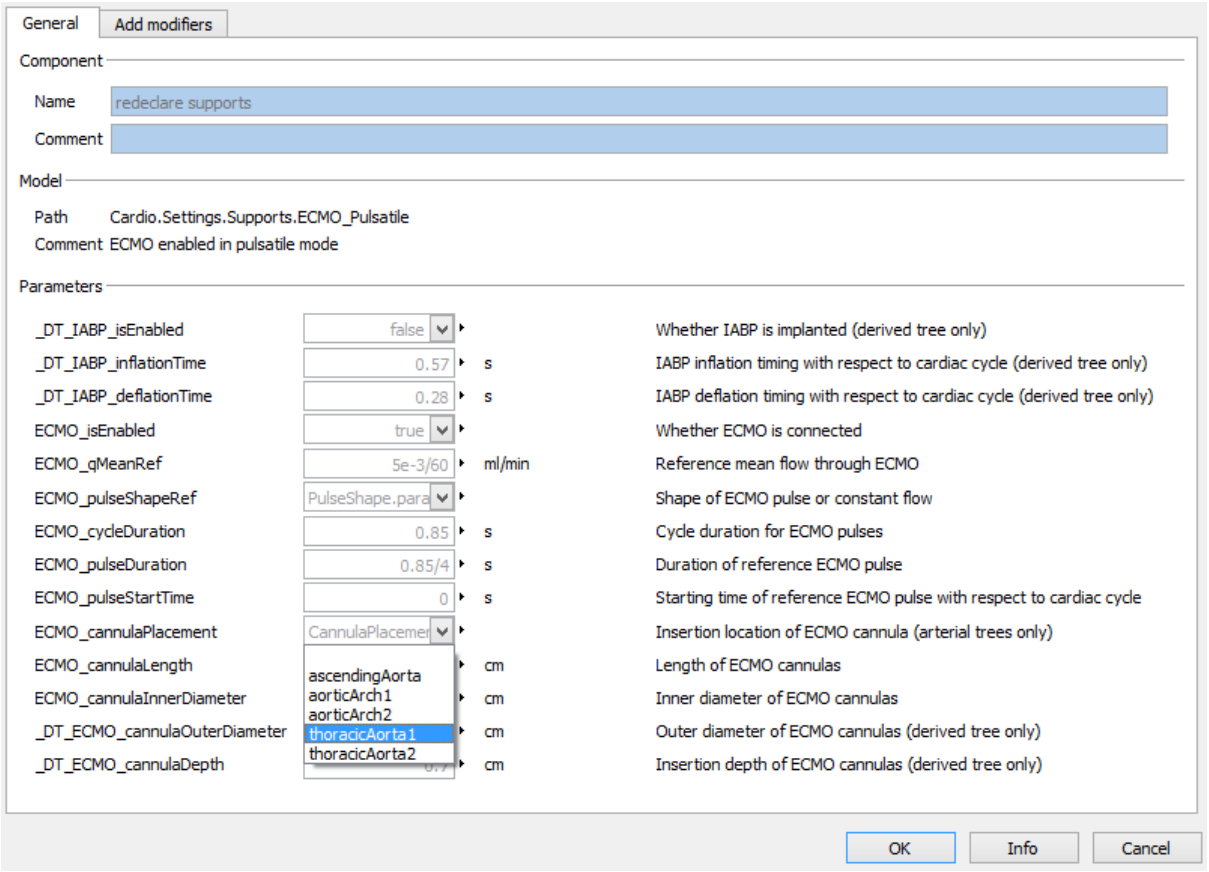

Figure 11: Adjusting Pre-Defined Settings

3) SIMULATIONS

After the entire model was constructed, it could be further investigated with regard to its physiological plausibility.

3.1) Model Preparation

First, original initial values for model components were adopted from the CircAdapt system (Maastricht University – Department of Biomedical Engineering, 2013). Nevertheless, for the model not being identical to CircAdapt but rather being a composition of various different models, the model was initiated in the adaptation protocol mode to properly adjust for the modifications.

A convergence was found in 340 seconds of simulated time. Thereafter, the simulated data were exported and processed with an auxiliary script for the MATLAB / GNU Octave environment (attached in Appendix III) to extract adapted parameters and create a new Modelica class with this settings, which can be simply copied into the model code. More precisely, due to an incompatibility in the data format for large files[6], the simulation was continued (via the "Continue" item in menu) for a short period of time and this data were exported and processed.

The adaptation, as captured with respect to aortic pressure, is depicted in Chart 1.

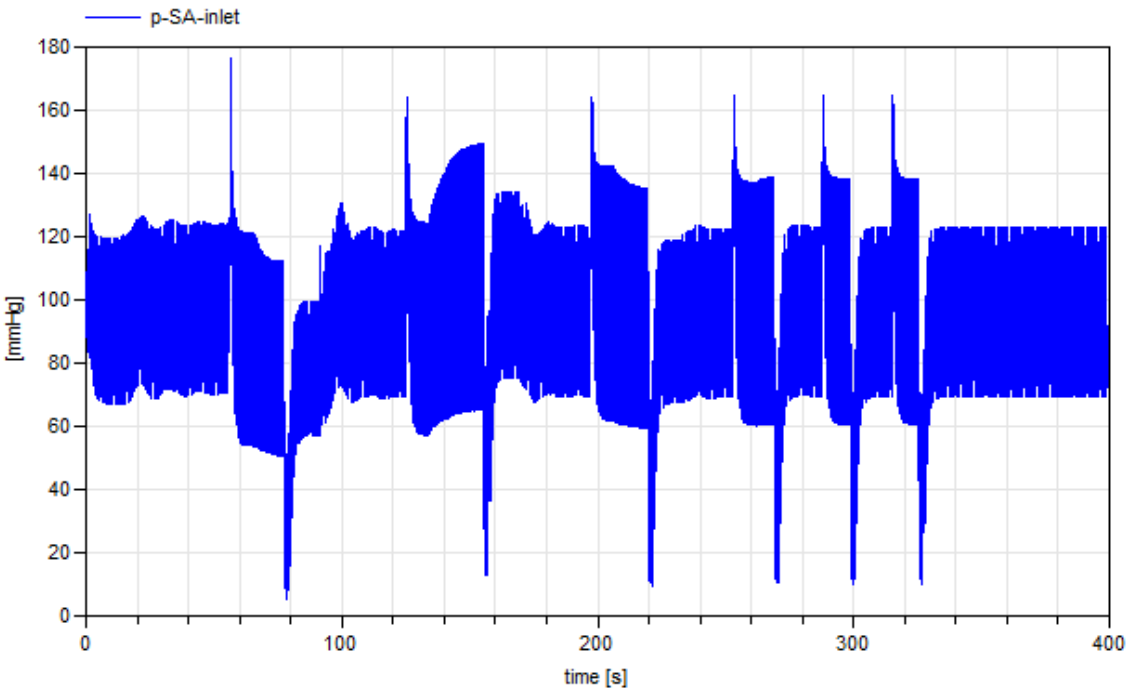

Chart 1: Aortic Pressure During the Process of Adaptation

[6] Dymola can export and import in the *.mat format; for large data, however, neither MATLAB nor GNU Octave can read such files despite using 64-bit versions.

Note the alternation of adapting phases for rest (with a lower pressure range) and exercise (with a higher pressure range). The peaks are caused by a sudden change in the phase and are followed by a period of stabilization before continuing with the adaptation.

However, after running a new simulation with the adapted settings and no adaptation enabled, the results were not in a direct correspondence with the converged solution. Based on this, it can be inferred that the inner state of the model (represented by state variables, which are changing continuously during a simulation – as opposed to parameters and constants) was consequential to preservation of the convergence and changes in the adapted parameters were overestimated.

A second run of the adaptation protocol (applied to the model with initial settings set to those found in the first pass) was much more satisfactory; using these adapted parameters, results of a new simulation with the adaptation disabled correspond to the converged solution.

The adapted parameters have been set as default. No dramatic changes have occurred during adaptation; noticeable modifications include increase in reference pressure of pulmonary veins from ca. 2.5 mmHg to 5.5 mmHg. Both sets – original and adapted – are presented in the model documentation (see Appendix II for more information).

3.2) Physiological Condition

The initial simulation was performed with the default settings for a physiological condition at rest with a minimal adaptation, i.e. adjusting capillary resistance to the blood flow.

3.2.1) Basic Setup

In this setting, the original component for systemic arteries was used.

Ventricular and arterial pressure waveforms (Chart 2) appear very realistic. The aortic pressure ranges between approximately 70 and 125 mmHg and the dicrotic notch is visible (although minute). Arterial pressures copy the wave of their ventricle until their valves close.

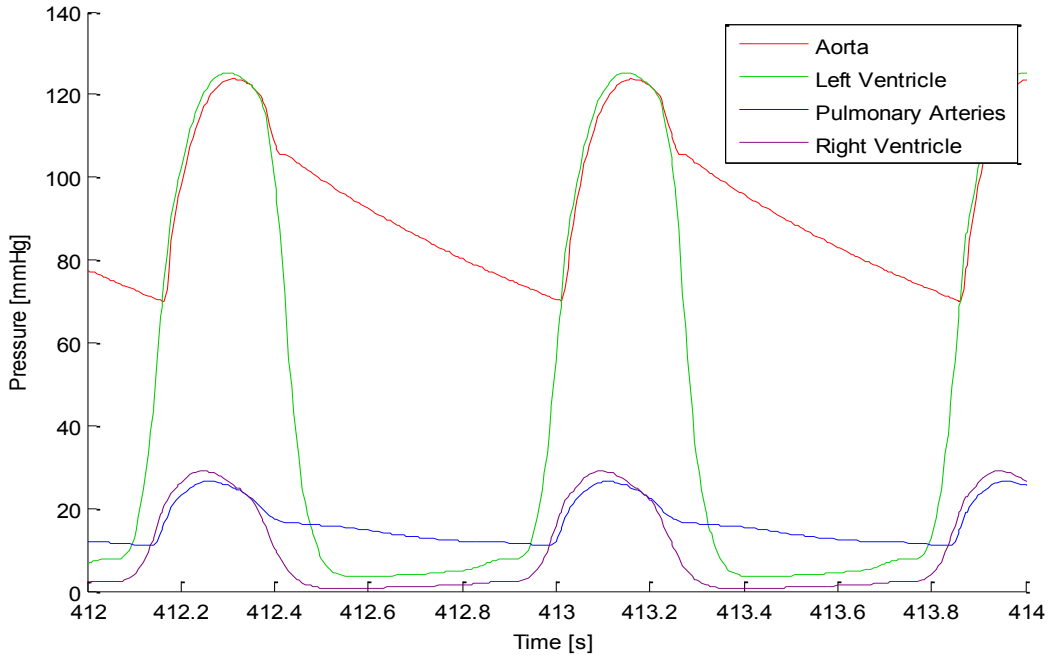

Chart 2: Pressure in Ventricles and Arteries (Physiological)

Pressure in atria and veins (Chart 3) correlate, since they are connected. Peak pressure is slightly below 9 mmHg in left atrium and around 4 mmHg in right atrium. There are two peaks during one heartbeat – one for atrial contraction (which precedes ventricular contraction for about 150 ms) and one for incoming wave from veins.

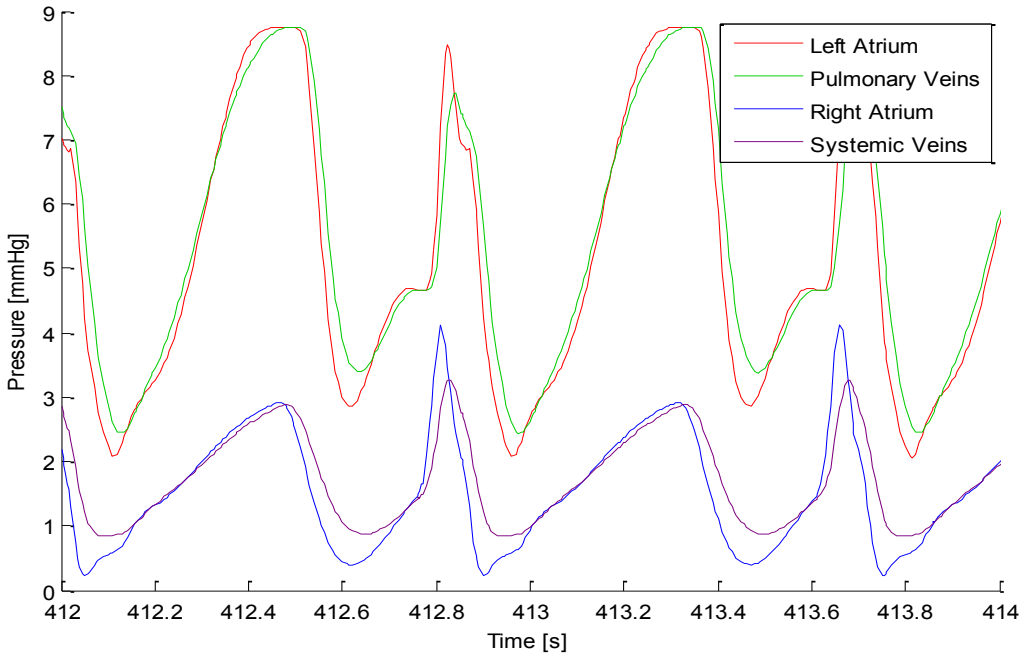

Chart 3: Pressure in Atria and Veins (Physiological)

Ventricular volume (Chart 4) is 15 ml higher in left ventricle with stroke volume around 75 ml. There is a clear convex pattern before reaching a peak volume caused by additional influx with higher pressure during atrial contraction.

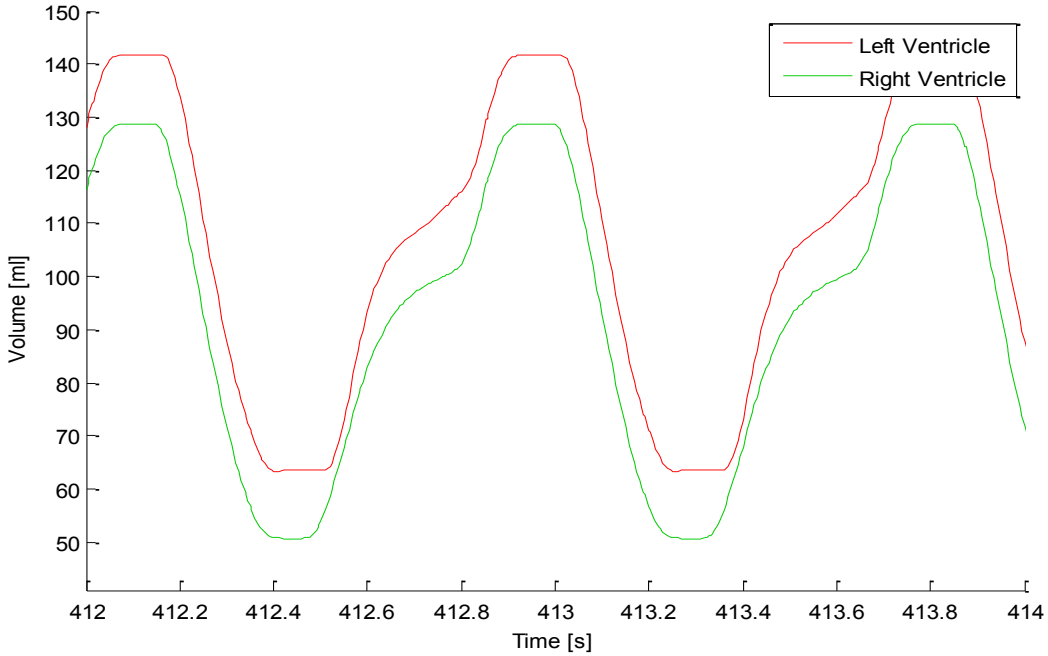

Chart 4: Ventricular Volume (Physiological)

Length of sarcomeres in ventricular walls (Chart 5) correlates with ventricular filling. Sarcomeres in the sepal wall are almost identical to those in the left wall.

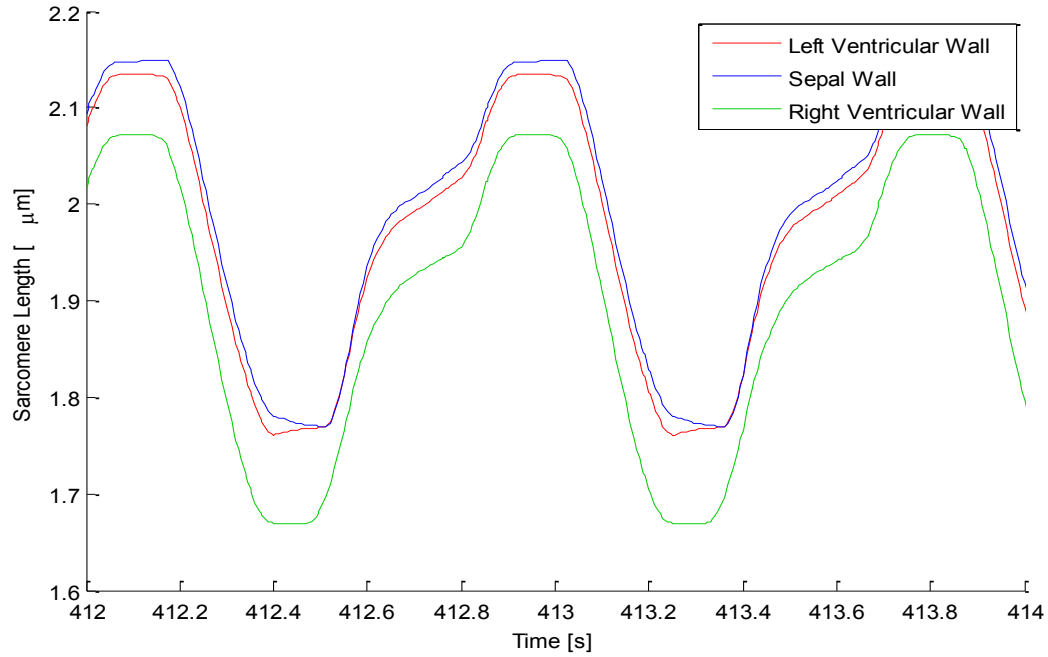

Chart 5: Sarcomere Length in Ventricles (Physiological)

Myofiber stress in ventricular walls (Chart 6) consists mostly of the active compound caused by fiber contractions and is higher in the left wall. Peaks in active stress correspond to systole whereas peaks in passive stress reflect ventricle diastole, as the passive stress is caused by fiber stretching.

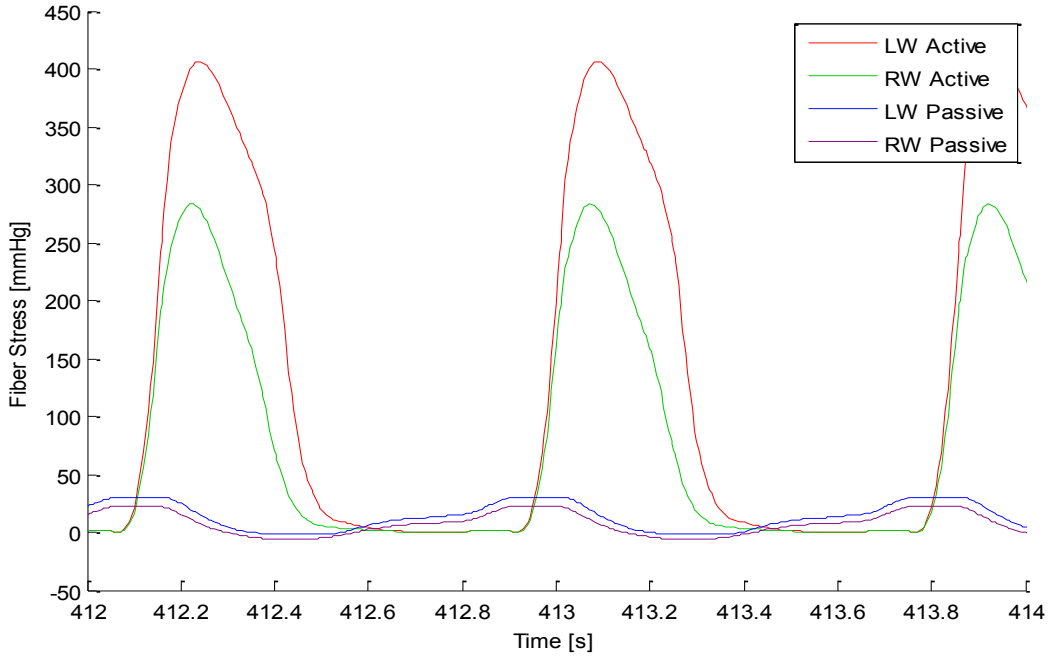

Chart 6: Myofiber Stress in Ventricles (Physiological)

Sarcomere length in atria (Chart 7) is in the similar range as in case of ventricles. Left atrium is being stretched a little more.

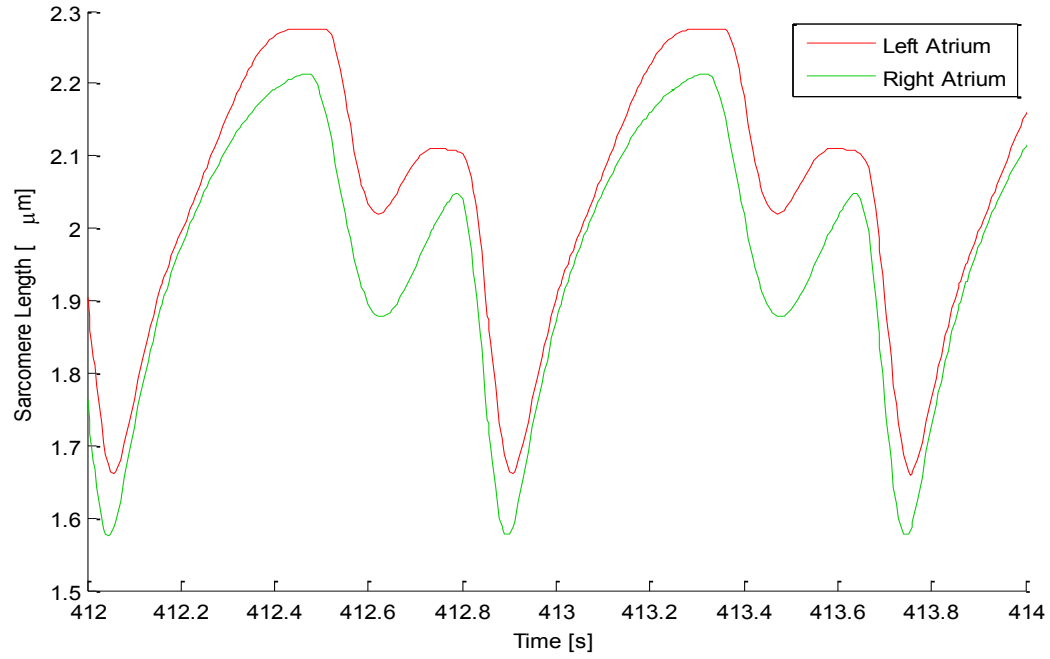

Chart 7: Sarcomere Length in Atria (Physiological)

In contrast to ventricles, the main compound of myofiber stress in atria (Chart 8) is the passive stress, illustrating higher sensitivity of atrial fibers to stretch (Arts et al., 2004). The decomposition into passive and active compound also explains both peaks in atria pressure waveforms as seen in Chart 3.

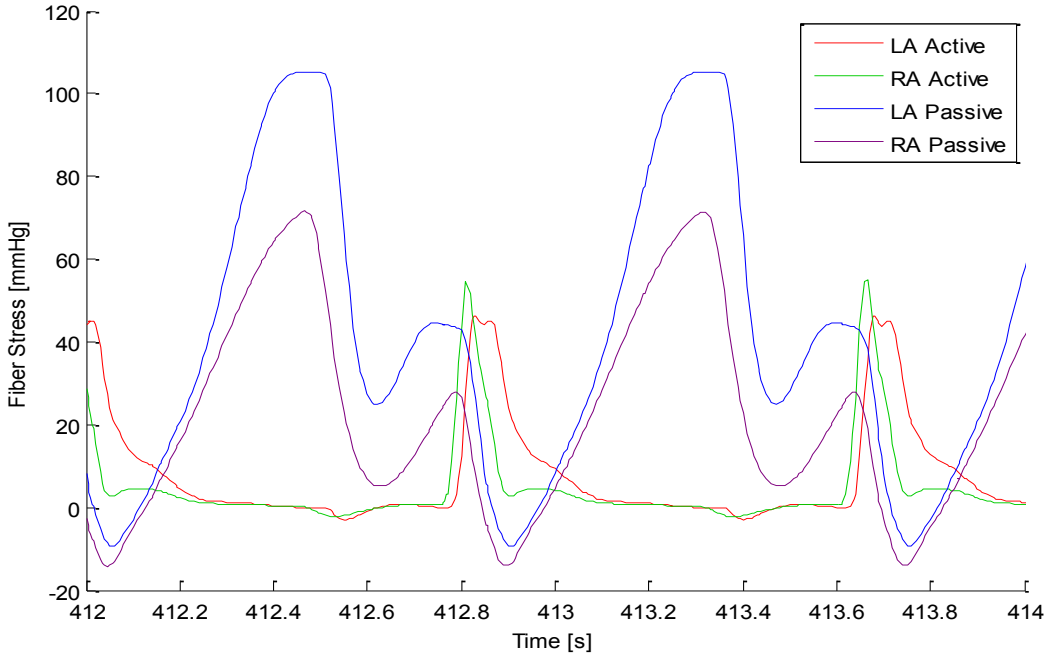

Chart 8: Myofiber Stress in Atria (Physiological)

Blood flow through valves of left ventricle (LV) (Chart 9) illustrates the systolic (flow through the aortic valve) and diastolic (flow through the mitral valve) period. Note the little backward flux before the aortic valve closes reflecting a (pressure-dependent) closing time interval.

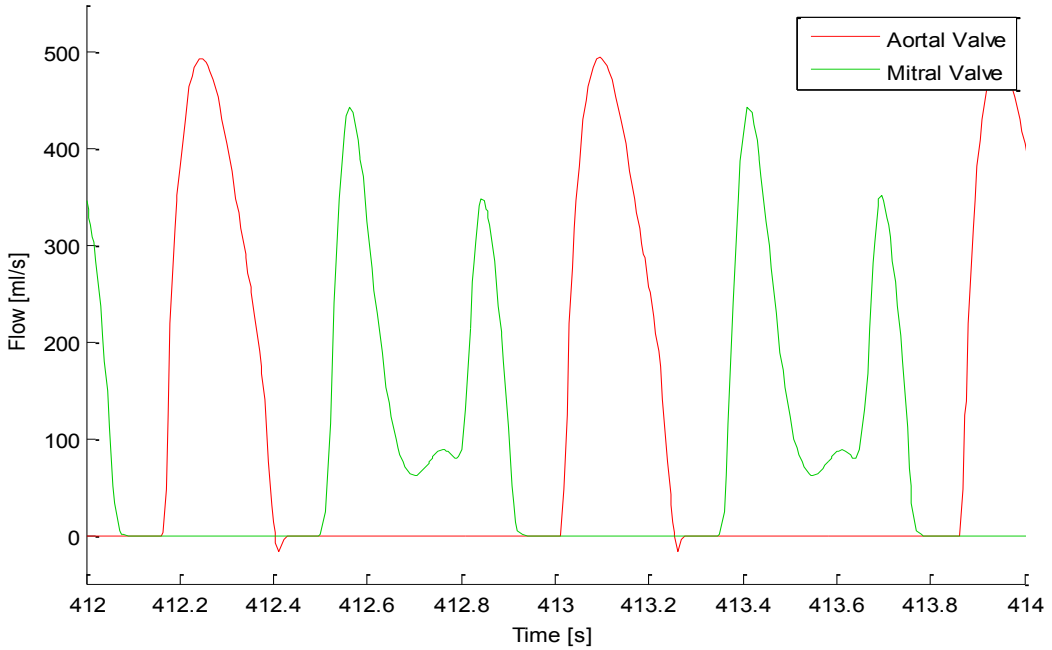

Chart 9: Flow Through LV Valves (Physiological)

The situation in valves of the right ventricle (RV) (Chart 10) is similar.

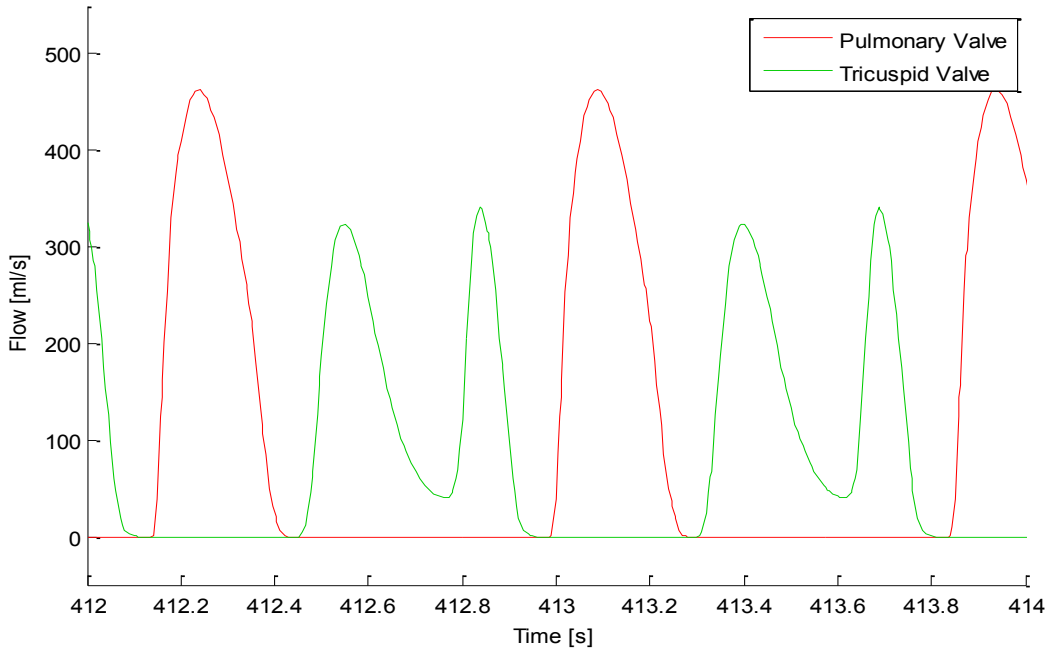

Chart 10: Flow Through RV Valves (Physiological)

Pericardial pressure (Chart 11) increases during fiber contraction – the first peak corresponds to the atrial contraction while the second, more intensive mirrors the ventricular contraction.

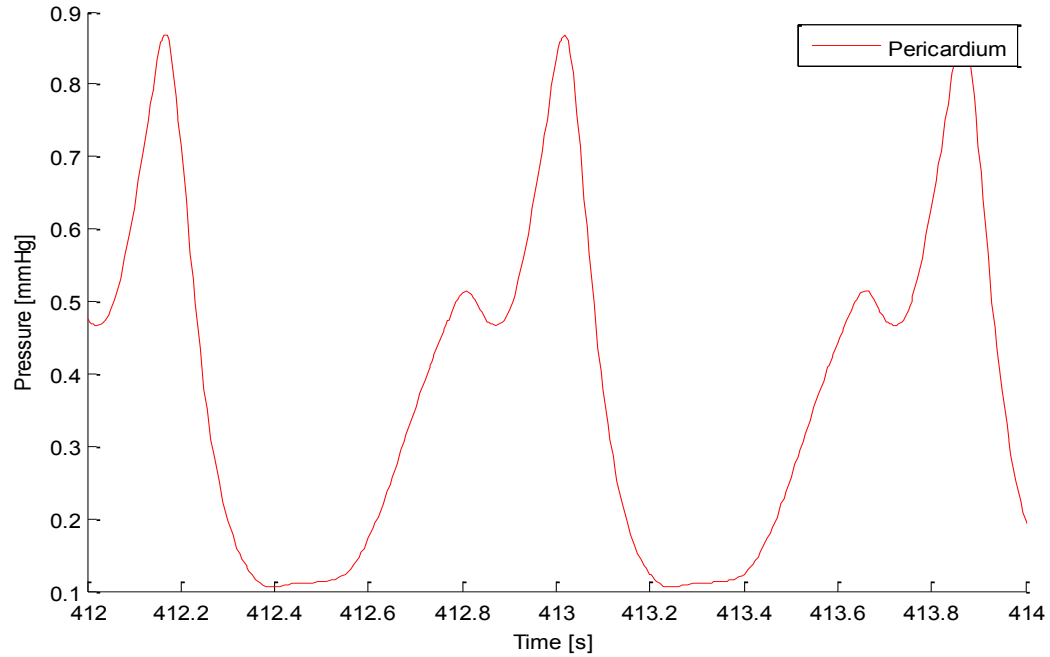

Chart 11: Pericardial Pressure (Physiological)

Coronary myocardial pressure and intramyocardial pressure in left ventricle (Chart 12) are closely correlated together and to ventricular pressure. It is in accordance with the results of the original coronary model of Bovendeerd et al. (2006).

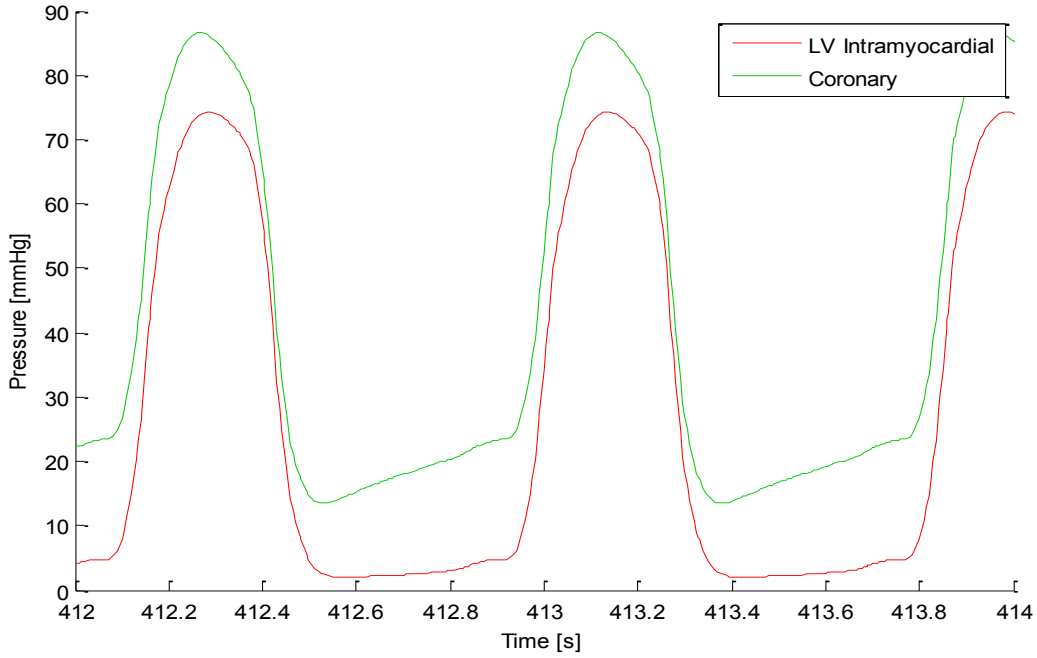

Chart 12: Coronary and Intramyocardial Pressure (Physiological)

Flow through coronary arteries (Chart 13) is higher during heart diastole, which is also physiologically valid and explained by variations in radius of myocardial vessels rather than their pressure gradient (Bovendeerd et al., 2006).

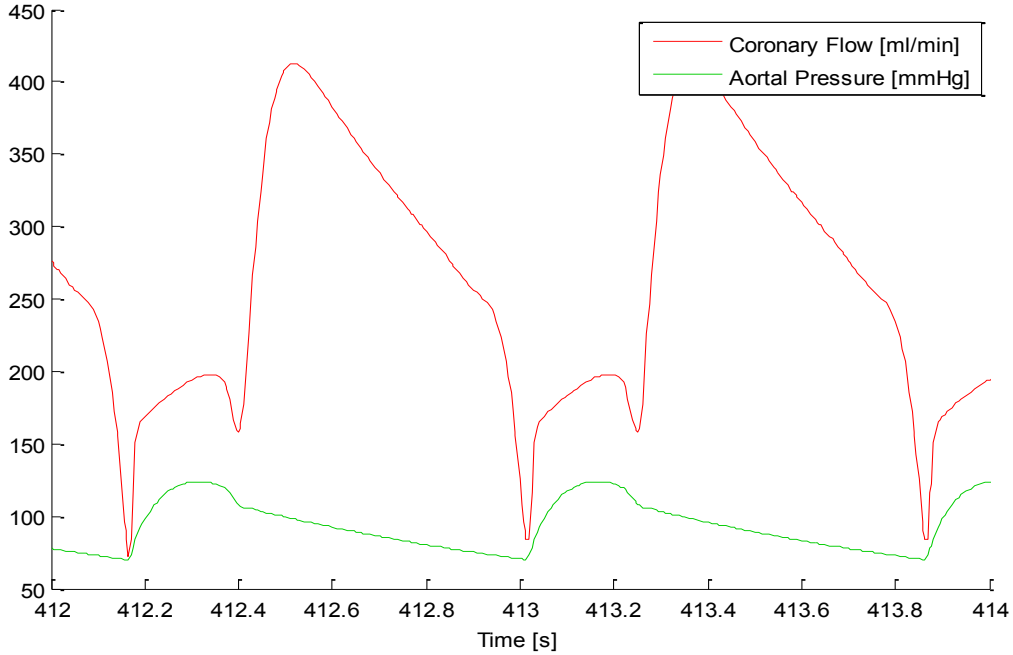

Chart 13: Coronary Flow (Physiological)

Monitored cardiologic indicators are summarized in Table 11. Note that the estimates of stroke work and cardiac power output are underestimated as expected.

Indicator	Value	Unit
HR	71	bpm
MAP	94	mmHg
SVol	74	ml
CO	5223	ml/min
SWest	0.92	J
SW	1.12	J
CPOest	1.09	W
CPO	1.32	W

Table 11: Values of Cardiac Indicators in Physiological Settings

3.2.2) ECMO Pulses

After connecting to the ECMO device with reference mean flow 5 l/min, the differences between pulse types and between reference (ideal) and resulting flow can be compared (Chart 14). Distortion is present in all three cases although the total impact on mean flow is negligible. Effects of ECMO on the cardiovascular system are examined later (Section 3.6).

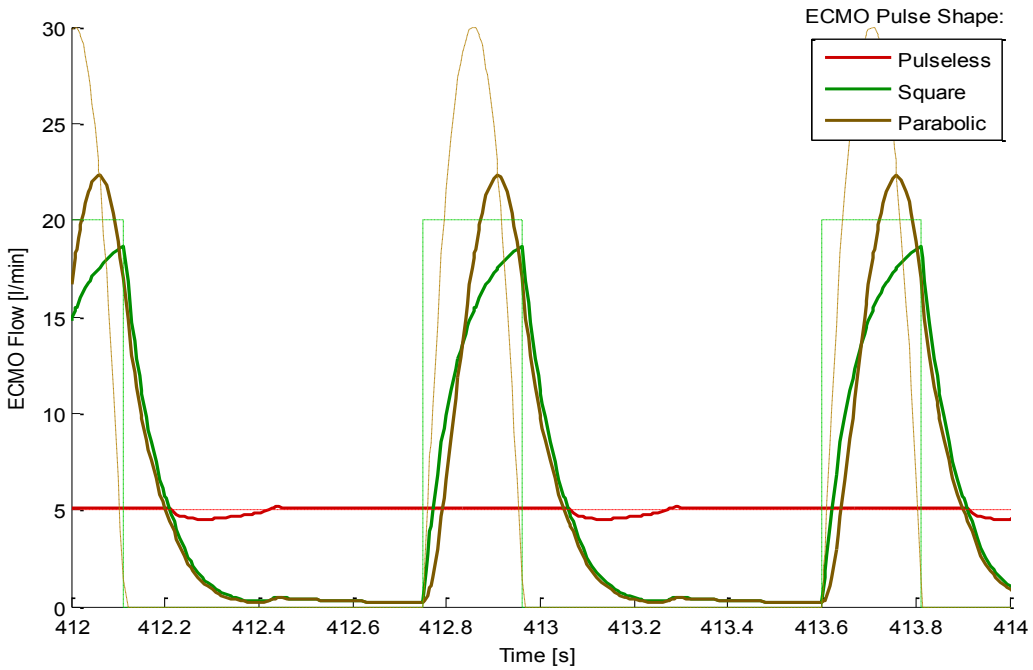

Chart 14: ECMO Pulses

Dashed lines – computed reference flow, Full line – resulting flow through ECMO

3.2.3) Substituting Models of Systemic Arteries

Afterwards, the original component of systemic arteries was replaced by the other models and the resulting aortic pressure waveform was compared with the original one.

The first windkessel model (Chart 15), defined by Stergiopulos et al. (1999), performs very attractively. The pressure ranges between 80 and 130 and the dicrotic notch is more visible than in the original model.

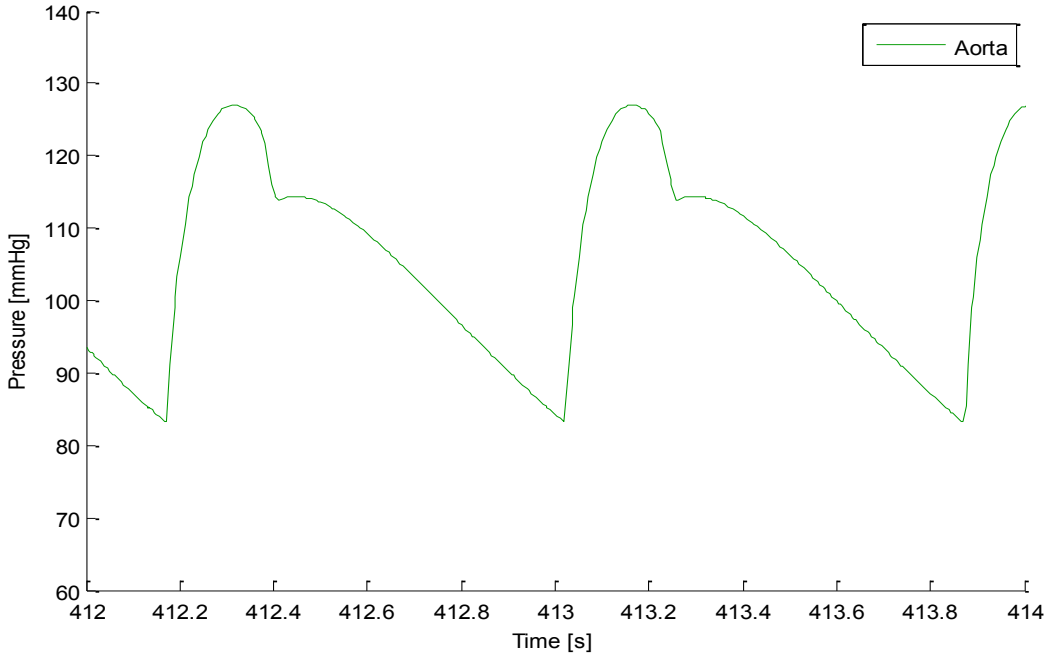

Chart 15: Aortic Pressure using Windkessel Model by Stergiopulos (Physiological)

The second windkessel model (Chart 16), adopted from Physiolibrary (Institute of Pathological Physiology, Charles University in Prague, 2015), reaches the same pressure range in aorta although the dicrotich notch is not apparent.

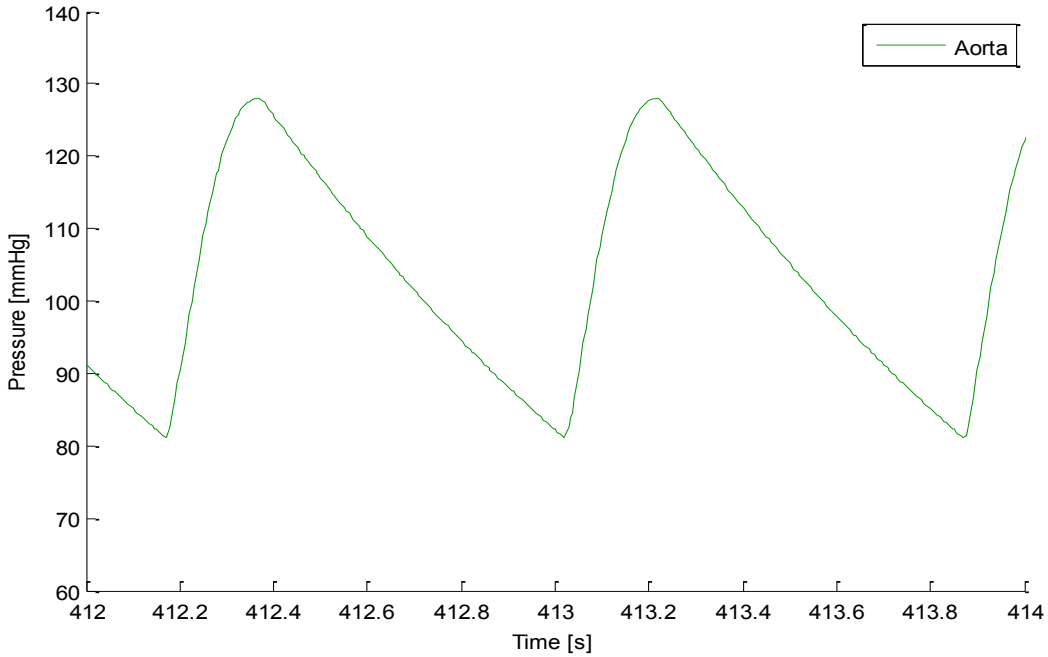

Chart 16: Aortic Pressure using Physiolibrary Windkessel Model (Physiological)

The model of aorta constructed by Ferrari et al. (2000) (Chart 17) performs rather disappointingly. There are high pressure reflections in both ascending and abdominal aorta and the overall waveform is not in correspondence with their results. This can be explained by assuming that resistive elements connected to the aortic core include all capillary resistance, effectively leading to its duplication in the scope of the model.

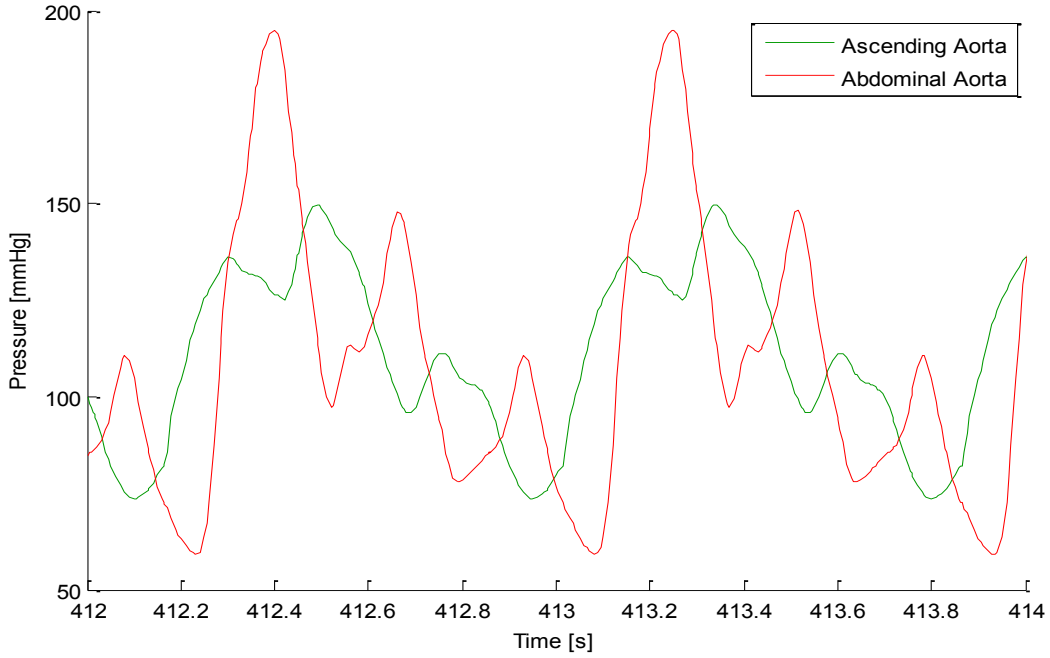

Chart 17: Aortic Pressure using Simple Aortic Model (Physiological)

After an adjustment in the resistance of peripheral elements (decrease by 75 %), the waveforms (Chart 18) correspond to those presented in the original paper (Ferrari et al., 2000) although there are still a little higher (especially abdominal aorta). The wave amplification in abdominal aorta reaches almost 40 mmHg, which is not entirely feasible. It can be concluded that this model of aorta is not fully compatible with the whole model.

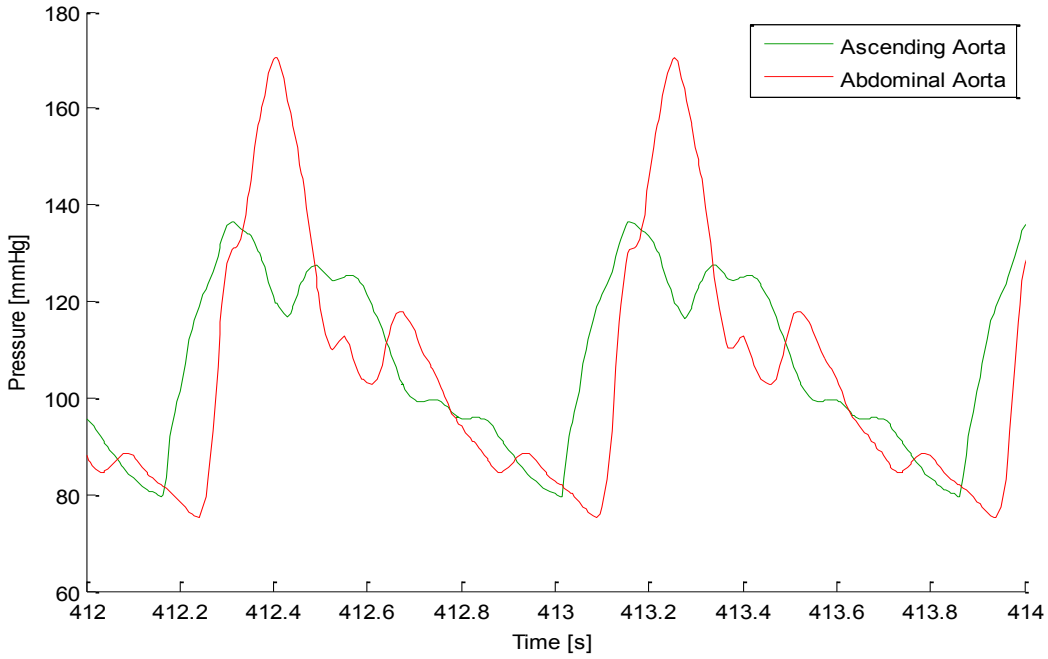

Chart 18: Aortic Pressure using Aortic Model with Adjusted Resistance (Physiological)

The arterial tree by Abdolrazaghi et al. (2010) (Chart 19) is of a valid pressure range between 70 and 125 mmHg in aorta and with 10mmHg amplification in femoral artery. The shape of aorta pressure waveform is, however, not nearly ideal – although, in fact, it is completely identical to the results in their paper.

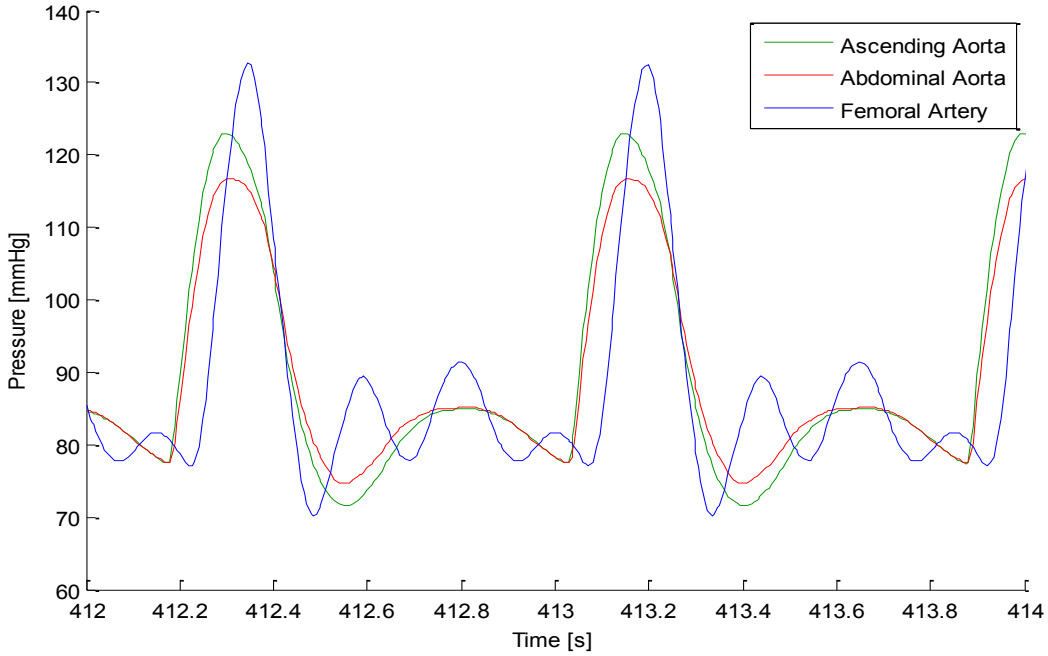

Chart 19: Aortic and Femoral Pressure using Simple Arterial Tree (Physiological)

The derived tree based on physiological arterial dimensions listed by Avolio (1980) (Chart 20) also exhibits a common physiological condition with a pressure range between 80 and 130 mmHg in aorta and between 75 and 140 mmHg in other parts of the tree.

There is a small notch caused by closure of the aortic valve (located slightly below 110 mmHg) and a more apparent dicrotic notch caused by a wave reflection from distant parts of the tree. It might be seen as a little exaggerated, which can result from simplifications in modeling branching resistance.

Pressure in femoral artery is amplified by 10 mmHg. Similarly, there is a pressure difference between left and right common carotid around 10 mmHg, which can be also attributed to the simplified branching resistance.

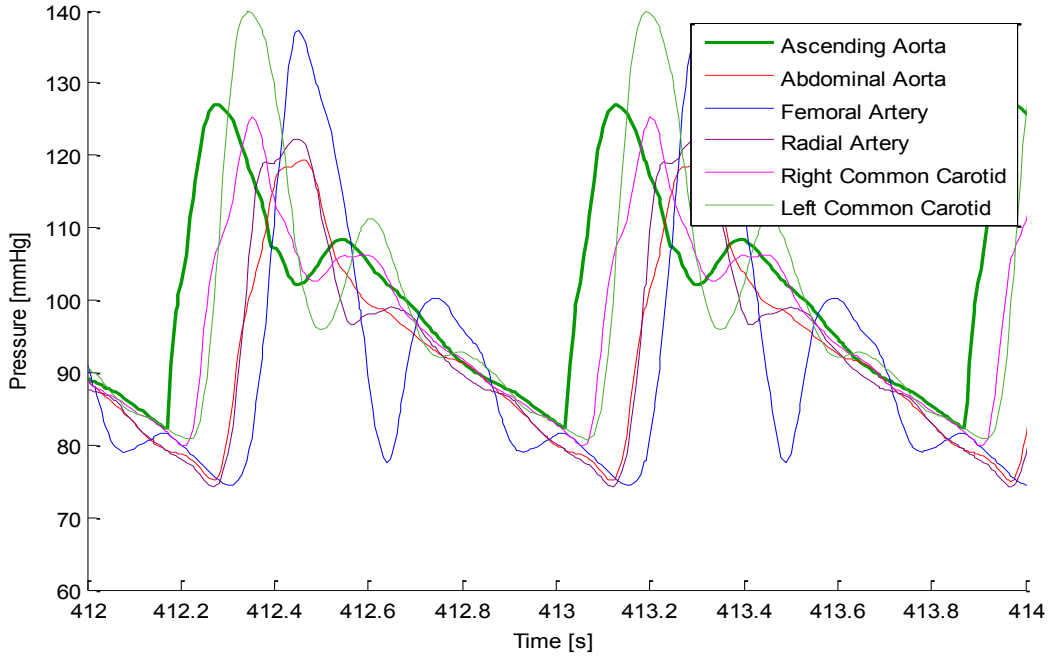

Chart 20: Pressure Waveforms using Derived Arterial Tree (Physiological)

3.2.4) Summary

In the basic setup, all simulated results appear realistic and no significant deviations from physiological ranges have been detected. This suggests plausibility of the model with a potential of predictive power and maybe even suitability for usage as a source for quantitative analyses.

Both windkessel models as well as the arterial trees except for the aortic model by Ferrari et al. (2010) have been successfully implemented into the presented model and have been found fully compatible with the circuit (having the right pressure range and a shape corresponding to results of their authors).

This suggests that the model is flexible enough to allow for replacements of its parts by independent components according to an objective being pursuit. It can be argued that this and the results are signs of a physiological plausibility of the model.

In further simulations, an arterial tree was needed to observe flow and pressure patterns in various parts of the tree. As already stated, the first model of aorta was found incompatible. From the

remaining two trees, the complex derived tree was selected for its more attractive pressure curves across the tree.

3.3) Pathological Conditions I: Blood Volume and Heart Contractility

After examination of the model behavior for the physiological state and selection of the most promising arterial tree, various pathological conditions were simulated and explored with the main emphasis on their qualitative impact.

All simulations employ the derived arterial tree and the resting condition with minimal adaptation (capillary resistance adjustments) unless stated otherwise.

3.3.1) Hypovolemia

In this condition, the total (stressed) blood volume was gradually decreased from 100 % to 50 % by 10% steps, simulating acute bleeding.

Aortic pressure (Chart 21) is decreasing with virtually equidistant pressure drops.

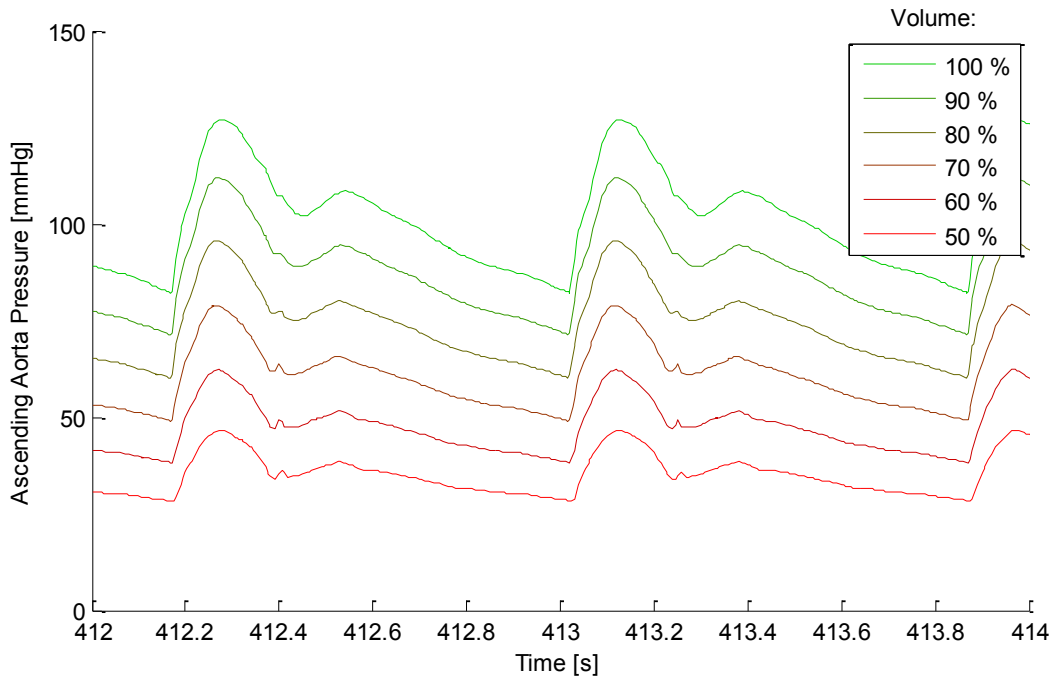

Chart 21: Aortic Pressure (Hypovolemia)

Similarly, pressure in pulmonary veins (Chart 22) is also dropping.

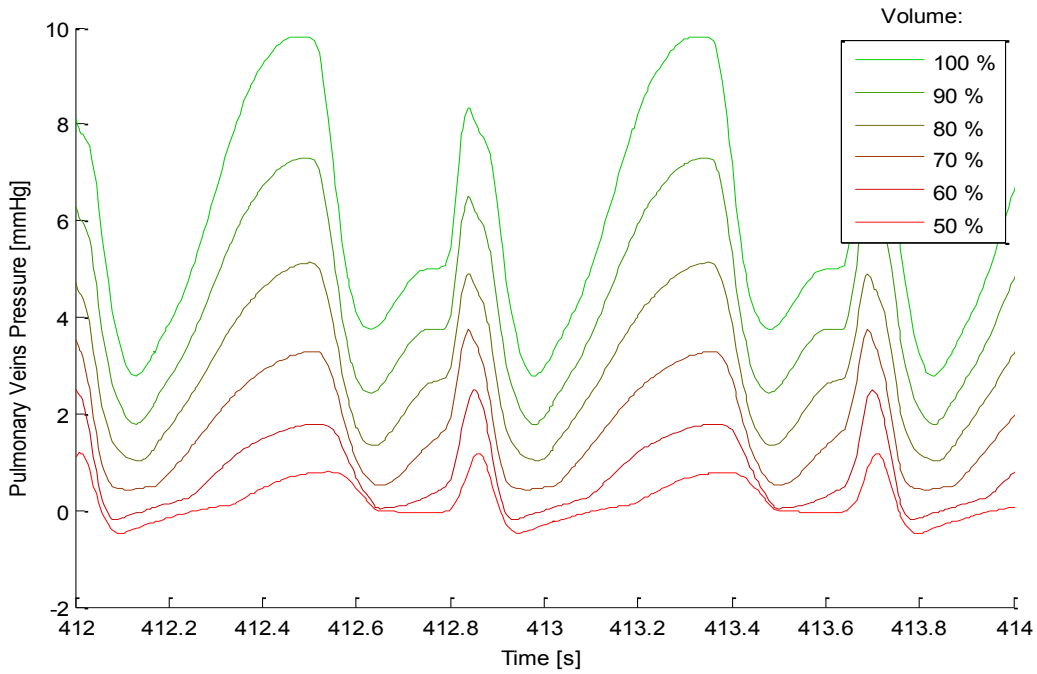

Chart 22: Pulmonary Veins Pressure (Hypovolemia)

Left ventricular volume as well as pressure (Chart 23) steadily declines. The ventricle is less filled during diastole although it is contracting more due to low afterload.

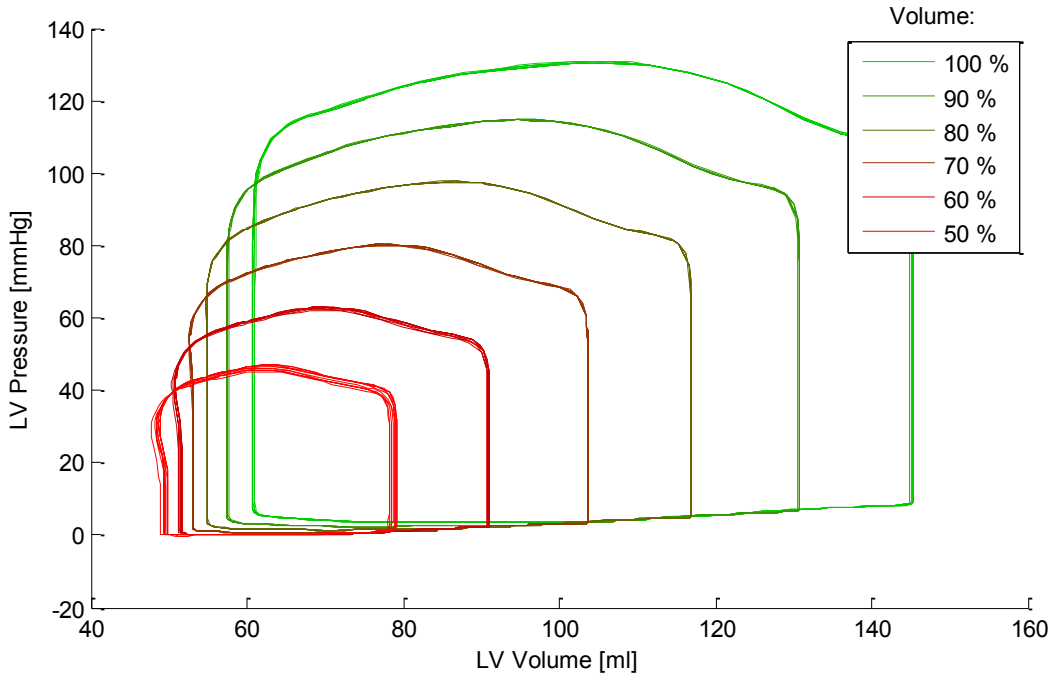

Chart 23: LV p-V Diagram (Hypovolemia)

In right ventricle, the filling volume is also dropping (Chart 24) while the end-systolic volume is increasing, meaning less intense contractions.

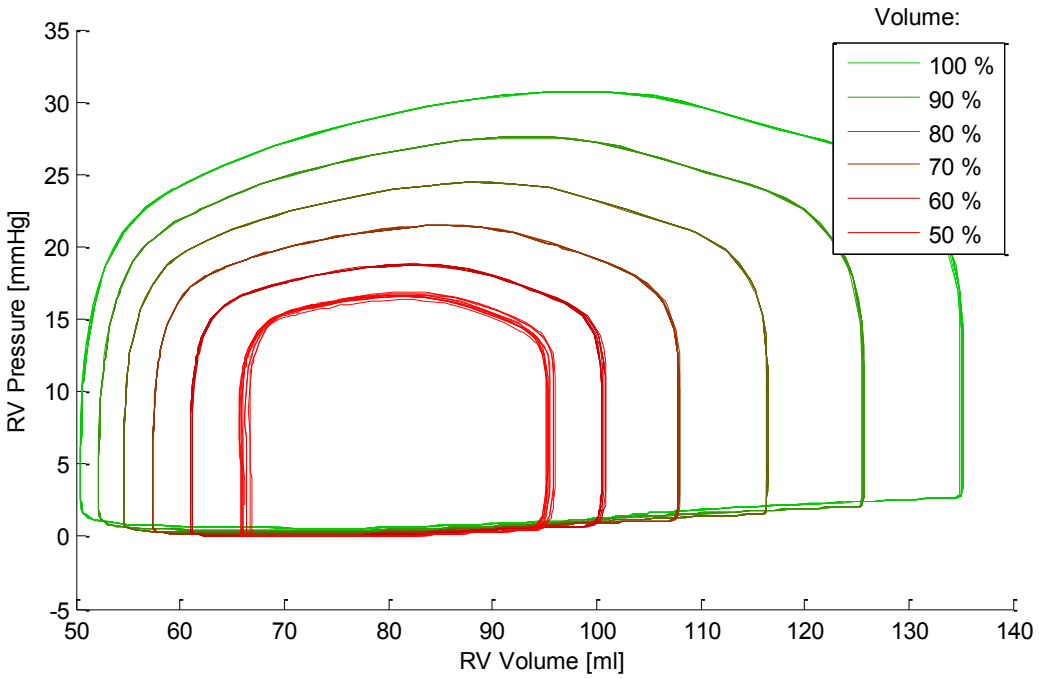

Chart 24: RV p-V Diagram (Hypovolemia)

Stroke volume and mean aortic pressure (Chart 25) are decreasing linearly.

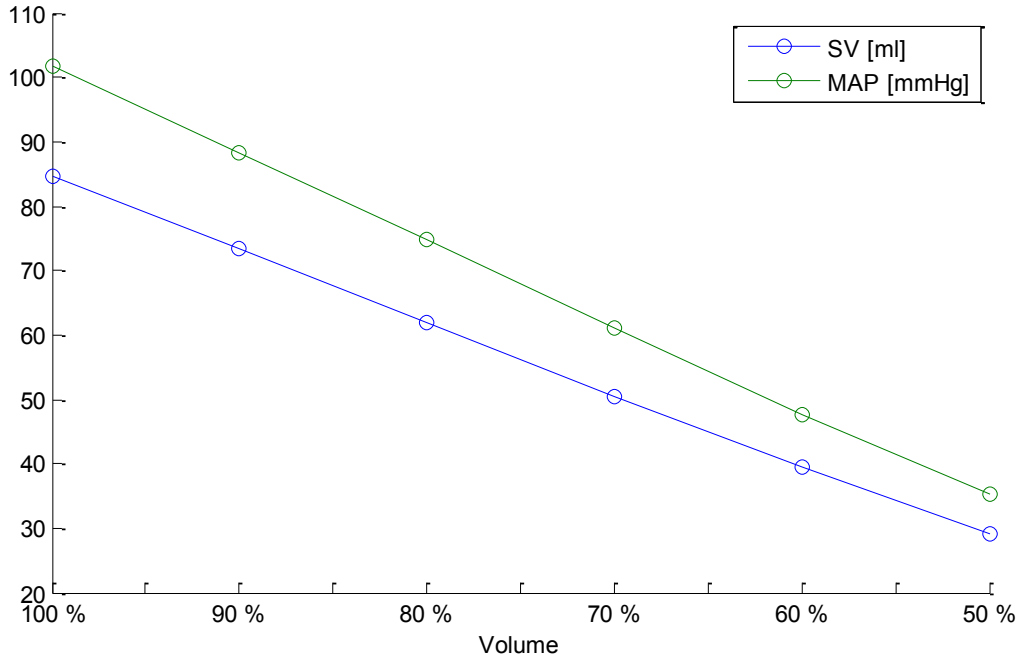

Chart 25: Stroke Volume and Mean Aortic Pressure (Hypovolemia)

Sarcomere length in the left heart wall (LW) (Chart 26) is stretching less, which is related to the low diastolic filling.

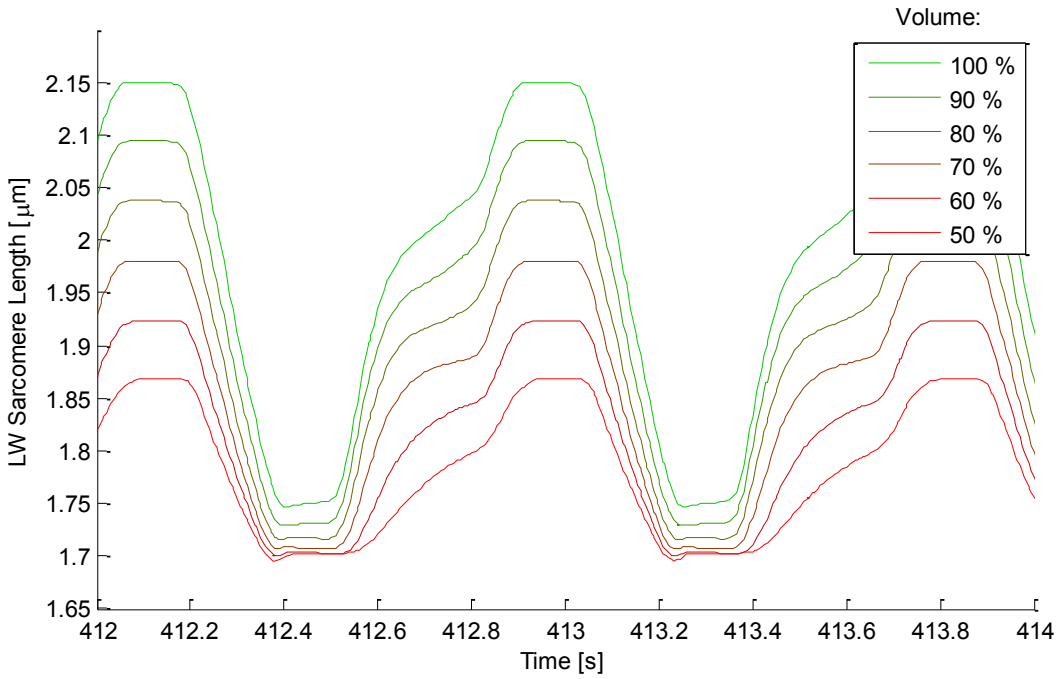

Chart 26: LW Sarcomere Length (Hypovolemia)

Fiber stress in the left ventricular wall (Chart 27) is falling – the contraction is much less intensive.

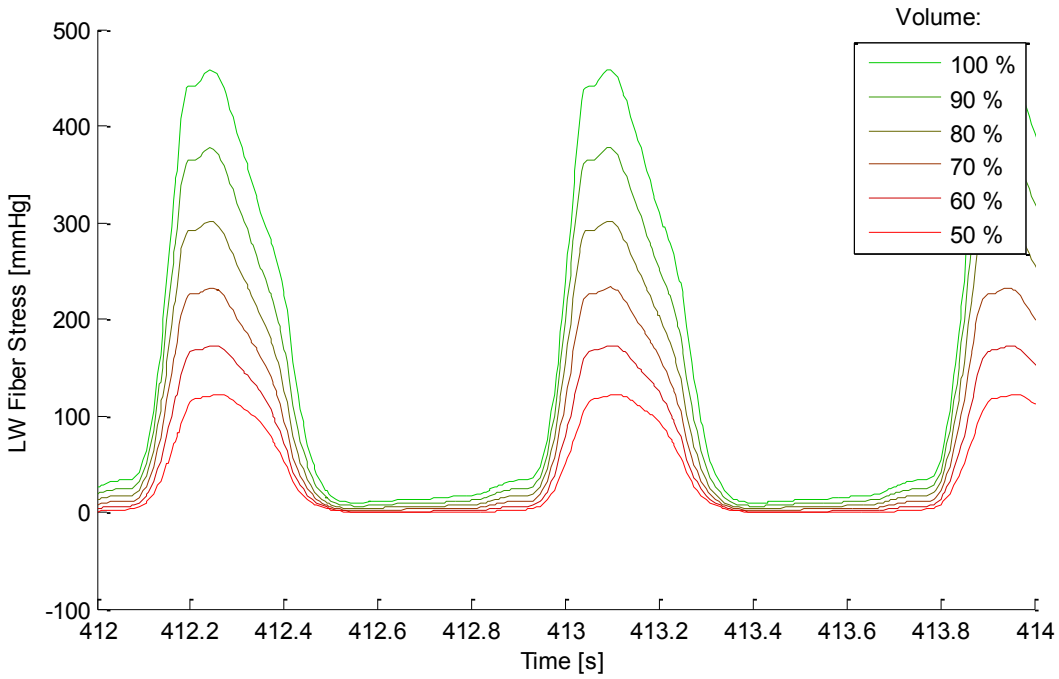

Chart 27: LW Myofiber Stress (Hypovolemia)

Cardiac power output and stroke work (Chart 28) are decreasing – less stroke volume means less hemodynamic work done and less power exerted.

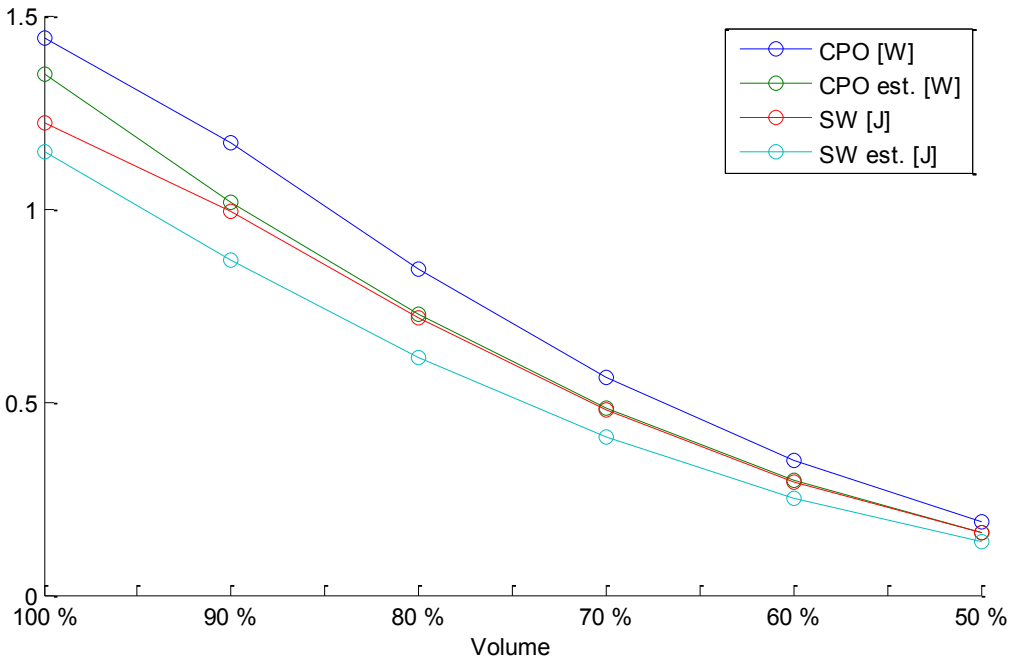

Chart 28: Cardiac Power Output and Stroke Work (Hypovolemia)

Plotting cardiac output in relation to end-diastolic myocardial wall stress (Chart 29), i.e. preload as defined by Norton (2001), results in almost linear relationship. This curve is known as a cardiac function curve –higher preload leads to higher cardiac output.

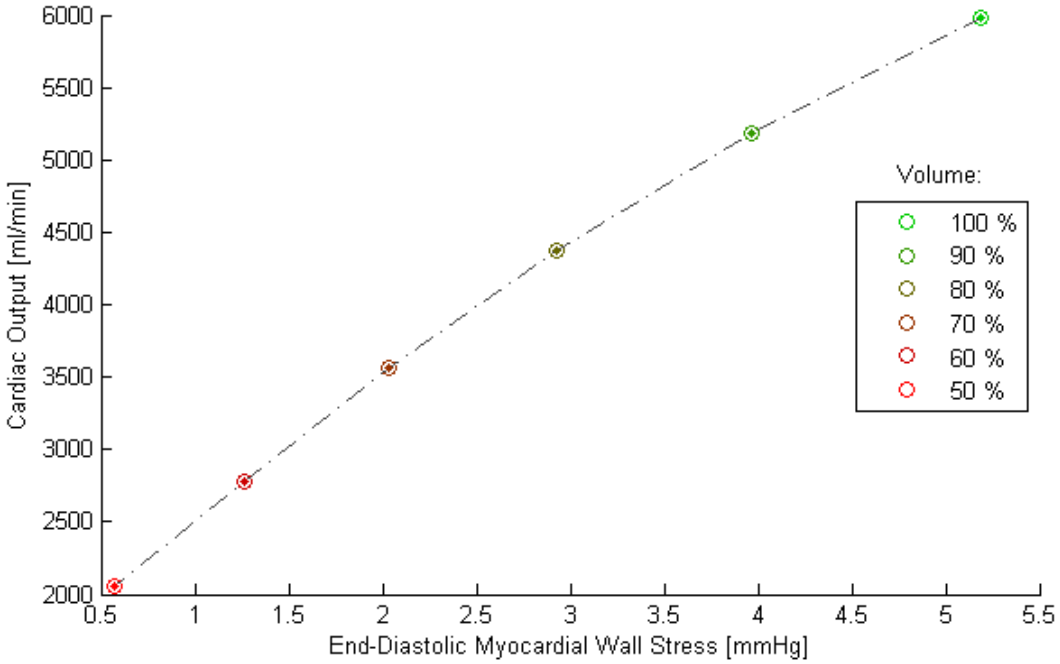

Chart 29: Preload and Cardiac Output Dependency (Hypovolemia)

3.3.2) Hypovolemia with Regulated Response

In the previous scenario, no body response to the condition was considered. In reality, when a large volume of blood is lost (and the subject is still living), the autonomic nervous system will react by increasing heart rate to maintain proper blood circulation and by vasoconstriction in an attempt to prevent from further blood loss.

This scenario is described and simulated in Dassen et al. (2011). Although the exact values are not mentioned, the settings used here involve double increase in both heart rate and reference systemic resistance in response to loss of 50 % of blood volume.

As a result, aortic pressure (Chart 30) is improved to values around 100 mmHg although with relatively small differences between systolic and diastolic pressure. This is typical for a shock condition.

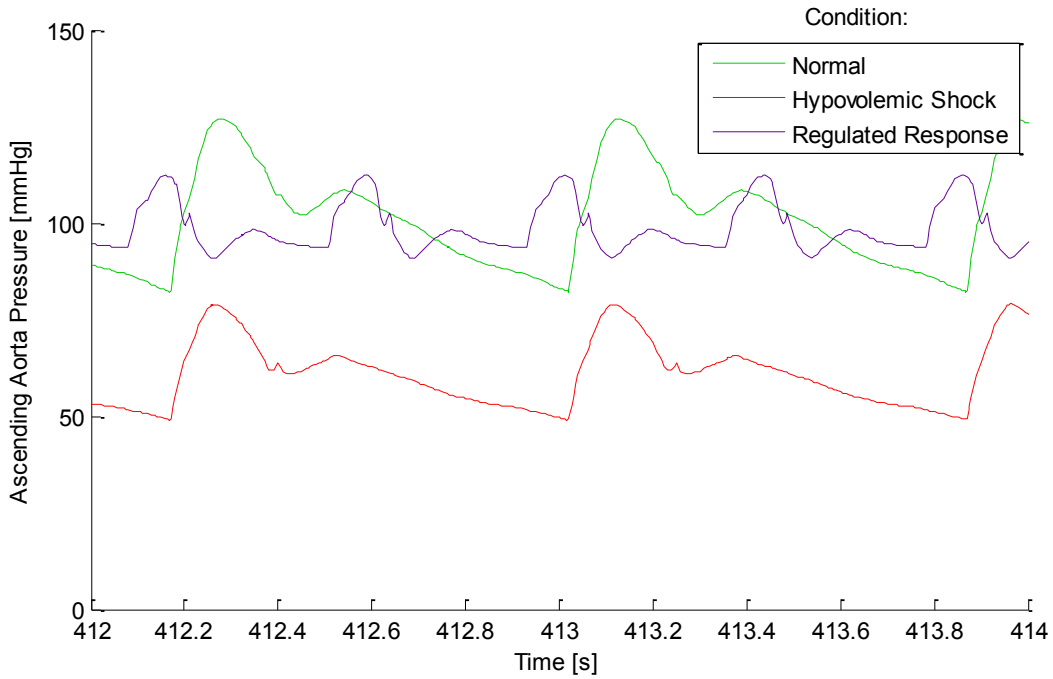

Chart 30: Aortic Pressure (Hypovolemia with Body Response)

The p-V diagram of left ventricle (Chart 31) shows a decrease in the stroke volume.

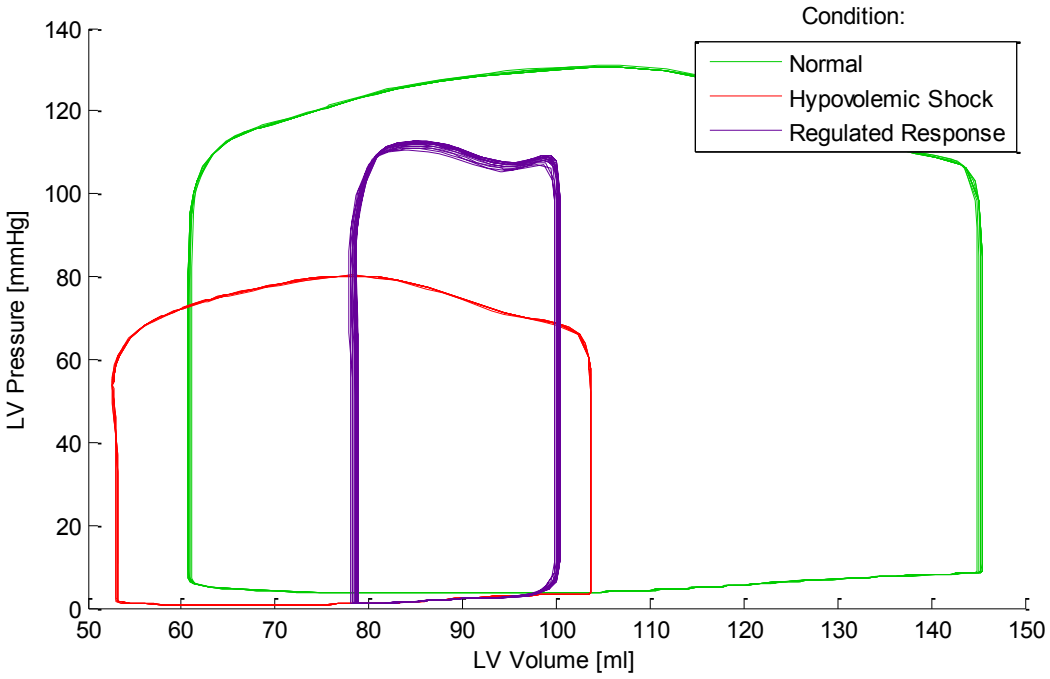

Chart 31: LV p-V Diagram (Hypovolemia with Body Response)

Filling of the right ventricle (Chart 32) is further reduced.

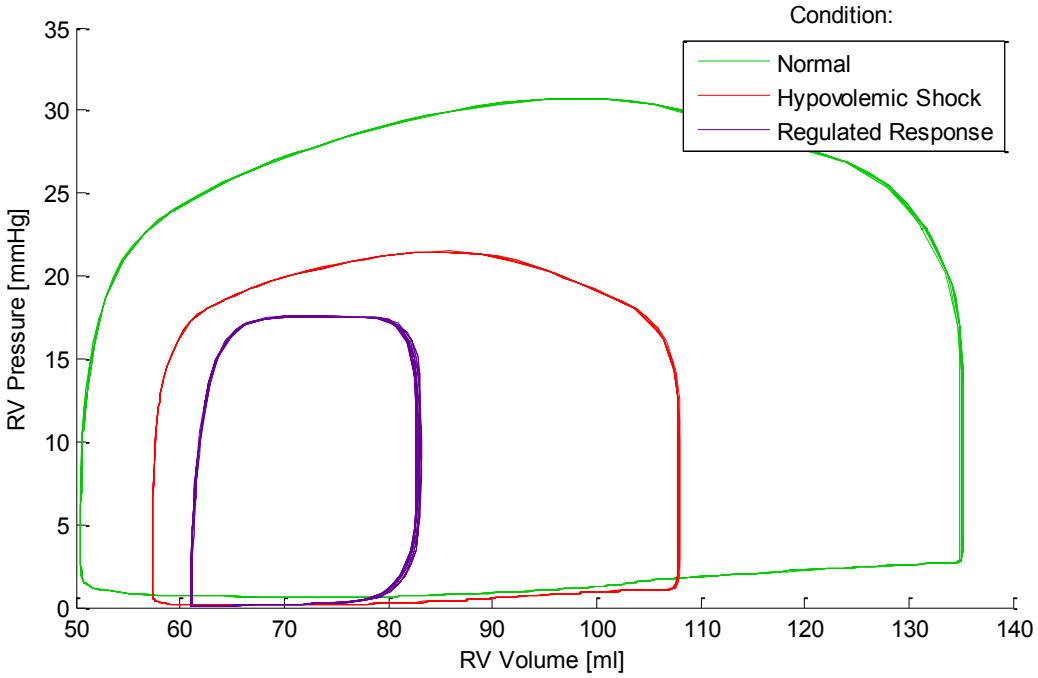

Chart 32: RV p-V Diagram (Hypovolemia with Body Response)

Changes in the sarcomere length of the left wall (Chart 33) are minimal due to shorter contractions.

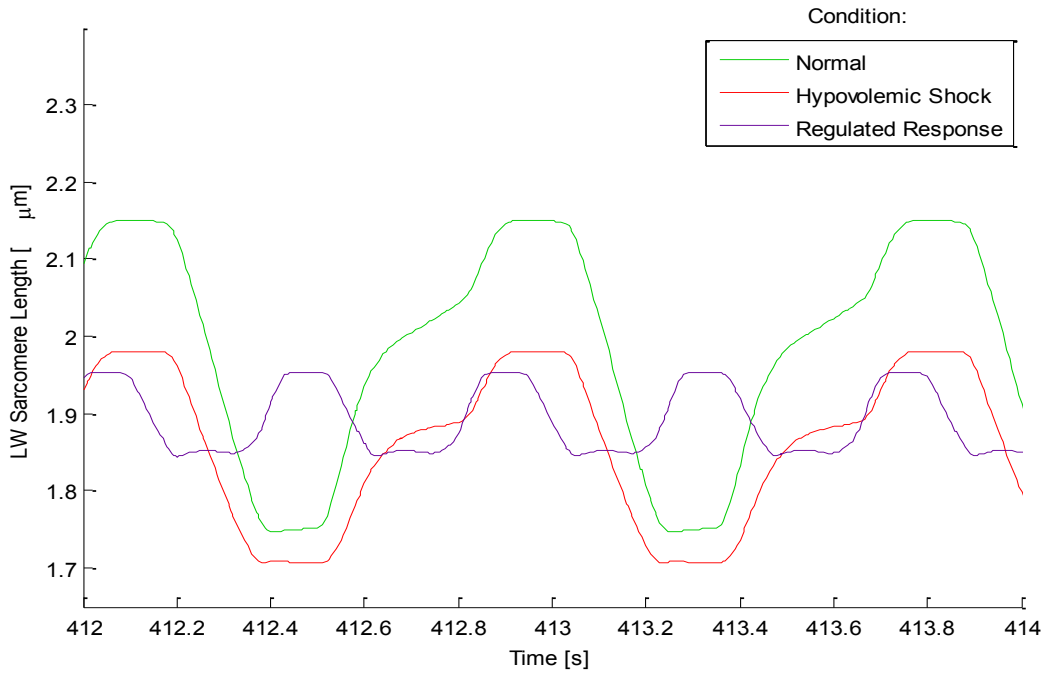

Chart 33: LW Sarcomere Length (Hypovolemia with Body Response)

Flow through systemic capillaries (Chart 34) is very reduced.

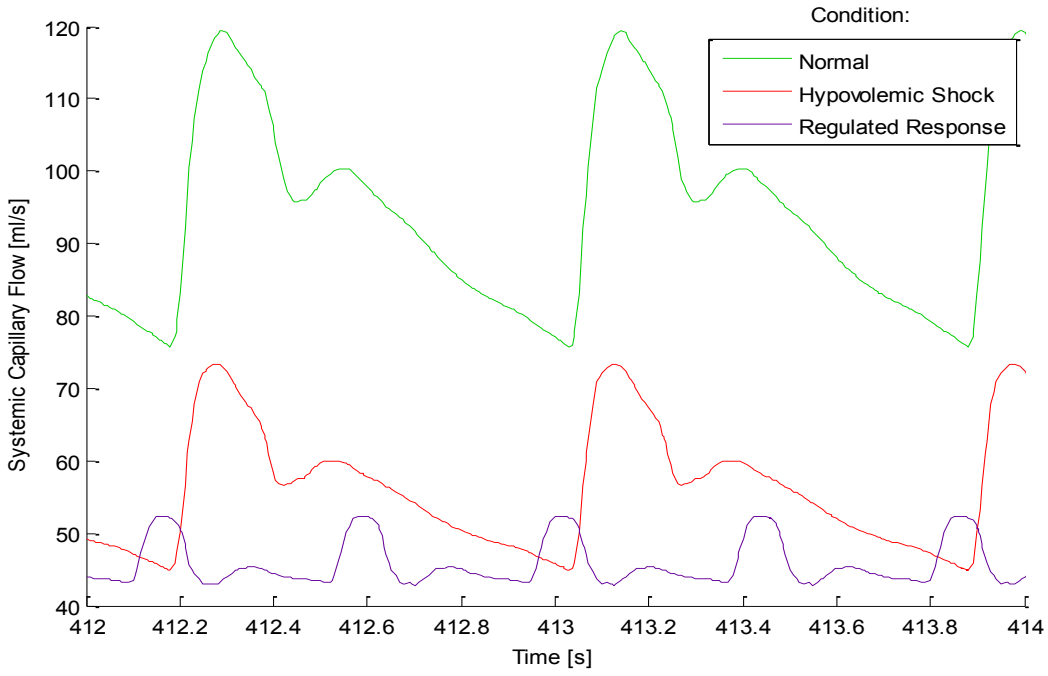

Chart 34: Capillary Flow (Hypovolemia with Body Response)

Flow through brachiocephalic artery (Chart 35) remains relatively unchanged.

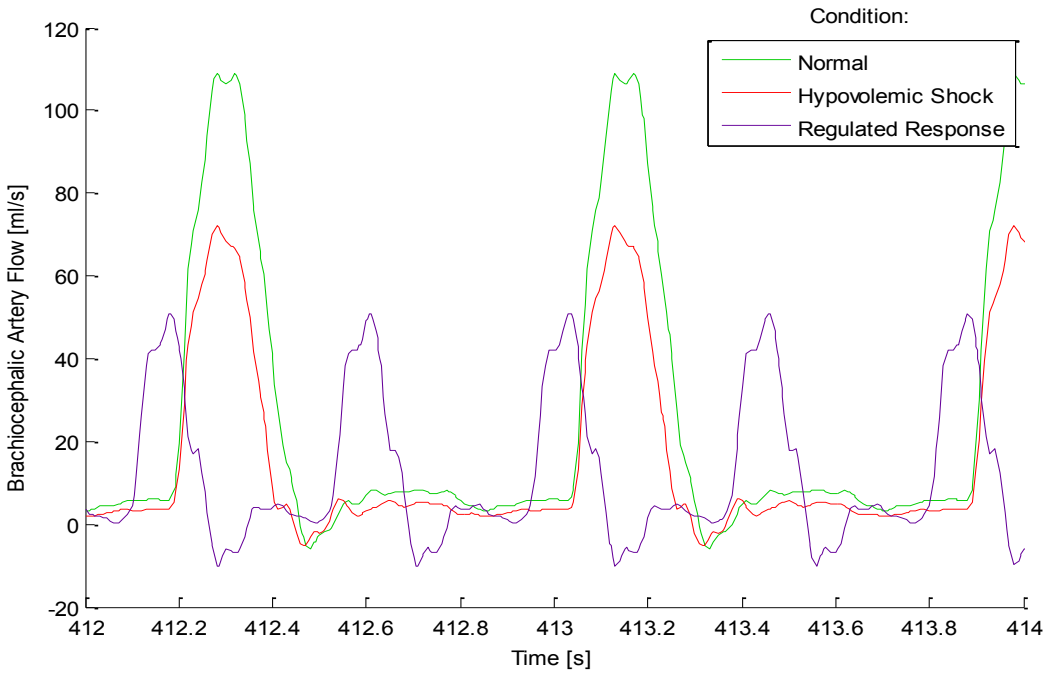

Chart 35: Brachiocephalic Artery Flow (Hypovolemia with Body Response)

However, coronary blood flow (Chart 36) returns to the initial value (approximately).

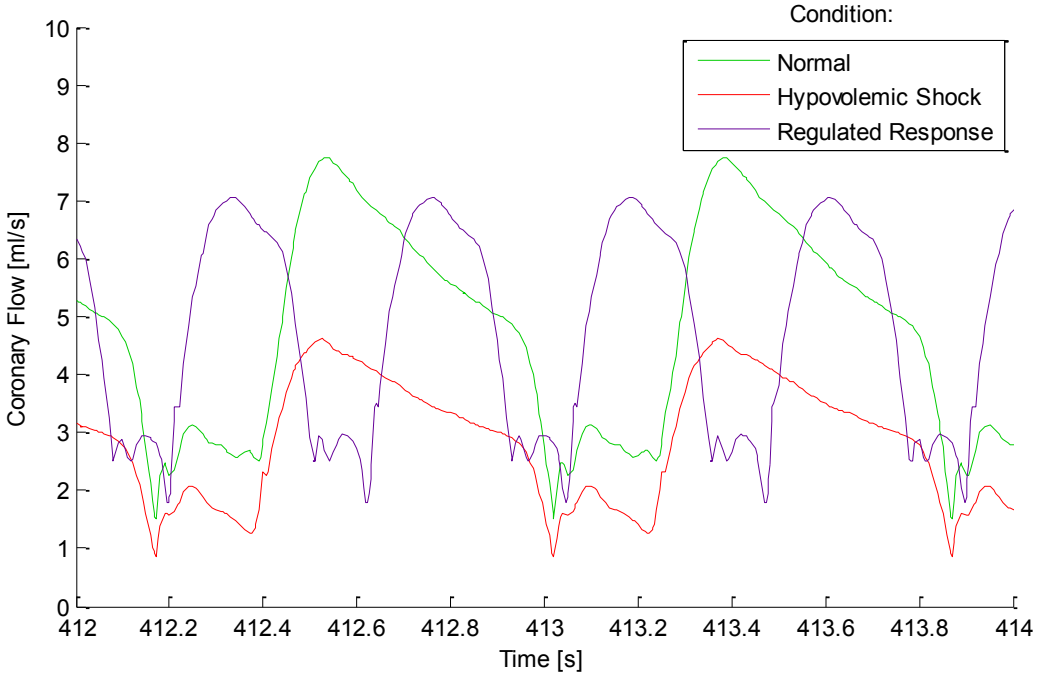

Chart 36: Coronary Flow (Hypovolemia with Body Response)

Stroke work is further decreased but cardiac power output has raised due to the higher heart rate (Chart 37).

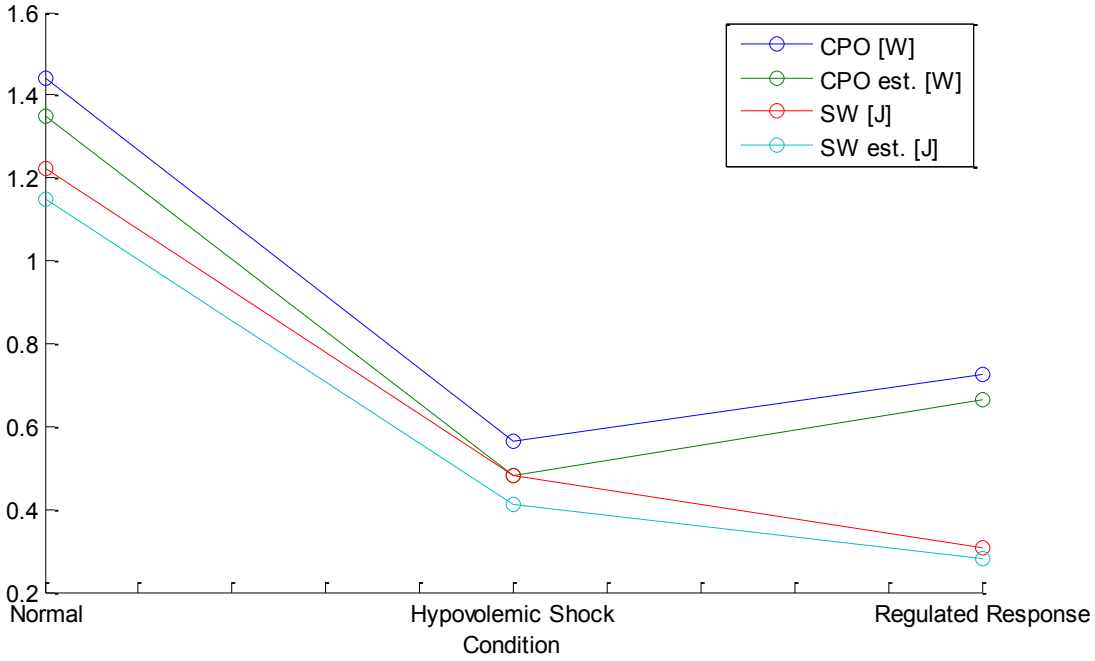

Chart 37: Cardiac Power Output and Stroke Work (Hypovolemia with Body Response)

3.3.3) Left Heart Disease

For this scenario, the left ventricular wall contractility was reduced by 10% steps down to 30 %, diminishing the ability of left ventricle to actively contract.

The aortic pressure (Chart 38) is decreasing with non-equidistant drops.

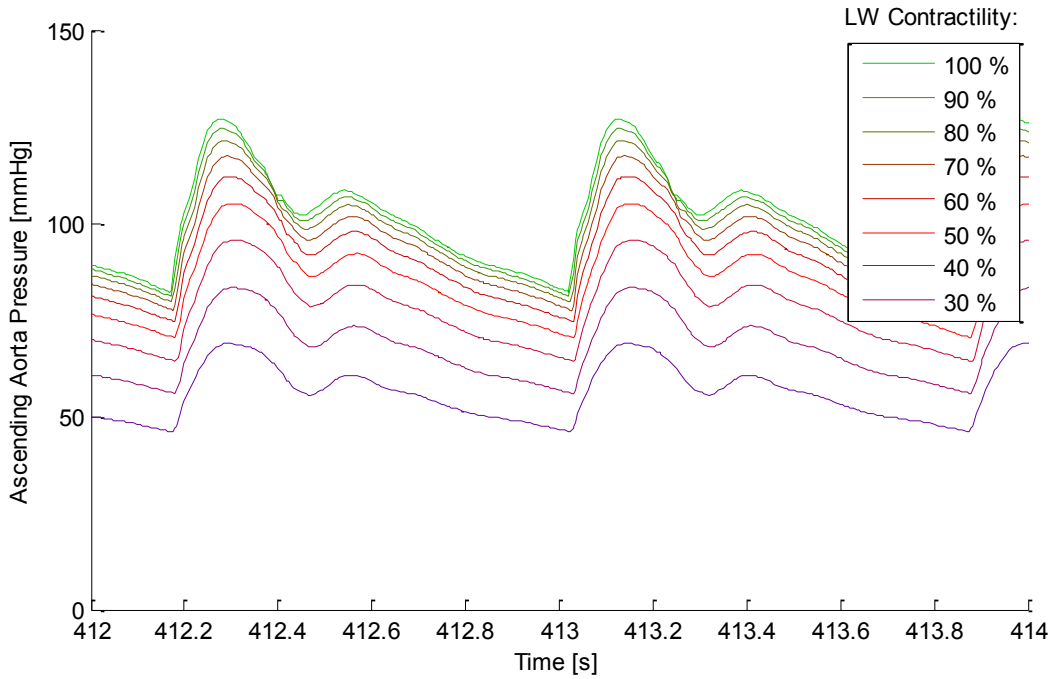

Chart 38: Aortic Pressure (Left Heart Disease)

Left ventricle exerts less pressure and is unable to pump all of its volume out, and consequently, a large volume of blood remains inside (Chart 39).

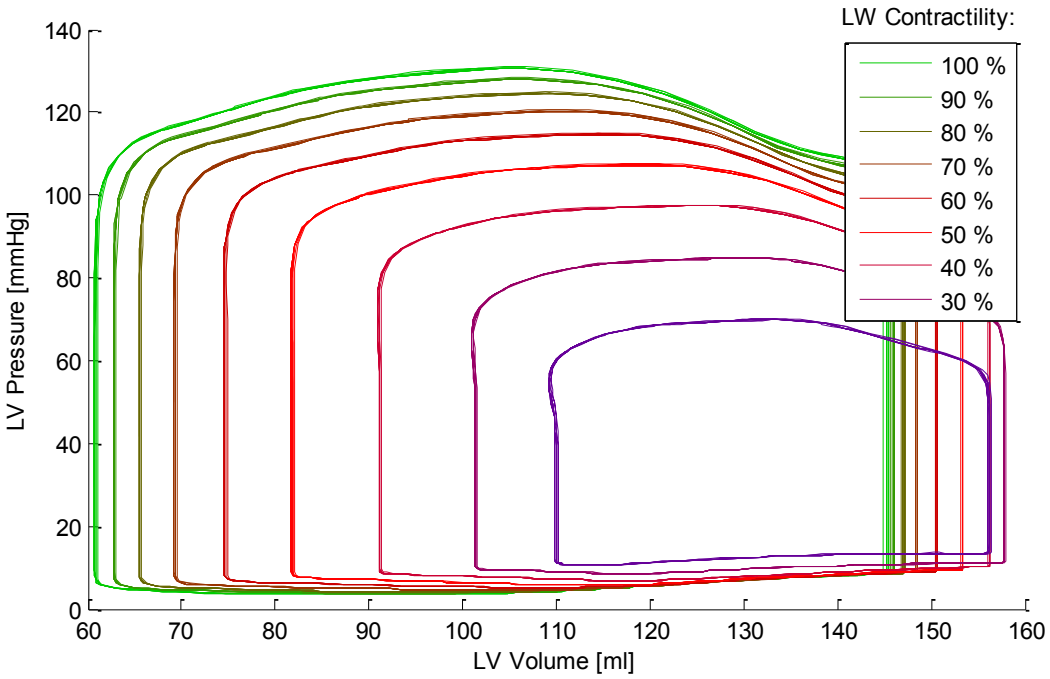

Chart 39: LV p-V Diagram (Left Heart Disease)

Unlike the previous case with hypovolemia, pressure in pulmonary veins (Chart 40) is increasing, as it cannot easily output to the left heart.

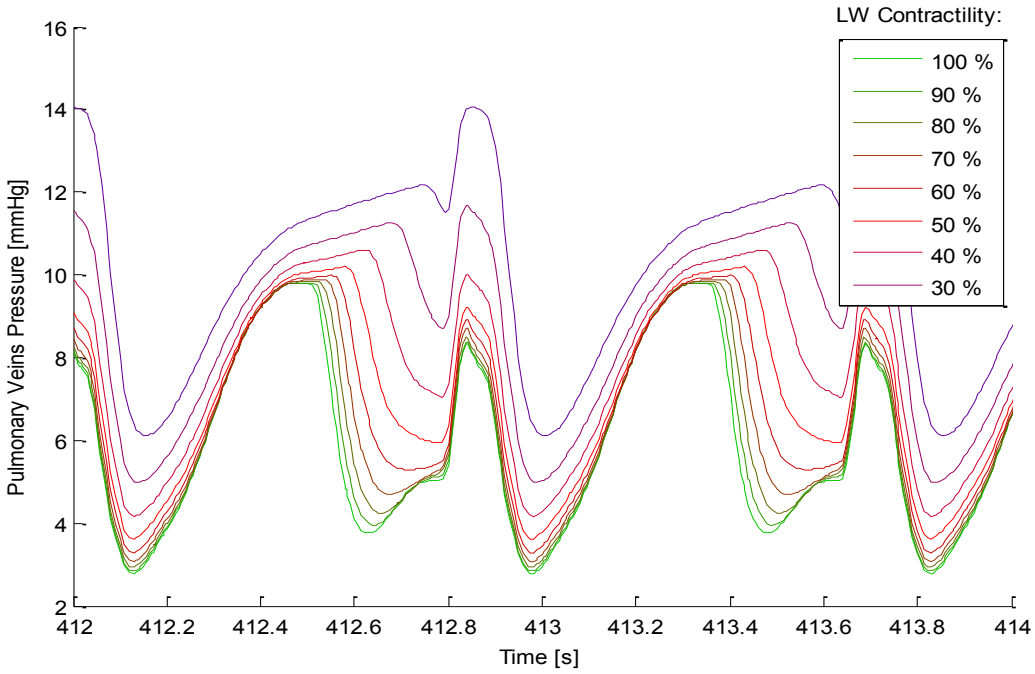

Chart 40: Pulmonary Veins Pressure (Left Heart Disease)

Right ventricle is less filled during diastole (Chart 41) and is also less contracted.

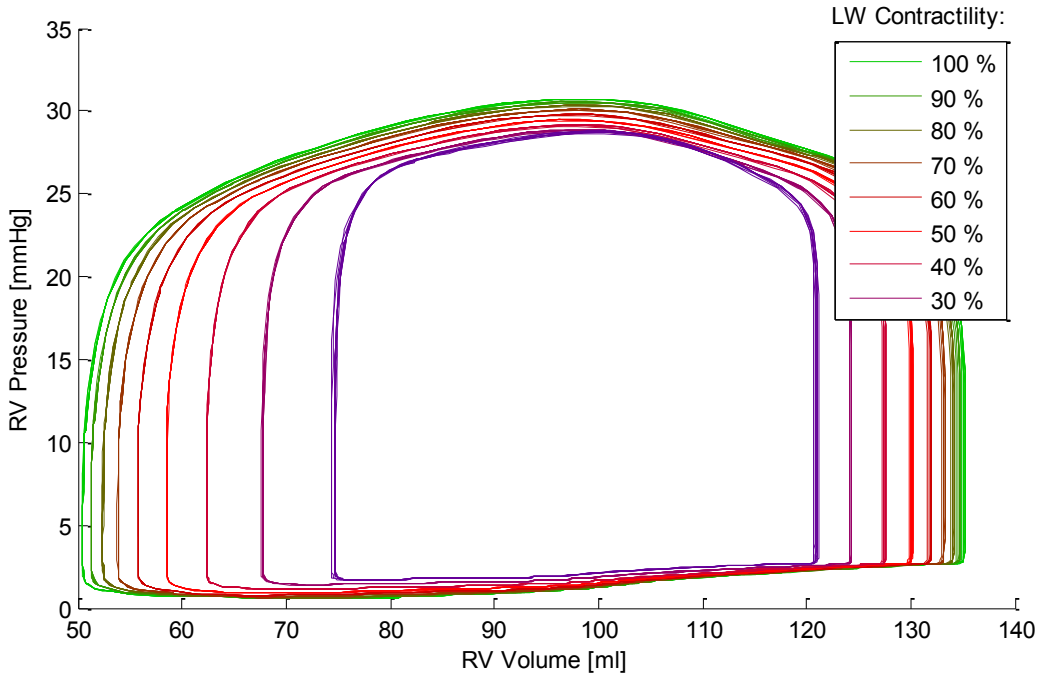

Chart 41: RV p-V Diagram (Left Heart Disease)

Sarcomeres in the left wall (Chart 42) are elongated, which is related to its large filling volume.

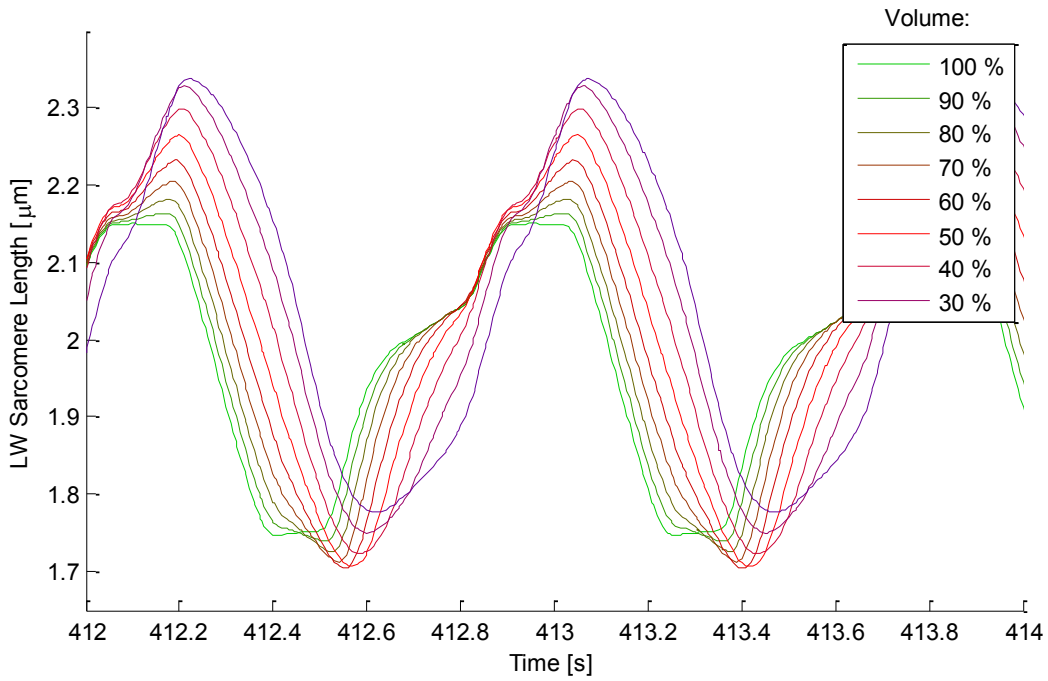

Chart 42: LW Sarcomere Length (Left Heart Disease)

Cardiac power output and stroke work (Chart 43) are decreasing – at a low rate first and then significantly.

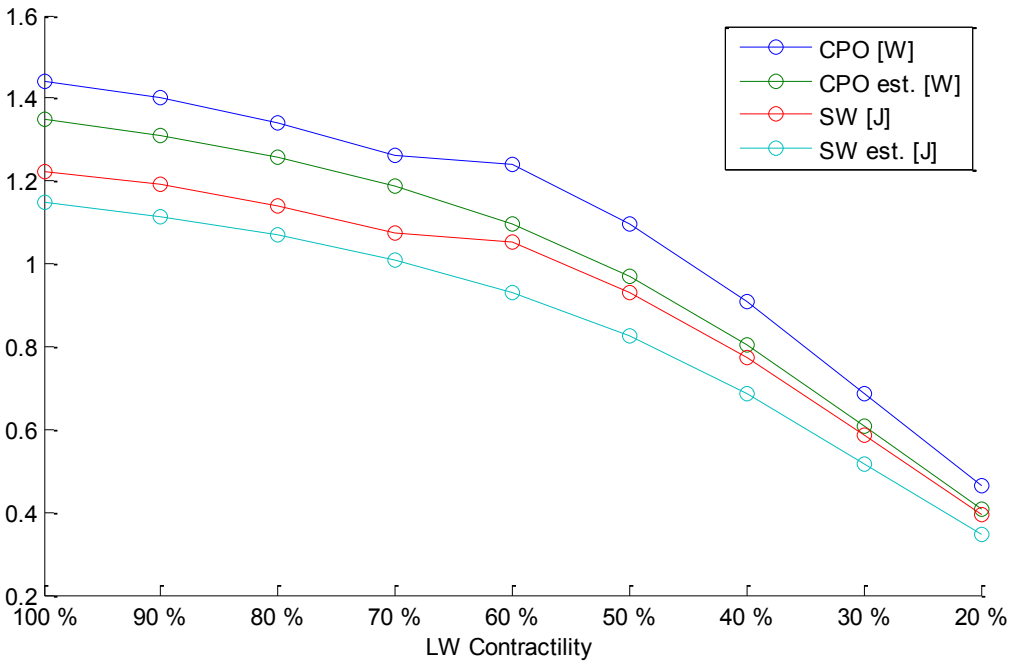

Chart 43: Cardiac Power Output and Stroke Work (Left Heart Disease)

Plotting cardiac output against preload (Chart 44) leads – in this scenario – to a decreasing dependency. This curve is known as a venous return curve – the weakened ventricle retains blood, pressure in left atrium is higher, and as a result, venous return drops. Note that the circuit is closed and stabilized; therefore, venous return and cardiac output are equal.

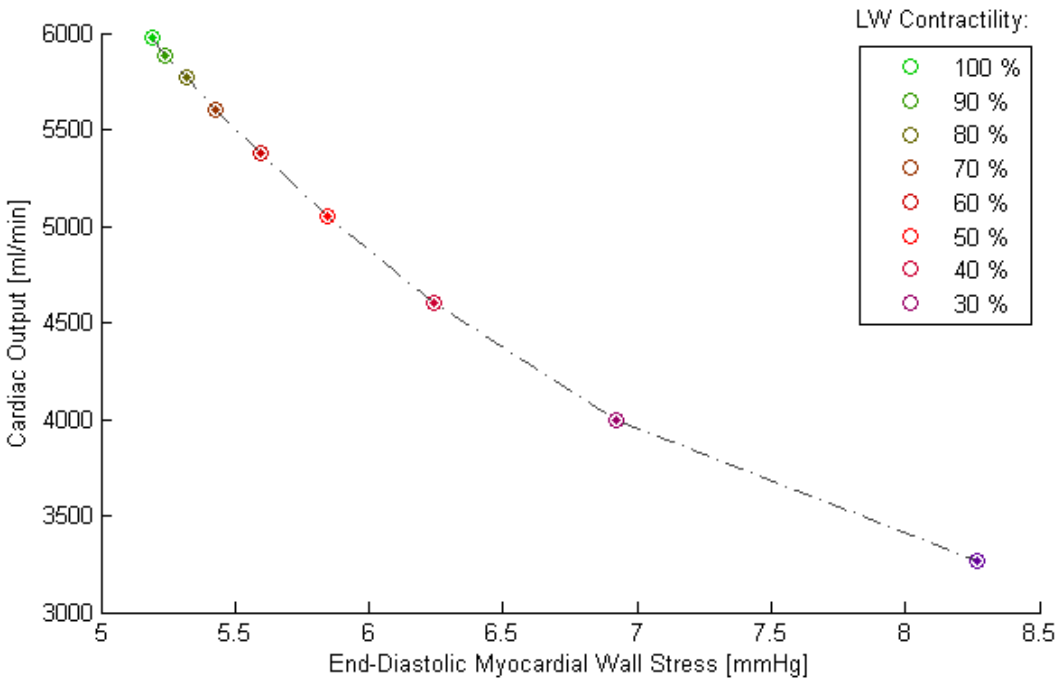

Chart 44: Preload and Cardiac Output Dependency (Left Heart Disease)

3.3.4) Right Heart Disease

This case is similar to the previous scenario, only the right wall is now weakened whereas the left wall remains healthy.

Blood is being retained in the right ventricle (Chart 45).

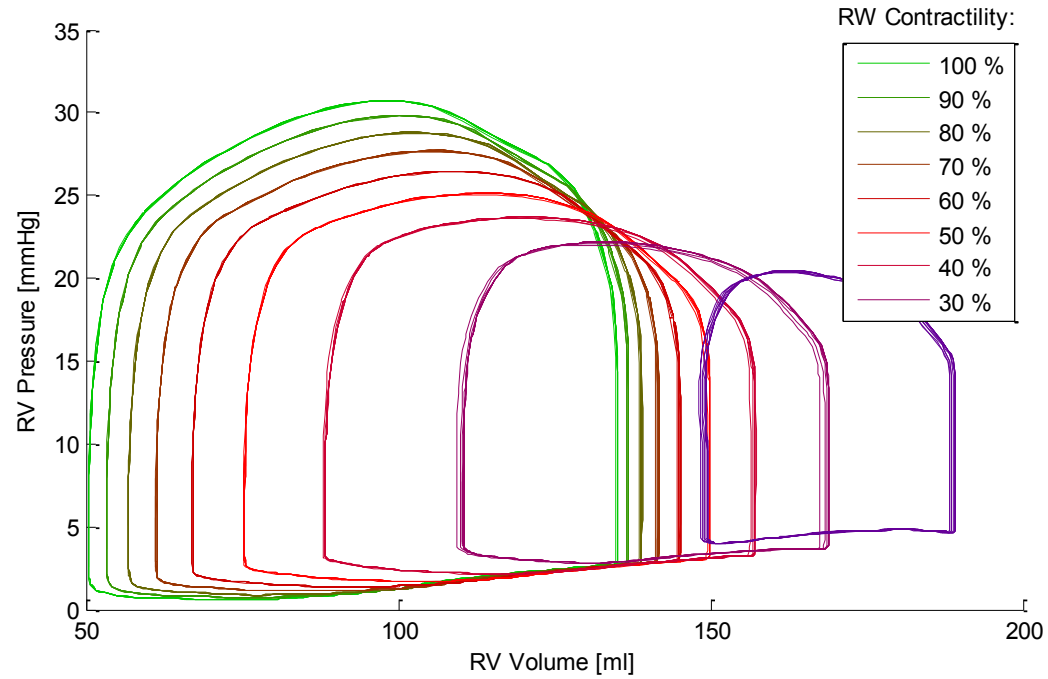

Chart 45: RV p-V Diagram (Right Heart Disease)

On the other hand, the left ventricle diastolic filling is significantly reduced (Chart 46).

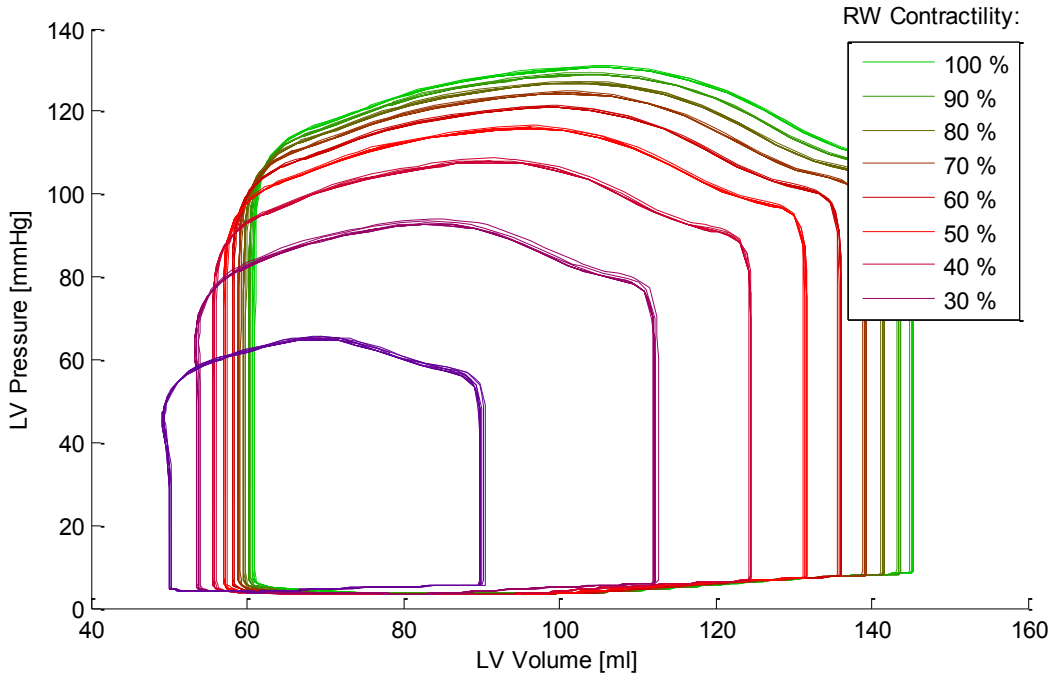

Chart 46: LV p-V Diagram (Right Heart Disease)

The venous return curve (Chart 47) is also clearly visible – now plotted cardiac output in relation to end-diastolic volume of the right atrium (EDV-RA) (using end-diastolic volume is a valid substitution for the "proper" preload (intramyocardial wall stress), since they are correlated).

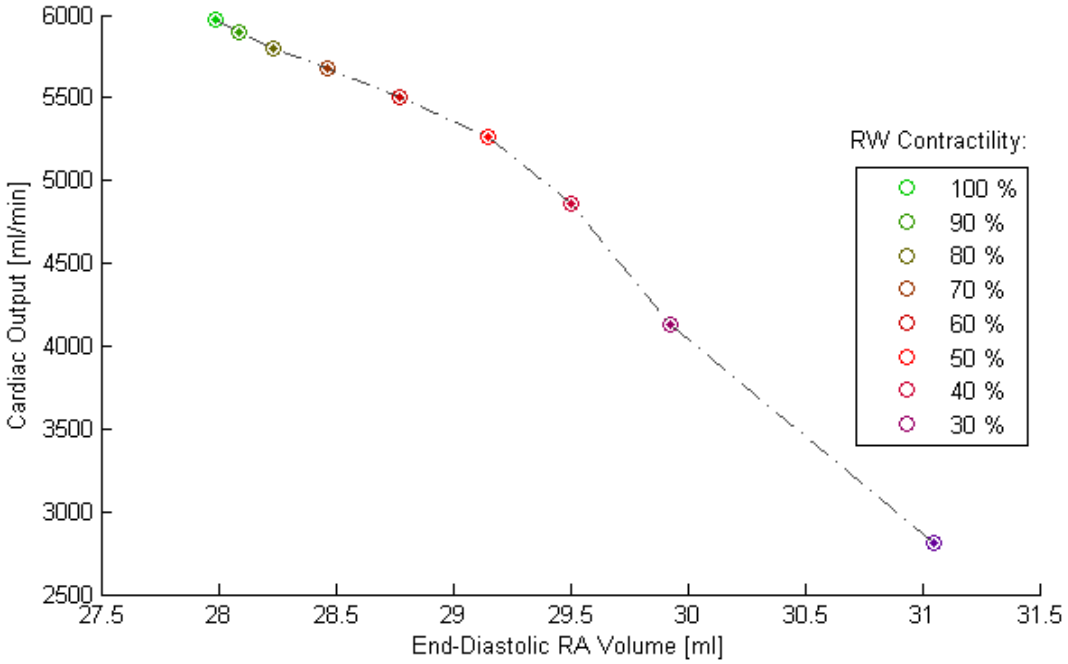

Chart 47: Cardiac Output and EDV-RA Dependency (Right Heart Disease)

3.3.5) Combining Hypovolemia and Left Heart Disease

Plotting working equilibria of 30 states with both reduced blood volume and left heart wall contractility (with the sepal wall still intact), venous return curves for different blood volumes are obtained (Chart 48). The curves are moved towards the point of origin (lower cardiac output and lower preload) in approximately equidistant shifts.

Alternatively, cardiac function curves may be illustrated for various contractility levels (Chart 49). The curves are shifted while their slope declines.

3.3.6) Summary

A drop in the blood volume leads to lower ventricle filling during diastole, lower stretching of sarcomeres, which is in turn connected with a lower sarcomere contraction and lower stroke volume and cardiac output. This is in accordance with the Frank-Starling law.

When considering a body response, the vital functions (coronary blood flow, arterial pressure) were significantly improved although the flow through capillaries is further reduced. This seems very real.

Simulations of a ventricular malfunction result in retaining a higher blood volume in the affected ventricle, followed by local hypertension.

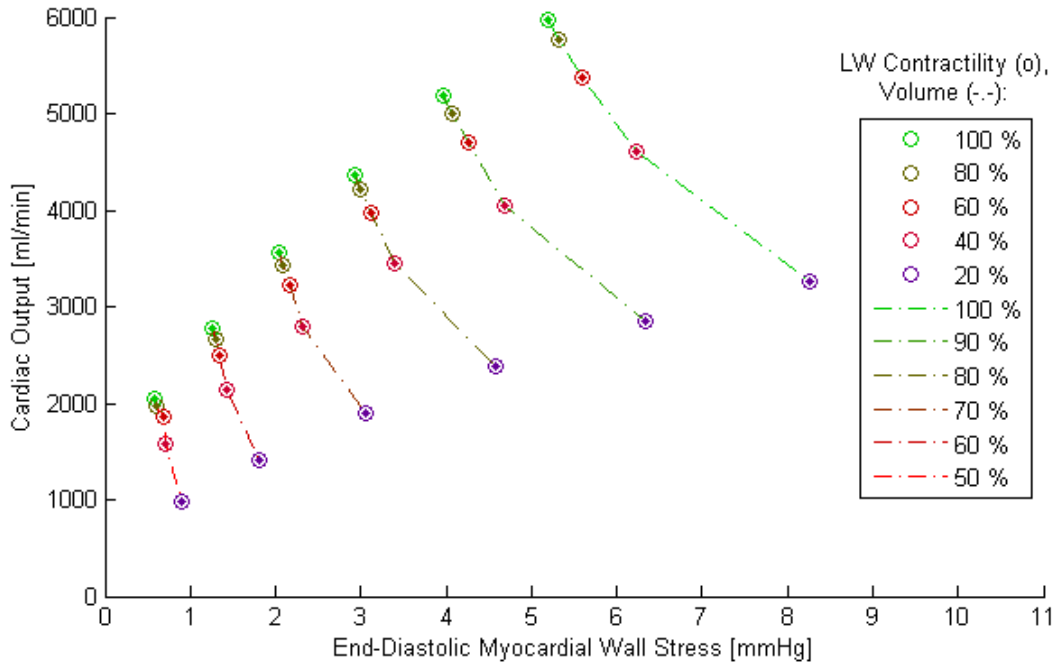

Chart 48: Emergence of Venous Return Curves (Hypovolemia and Contractility)

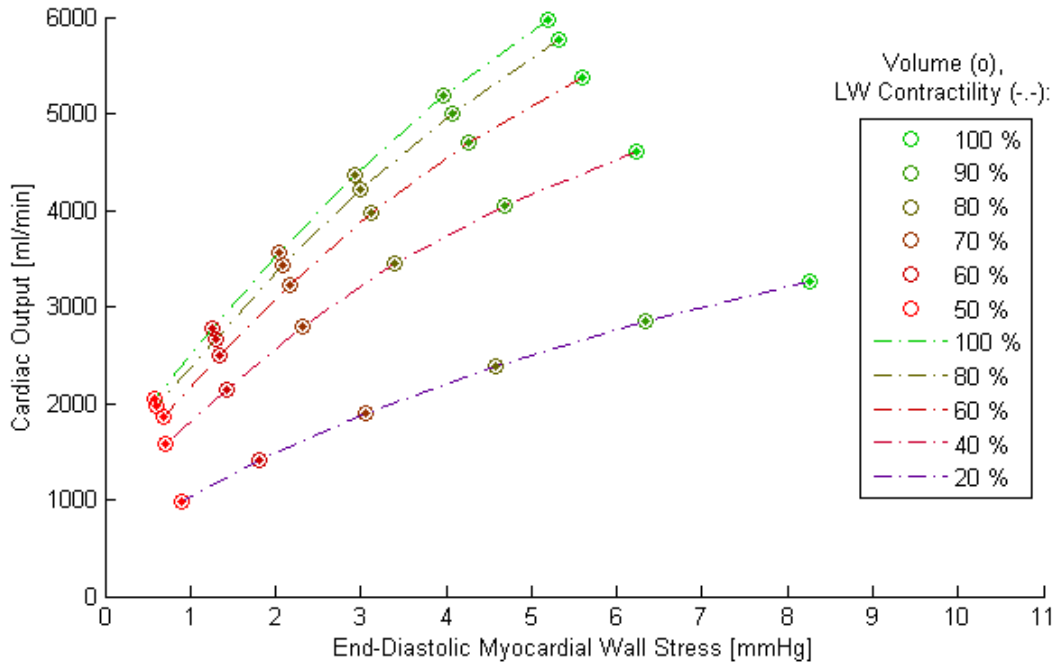

Chart 49: Emergence of Cardiac Function Curves (Hypovolemia and Contractility)

Cardiac function and venous return curves are very close to encyclopedic drawings (Figure 12). Decrease in blood volume and contractility (inotropic effect) were simulated only. Therefore, the upper parts of the curves are not visible. Note that the curves are extrapolated only via working equilibria, which means that adjusting blood volume can reveal the cardiac function curve while changes to contractility disclose the venous return curve. However, the cardiac function curve points

to the origin, leading to difficulties in finding a working equilibrium for the upper parts of the venous return curve.

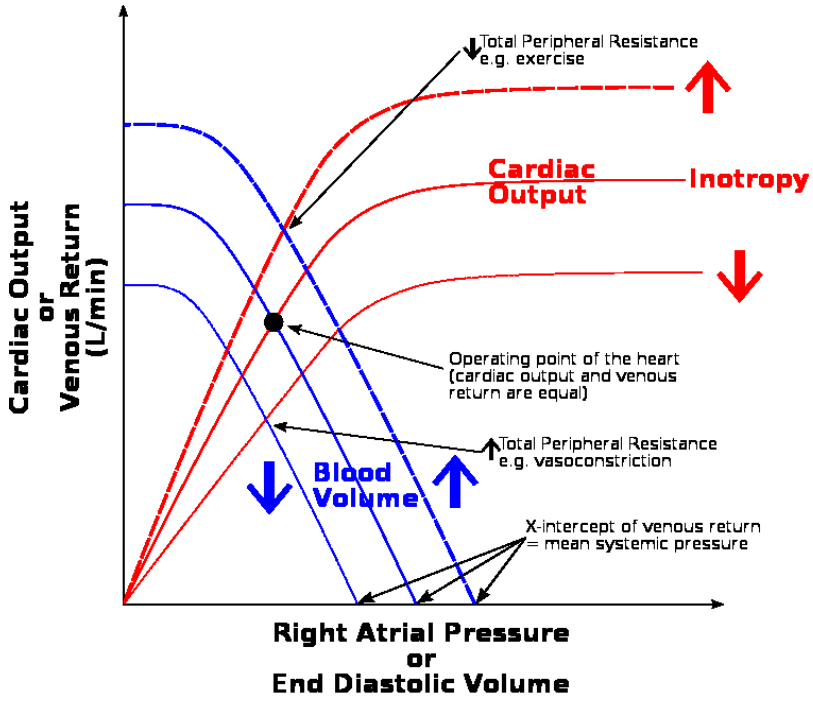

Figure 12: Cardiac Function and Venous Return Curves

Source: Wikimedia Foundation (2010)

3.4) Pathological Conditions II: Arterial Tree Pathologies

In these simulations, effects of increased stiffness of systemic arteries and stenosis in aortic arch were examined.

3.4.1) Arterial Stiffness

For this scenario, stiffness (the inverse of compliance) was gradually raising up to 300 % by 50% increments for each arterial segment.

Aortic pressure (Chart 50) is elevated as a result of earlier reflections within the tree, which is losing its flexibility.

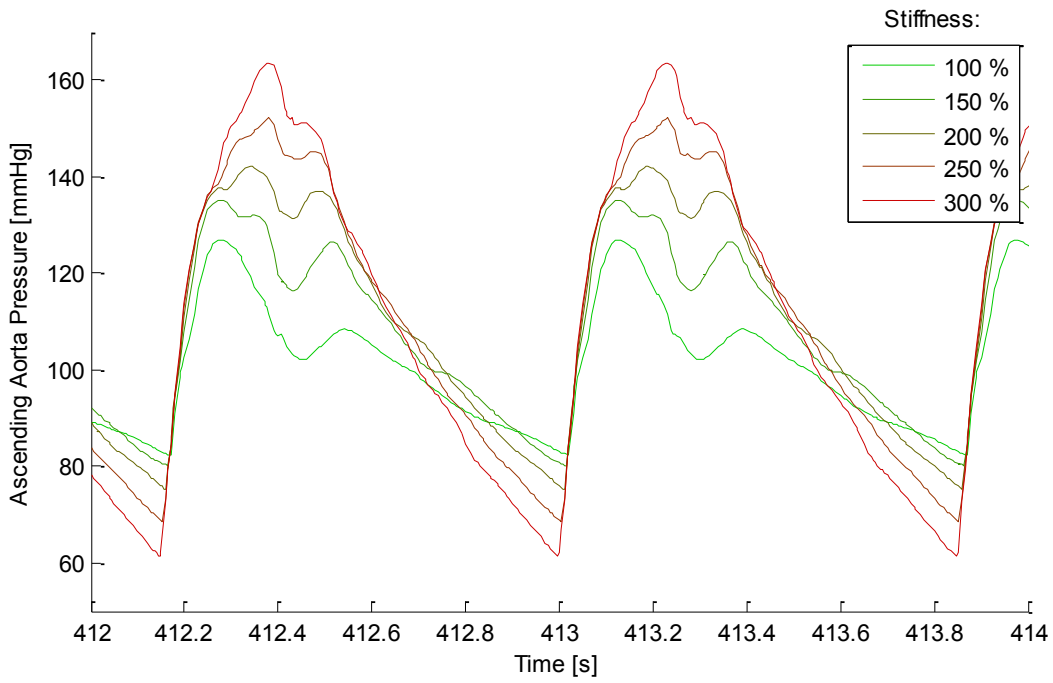

Chart 50: Aortic Pressure (Stiffness)

Left ventricle is retaining more blood (Chart 51).

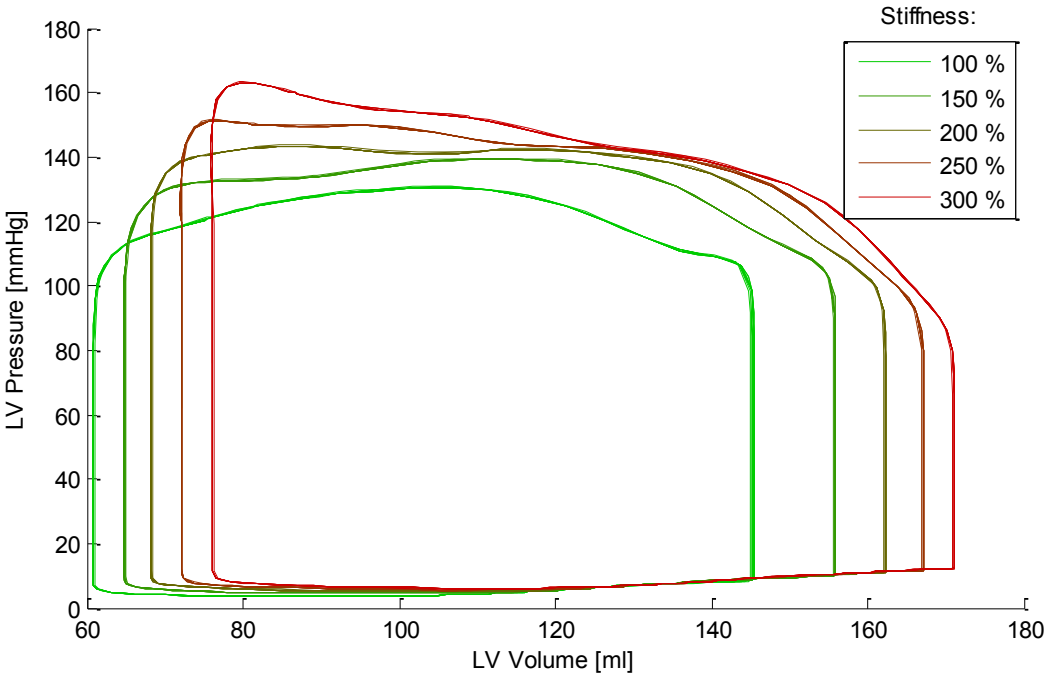

Chart 51: LV p-V Diagram (Stiffness)

The situation in the right ventricle (Chart 52) remains almost unchanged.

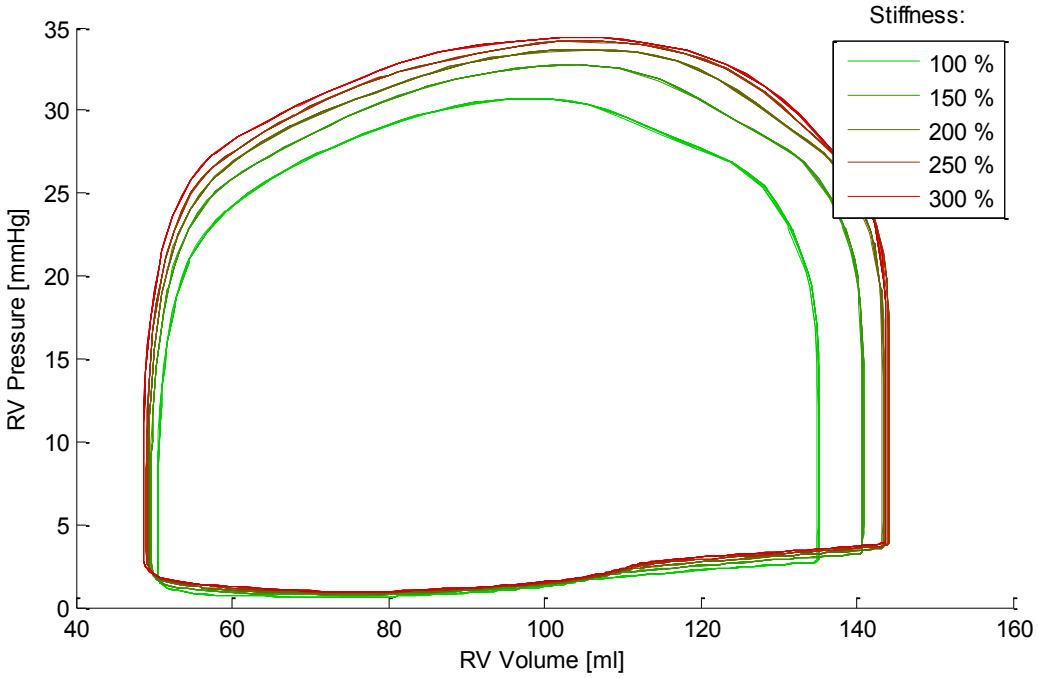

Chart 52: RV p-V Diagram (Stiffness)

Length of sarcomeres in the left wall (Chart 53) is a little higher, which corresponds to the higher volumes throughout the cardiac cycle.

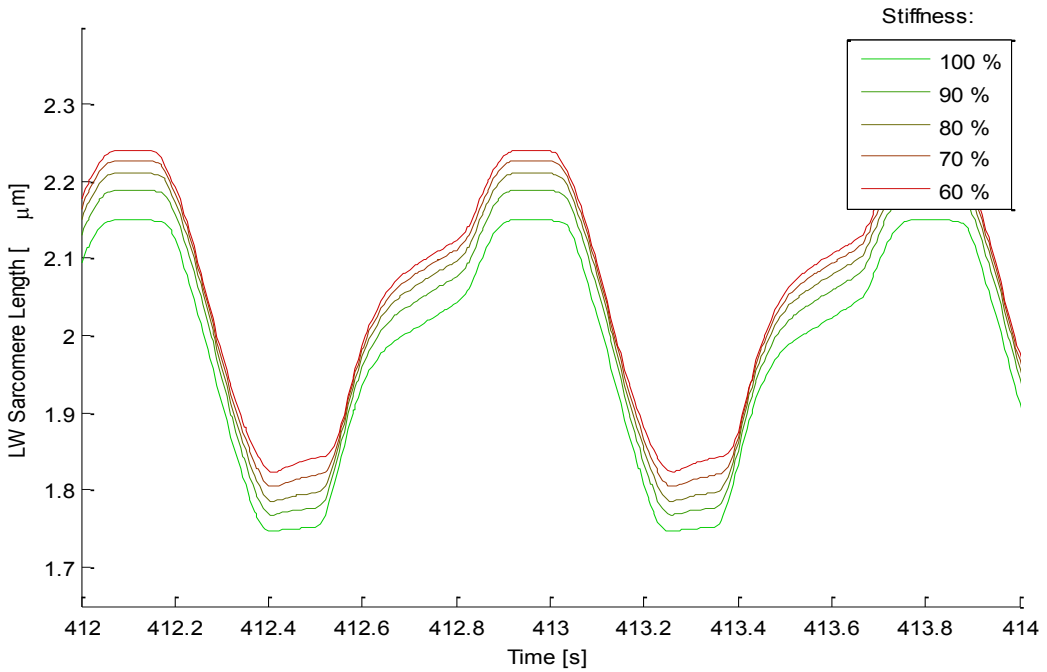

Chart 53: LW Sarcomere Length (Stiffness)

Cardiac power output and stroke work (Chart 54) significantly increase. The heart exerts more energy to overcome the higher preload.

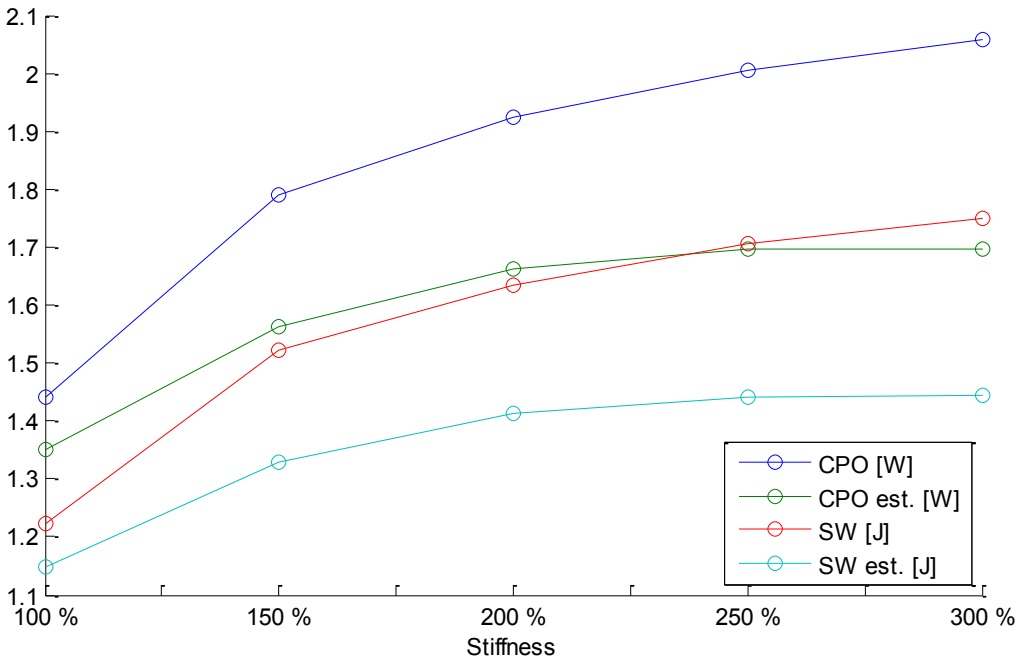

Chart 54: Cardiac Power Output and Stroke Work (Stiffness)

Coronary blood flow (Chart 55) is slightly elevated during systole and at the beginning of diastole. In the second part of diastole, the flow is decreased.

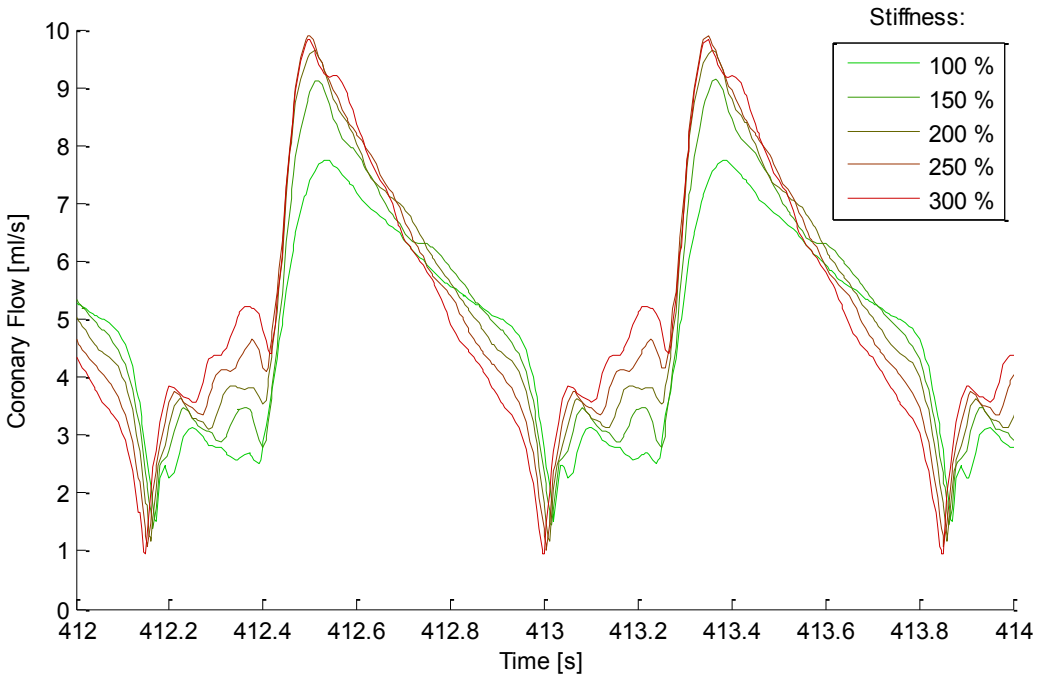

Chart 55: Coronary Flow (Stiffness)

Cardiac output increases together with elevated preload (Chart 56). This line forms the upper part of the cardiac function curve – note the characteristic plateau at the end of the curve.

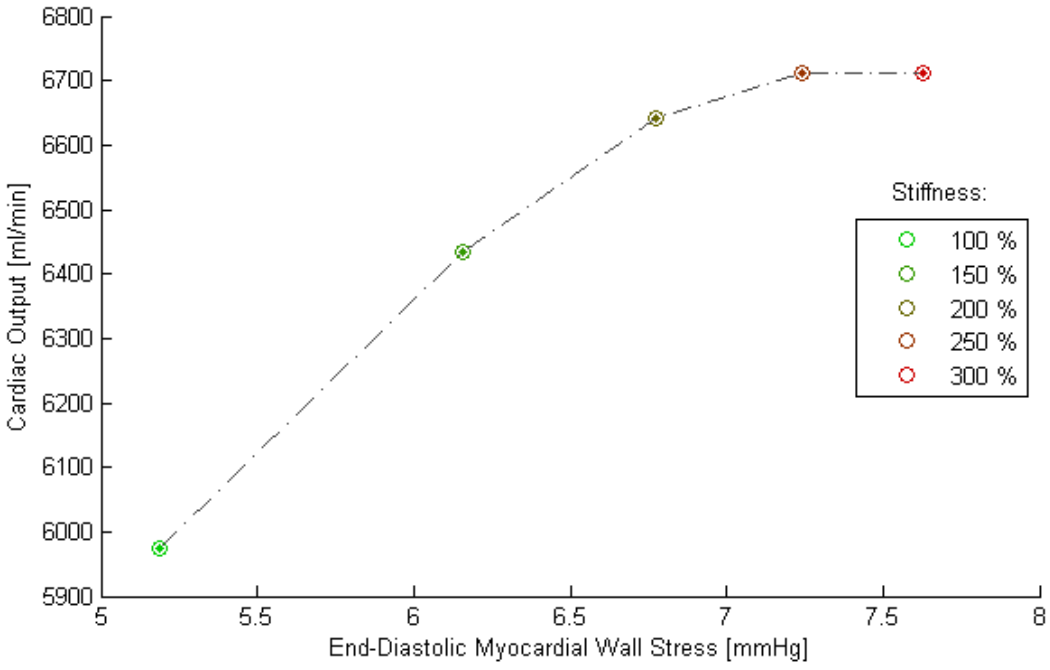

Chart 56: Cardiac Output and Preload Dependency (Stiffness)

3.4.2) Stiffness and Chronic Adaptation

As the high arterial stiffness tends to be a chronic condition, the adaptation protocol was applied despite a danger of instability, since the derived tree is not adaptable (which may negatively affect the integrity of the process of adaptation). The considered case is stiffness scaled to 250 %.

Aortic pressure (Chart 57) remains nearly unchanged. The pressure peak is smoothen, resulting in 5 – 10 mmHg lower systolic pressure.

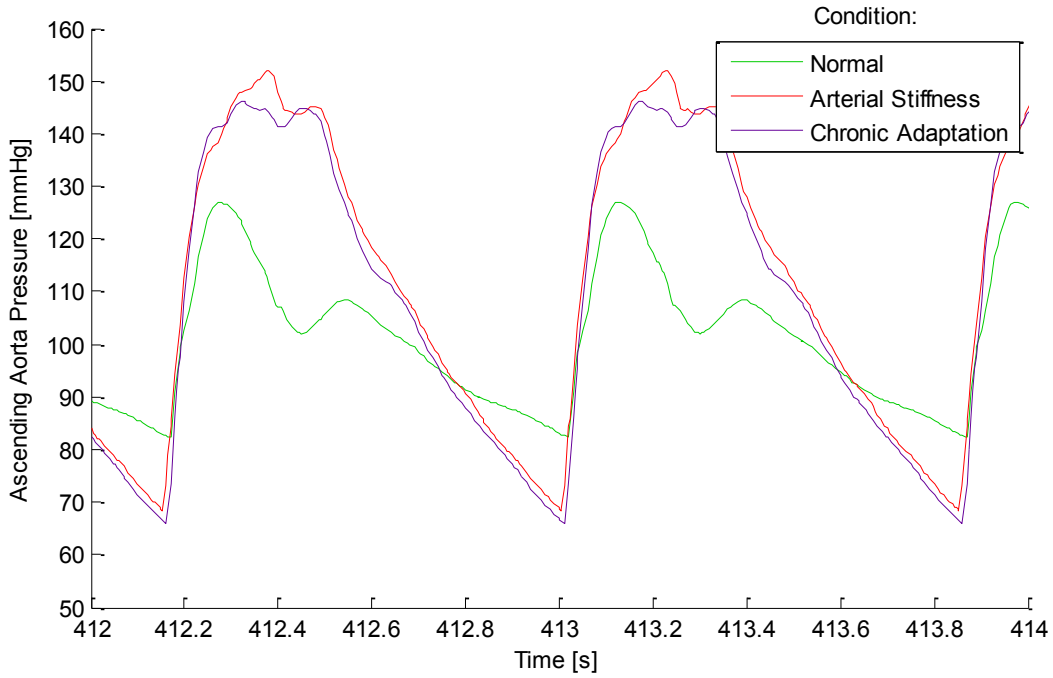

Chart 57: Aortic Pressure (Stiffness and Chronic Adaptation)

Pressure in the left ventricle remains elevated whereas filling volume has returned back to normal (Chart 58).

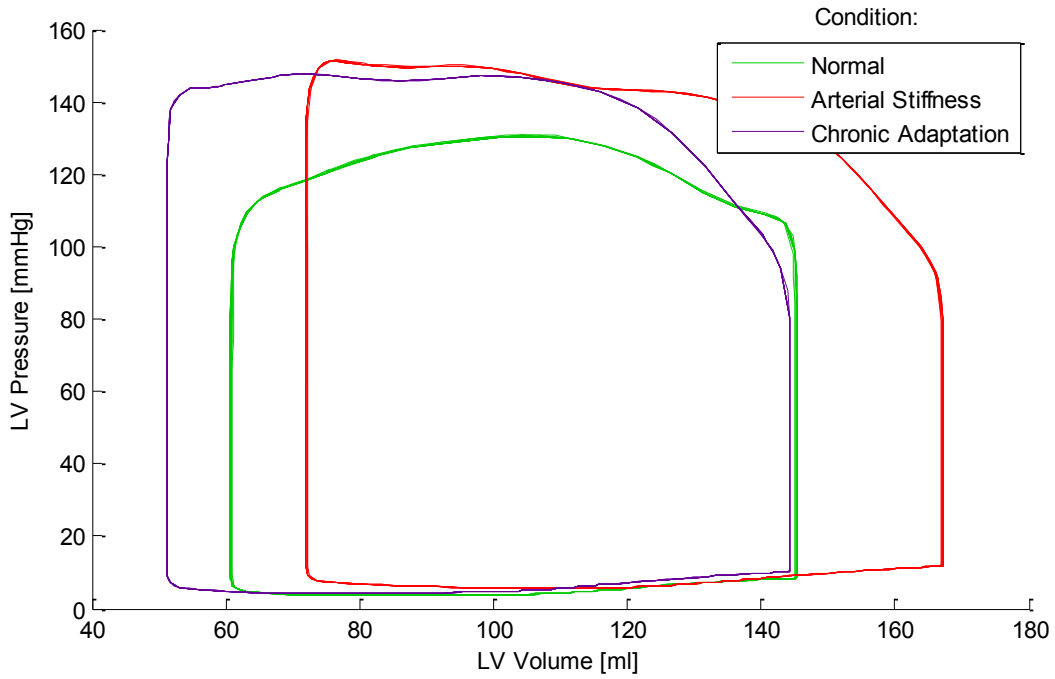

Chart 58: LV p-V Diagram (Stiffness and Chronic Adaptation)

Cardiac power output and stroke work (Chart 59) are decreased only little and remain elevated.

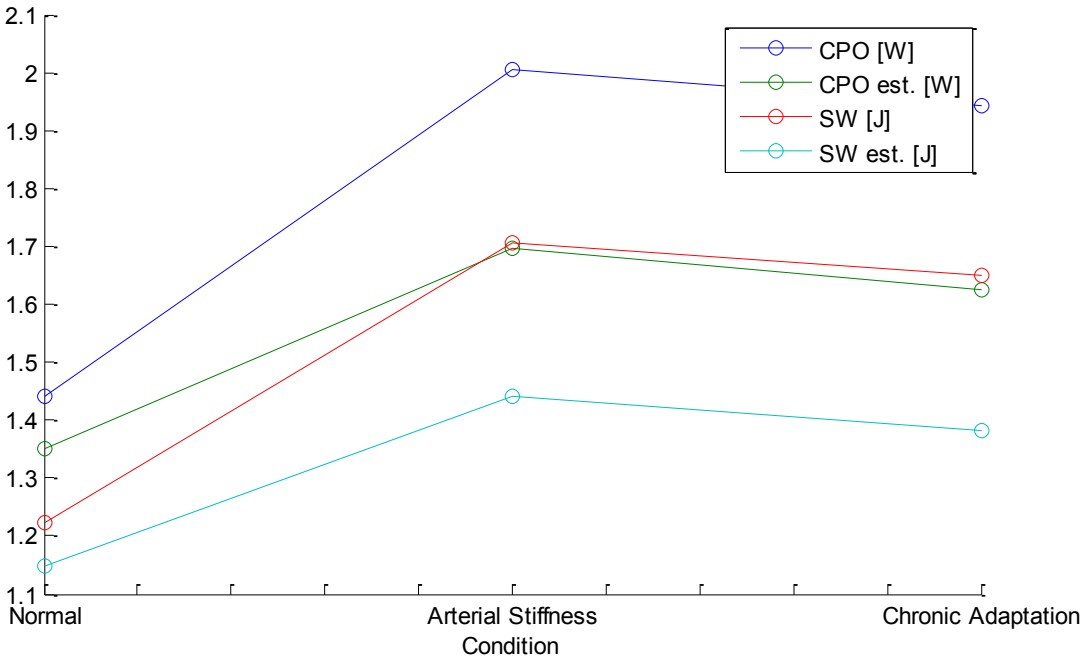

Chart 59: Cardiac Power Output and Stroke Work (Stiffness and Chronic Adaptation)

3.4.3) Aortic Stenosis

A second simulated pathology of the arterial tree is stenosis in aortic arch, ranging from 0 up to 50 % by 10% increments. This portion of radius of both arch segments is changed to the vessel wall.

Aortic pressure patterns (Chart 60) indicate progressive hypertension as in the previous scenario. The wave reflection is, however, not the cause. The reflection is in fact dampened, as it cannot easily transmit through the arch constriction back to ascending aorta. The pressure peak is caused by initial surge into the constriction and slower propagation beyond.

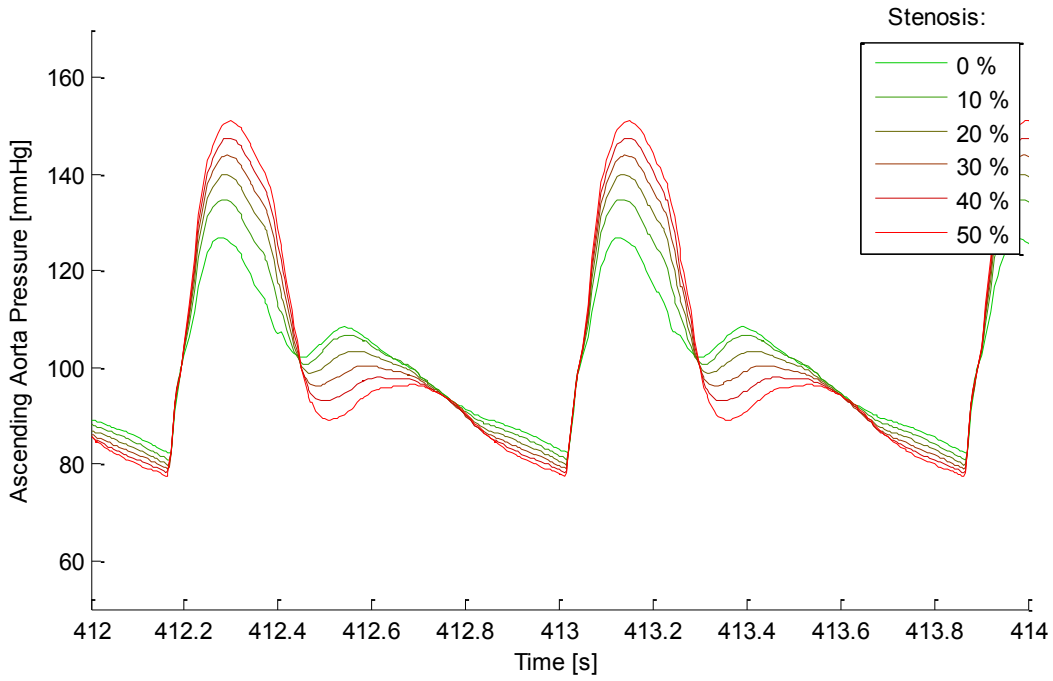

Chart 60: Aortic Pressure (Stenosis)

Left ventricular filling volume (Chart 61) is slightly elevated.

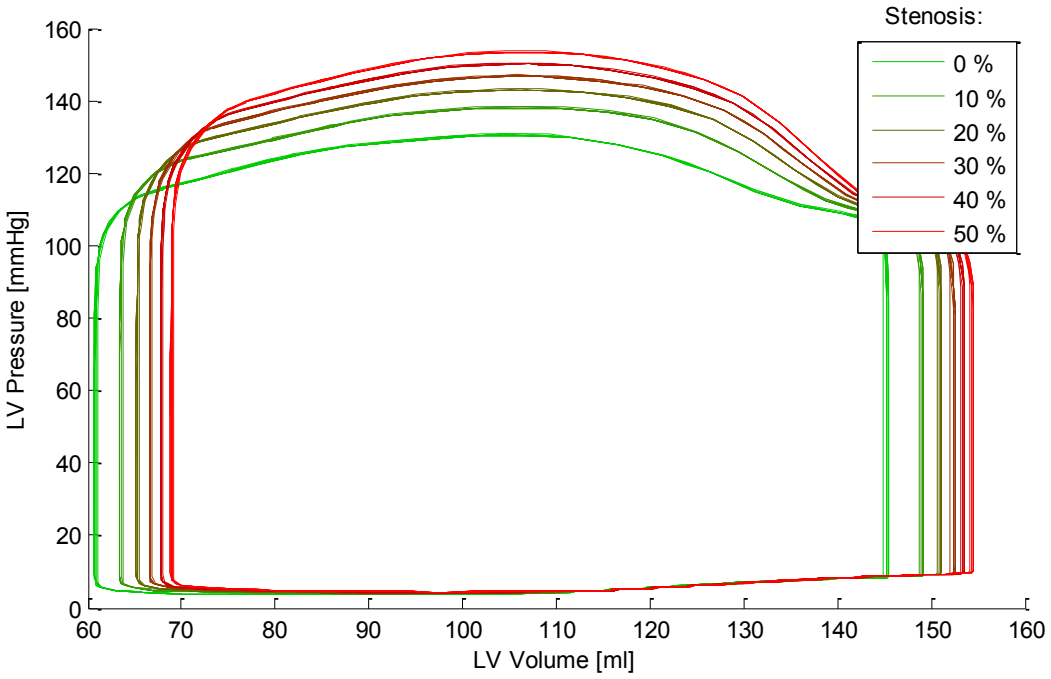

Chart 61: LV p-V Diagram (Stenosis)

Cardiac power output and stroke work (Chart 62) are increased; the heart needs more energy to pump through the stenotic segments. Here, the estimated values based on mean arterial pressure are biased because of only slight variations in mean arterial pressure (which is elevated during systole but reduced during diastole – but the diastolic part is not relevant with respect to cardiac work and power).

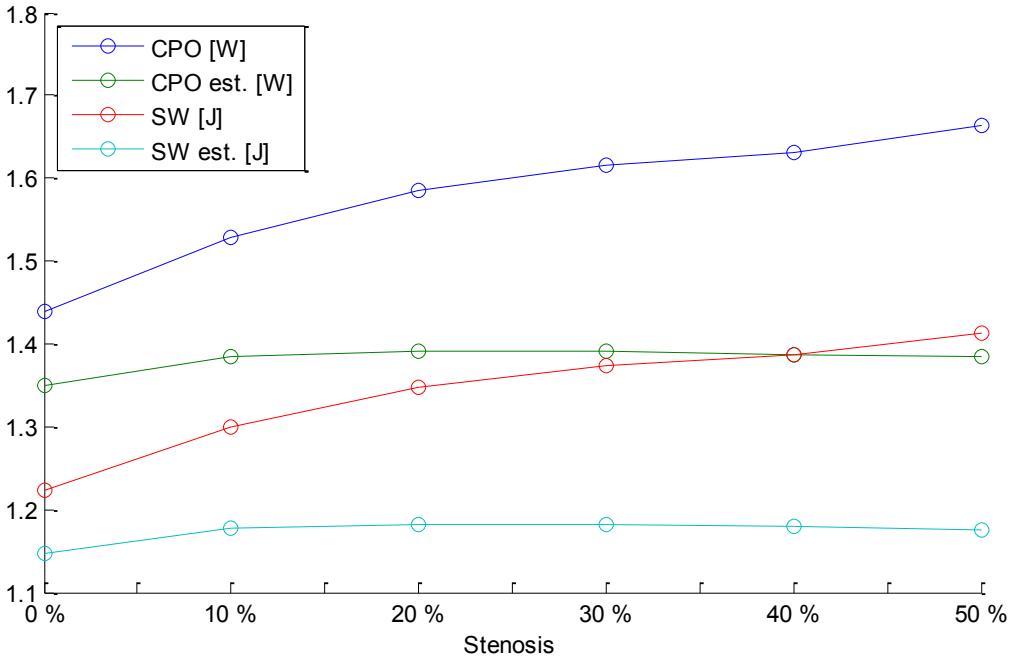

Chart 62: Cardiac Power Output and Stroke Work (Stenosis)

Flow through thoracic aorta (Chart 63) is reduced due to the constriction.

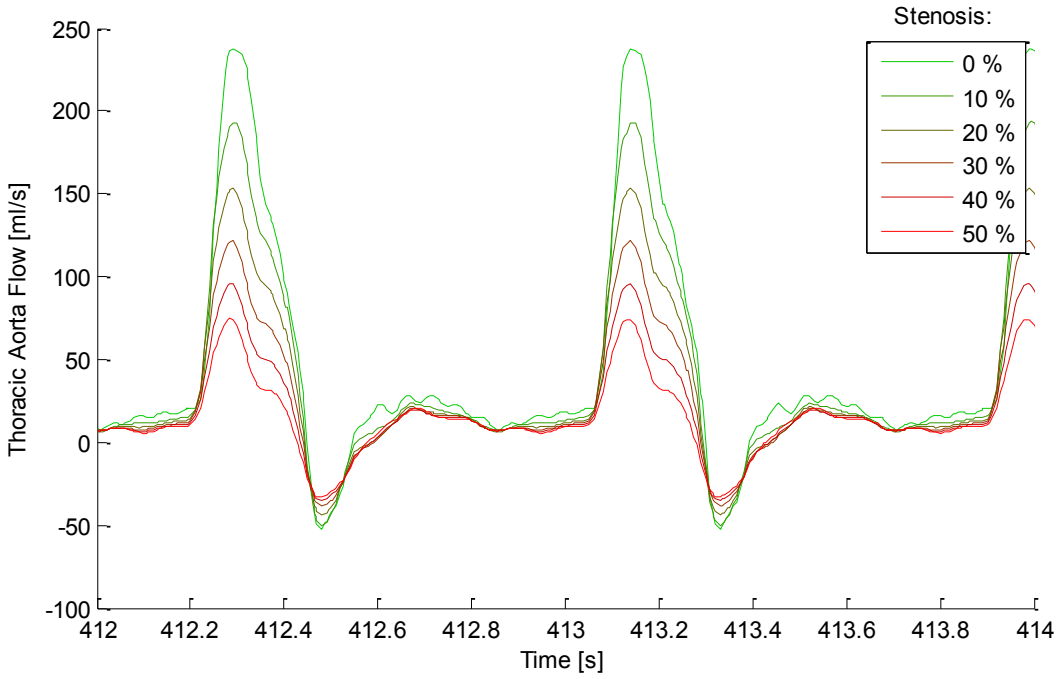

Chart 63: Thoracic Aorta Flow (Stenosis)

On the other hand, blood flow through brachiocephalic artery (Chart 64) is increased, since it is connected into the middle of aortic arch so the blood can easily flow through this artery rather than the second part of the constriction and farther continue through aorta.

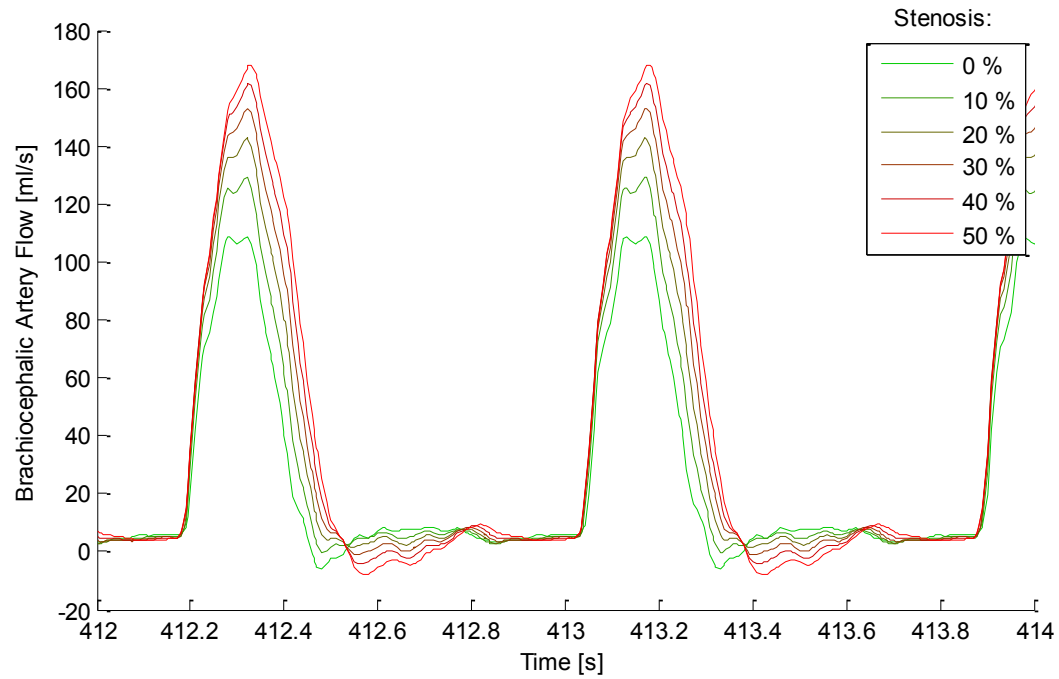

Chart 64: Brachiocephalic Artery Flow (Stenosis)

Coronary flow (Chart 65) is increased during systole only slightly.

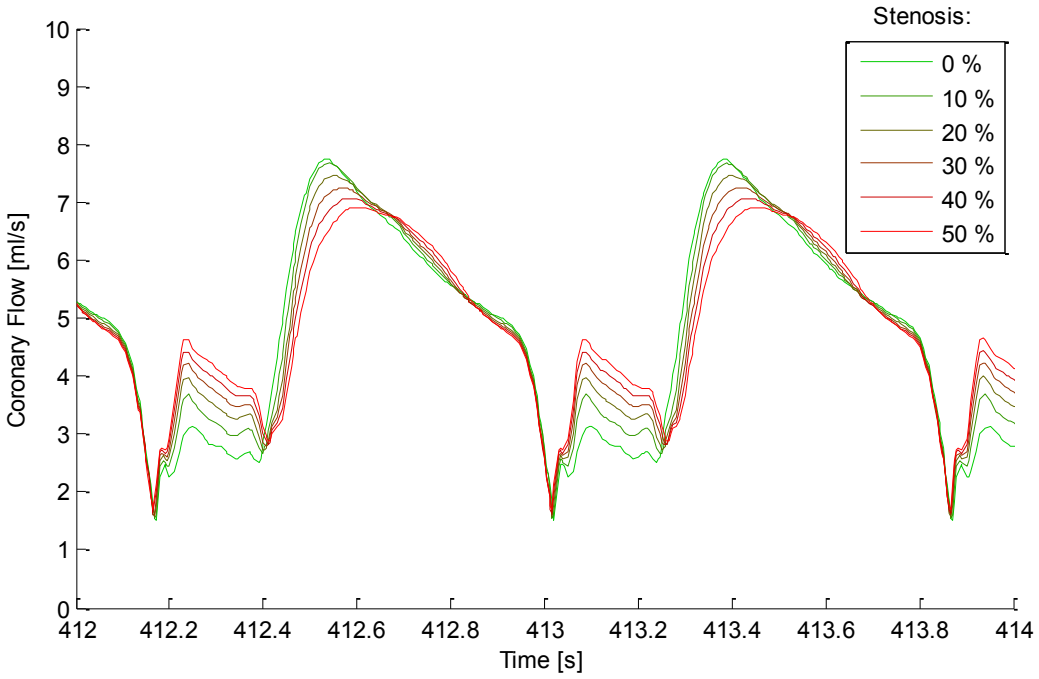

Chart 65: Coronary Flow (Stenosis)

3.4.4) Summary

As expected, the arterial stiffness leads to hypertension and urges the heart to exert more of mechanical work. The most notable changes during the adaptation process include 50% and higher increase in reference wall volume for all heart segments and pulmonary vessels.

Aortic stenosis negatively affects cardiac energy requirements and distribution of blood flow through the body.

3.5) Cardiac Supports I: Effects of IABP Settings

Supposing decreased contractility of the left ventricle wall to the level of 50 %, IABP was applied – similarly as in Schampaert et al. (2013). The support device was examined with respect to balloon contra-pulsation timing.

3.5.1) Inflation Timing

First, start of inflation was synchronized with the location of dicrotic notch (Krishna & Zacharowski, 2009), i.e. setting 570 ms. Thereafter, shifting in the inflation timing was simulated from -200 to +150 ms with 50ms steps.

Aortic pressure waveform (Chart 66) indicates decreased afterload (the systolic peak is lower), compensated by increased pressure during diastole (the second peak) due to contrapulsation. The latter effect is most prominent at the referential timing. Too early or late timings (-100 ms and less, 100 ms and more) seems rather ineffective.

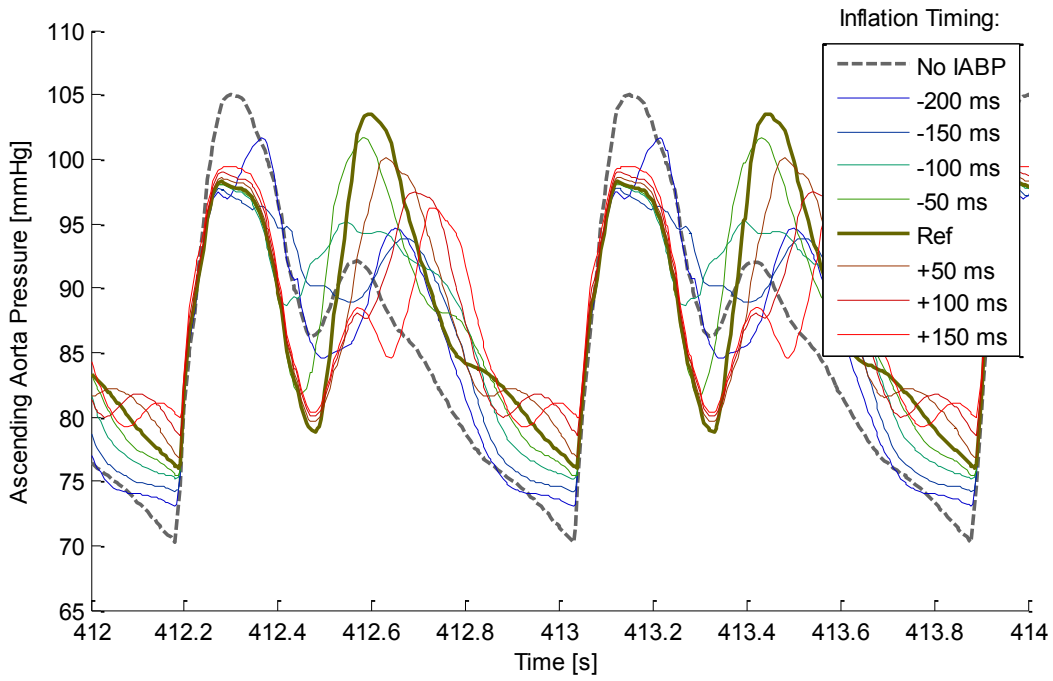

Chart 66: Aortic Pressure (IABP Inflation Timing)

The p-V diagram of left ventricle (Chart 67) confirms the reduction in afterload, which is approximately constant, i.e. not being affected by inflation timing.

Cardiac power output and stroke work (Chart 68) seem to be a little lower with their minimum at around -50ms timing. Increase in the estimates is caused by higher mean aortic pressure, which is, however, due to additional mechanical work produced by the IABP device – therefore, the estimates are biased.

The sudden jump at around -100ms timing is a result of the method used for calculation of the indicators. The ejection phase is supposed to correspond with the positive flow through the aortic valve. If using IABP, the pump deflation causes a pressure drop in aorta, leading to additional release

of blood from the left ventricle even though the systolic phase is already over and the heart exerts no further effort. When the pressure drop is small and the extra flow is minute, the mean ventricular pressure during ejection used for computation of the indicators is negatively affected (as in case of the -100ms timing).

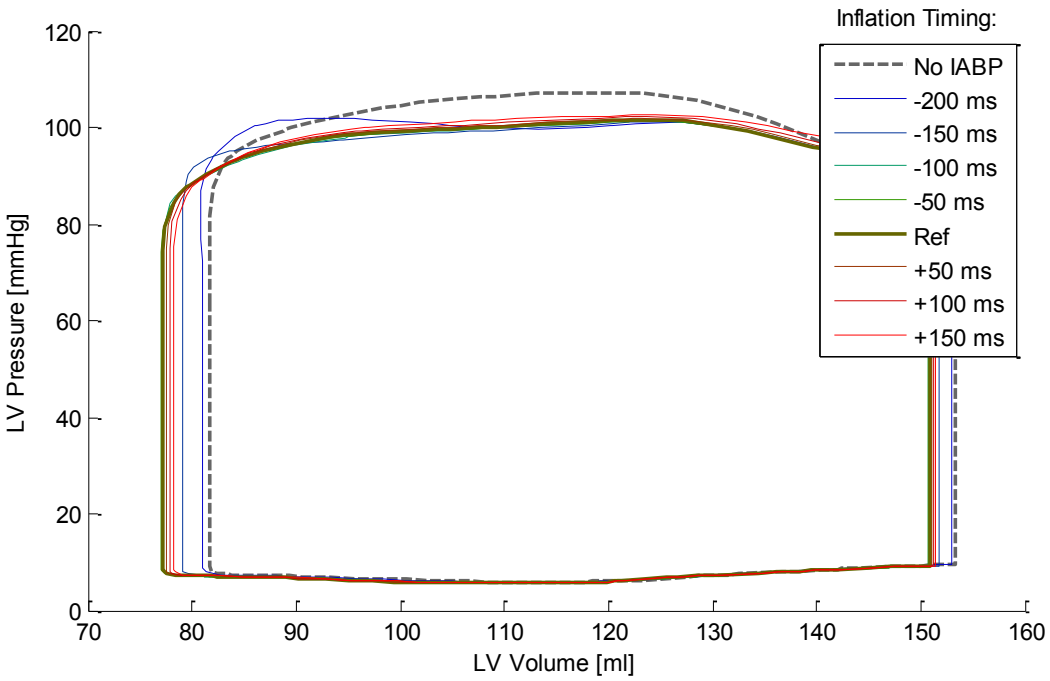

Chart 67: LV p-V Diagram (IABP Inflation Timing)

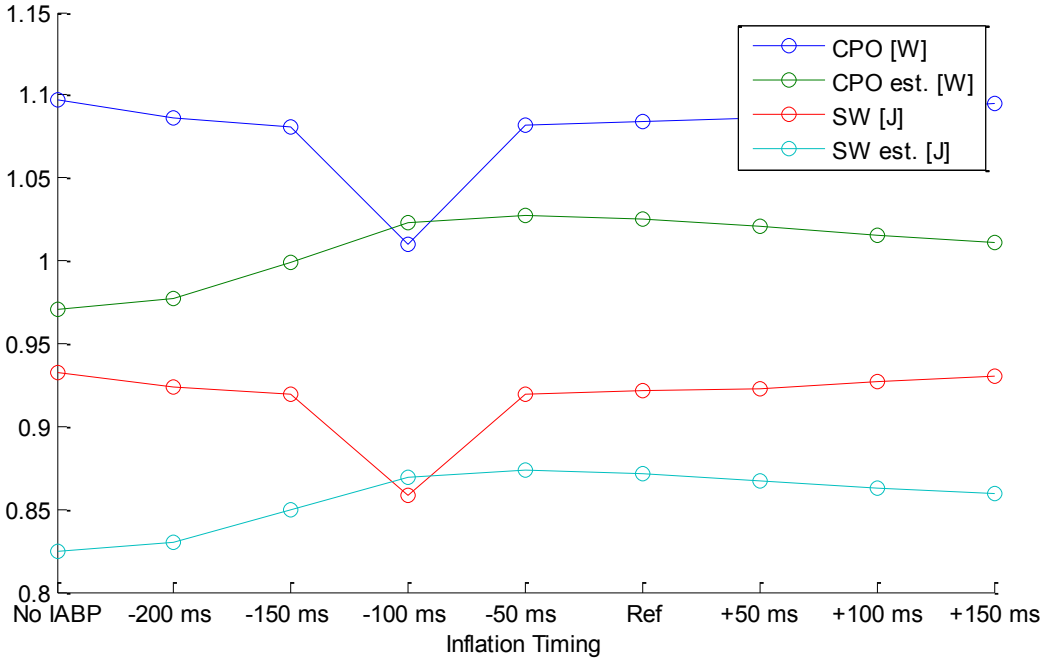

Chart 68: Cardiac Power Output and Stroke Work (IABP Inflation Timing)

Stroke volume and mean aortic pressure (Chart 69) are increased with their maximum between -100 ms and the referential timing. Earlier timings result in a faster decrease comparing to later timings.

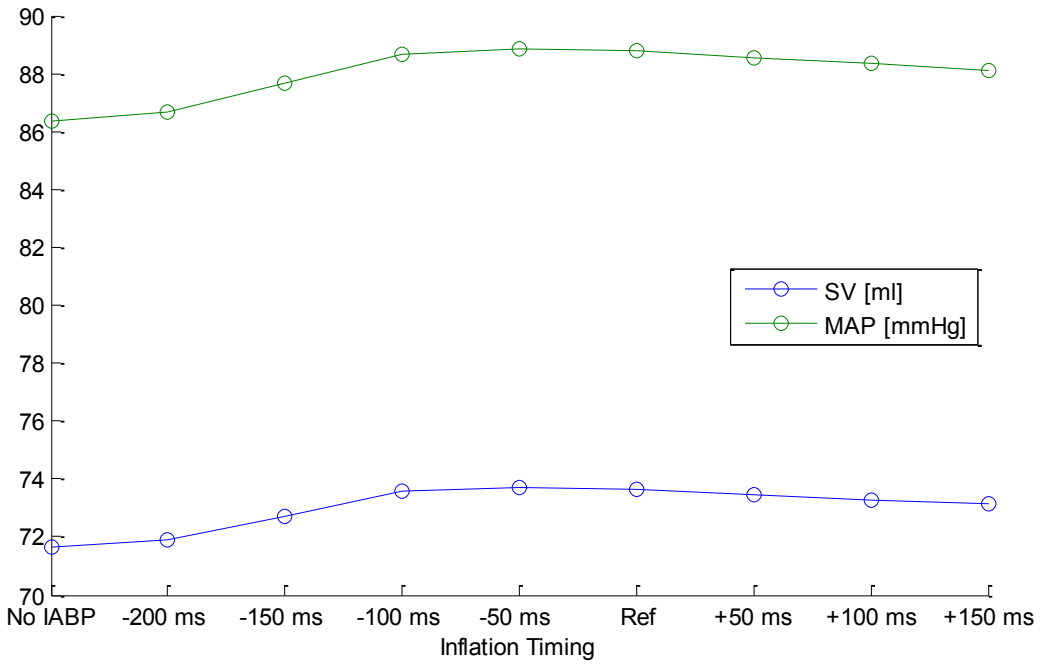

Chart 69: Stroke Volume and Mean Aortic Pressure (IABP Inflation Timing)

Coronary flow increased (Chart 70), most notably with the referential timing.

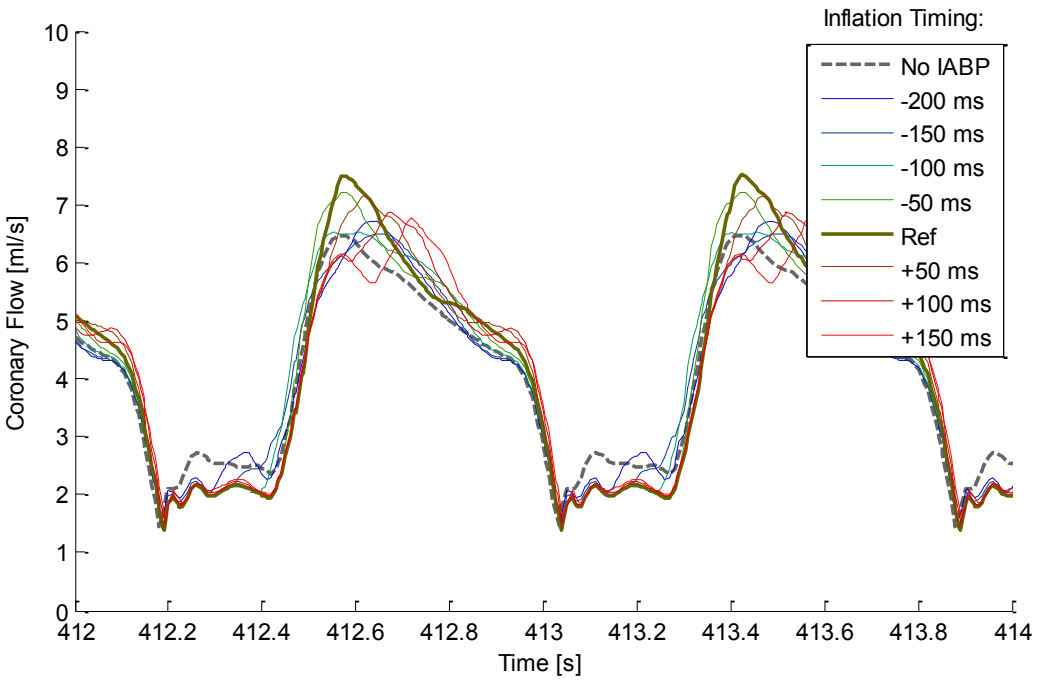

Chart 70: Coronary Flow (IABP Inflation Timing)

Flow through brachiocephalic artery (Chart 71) is a little increased during the diastole phase. In case of too early timings (-100 ms and less), however, there is strong backward outflow, leading to worsening the total flow.

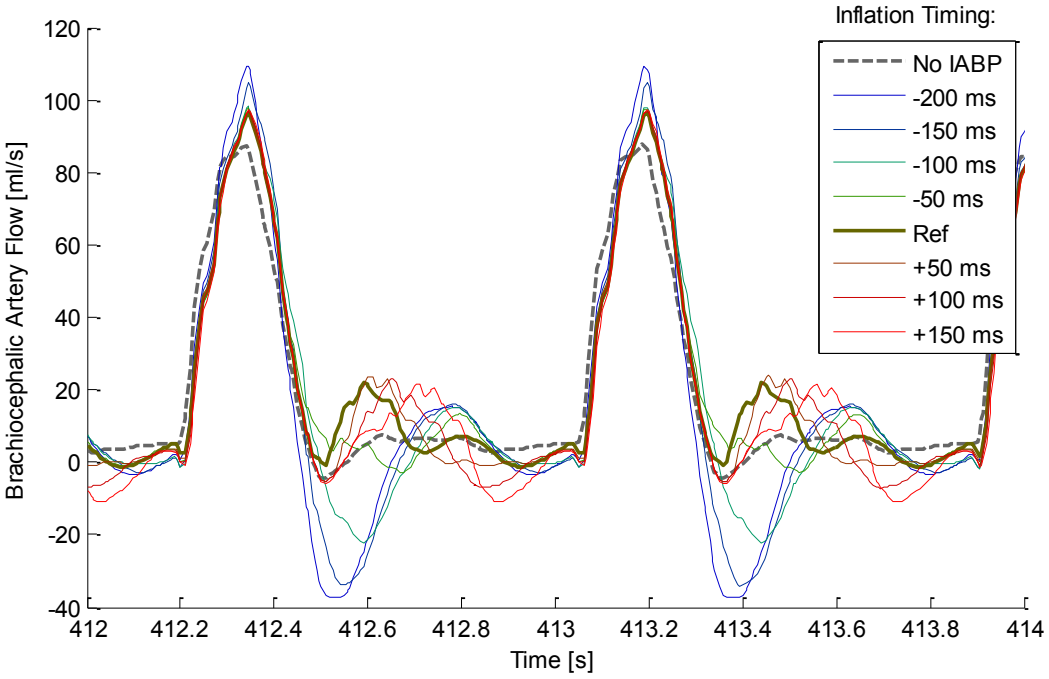

Chart 71: Brachiocephalic Artery Flow (IABP Inflation Timing)

The situation is similar with flow through left common carotid (Chart 72).

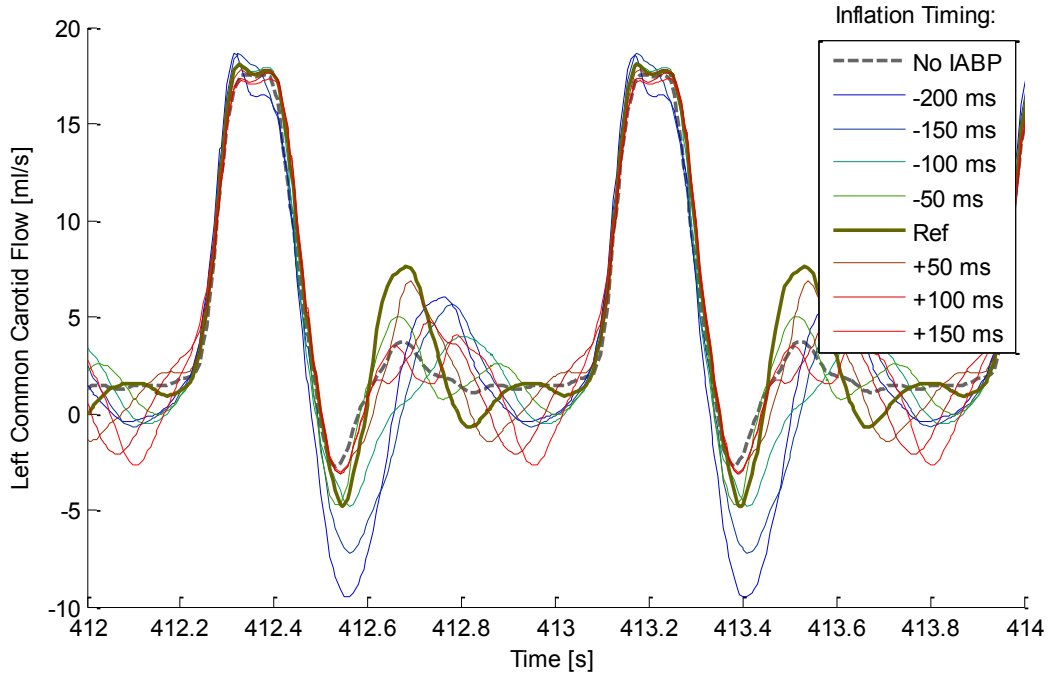

Chart 72: Left Common Carotid Flow (IABP Inflation Timing)

In abdominal aorta (Chart 73), the flow is also increased. The total flow does not seem to be dependent on the timing although the location of the additional flow peak caused by contrapulsation is correlated with the inflation timing.

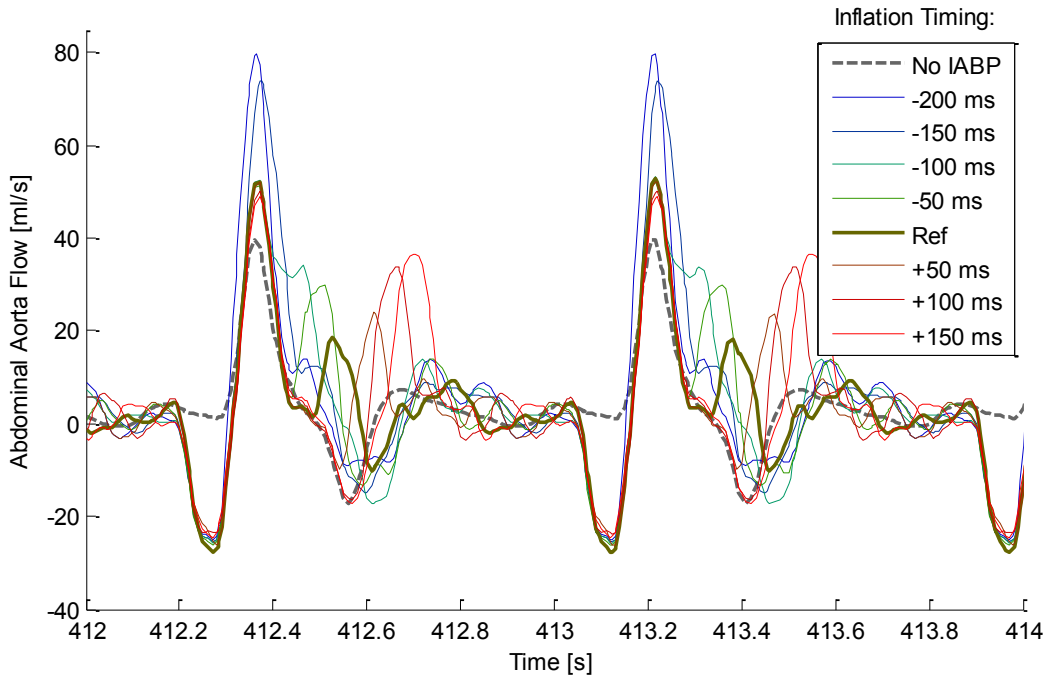

Chart 73: Abdominal Aorta Flow (IABP Inflation Timing)

Cardiac output (Chart 74) is dependent on timing, with its peak at -50 ms and the referential timing. It is also correlated with preload.

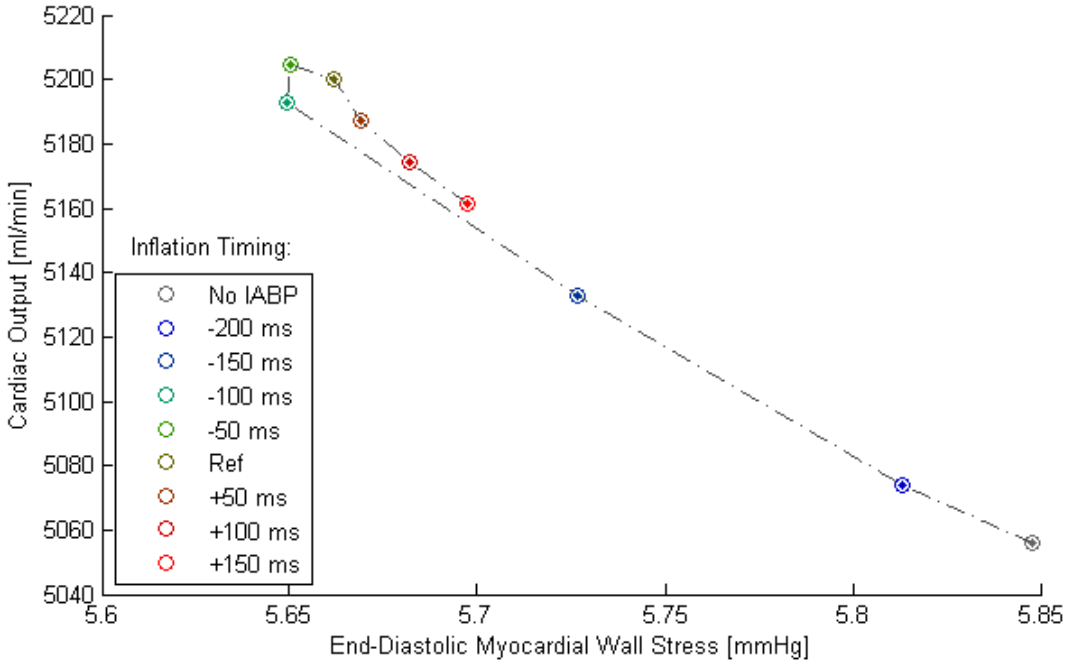

Chart 74: Cardiac Output and Preload Dependency (IABP Inflation Timing)

3.5.2) Deflation Timing

The recommended setting for deflation is located at the end of diastole (Krishna & Zacharowski, 2009) – in this case 280 ms. Effects was studied on timings adjusted from -200 ms to +150 ms by 50ms steps.

As in the inflation timing, the lowest systolic peak in ascending aorta (Chart 75), and highest end-diastolic pressure, simultaneously, is attained at the referential timing. Delayed deflation leads to higher systolic pressure and preload.

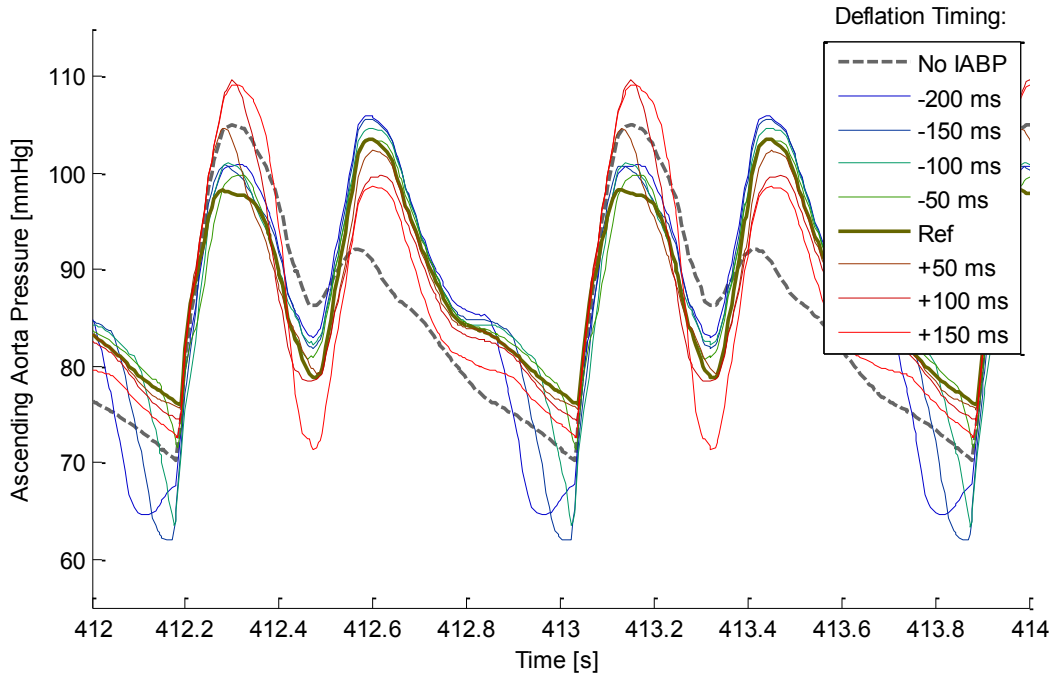

Chart 75: Aortic Pressure (IABP Deflation Timing)

Unlike inflation timing, the p-V diagram of left ventricle (Chart 76) indicates variations in afterload, which may be for delayed deflation timing even higher than if no IABP device is implanted.

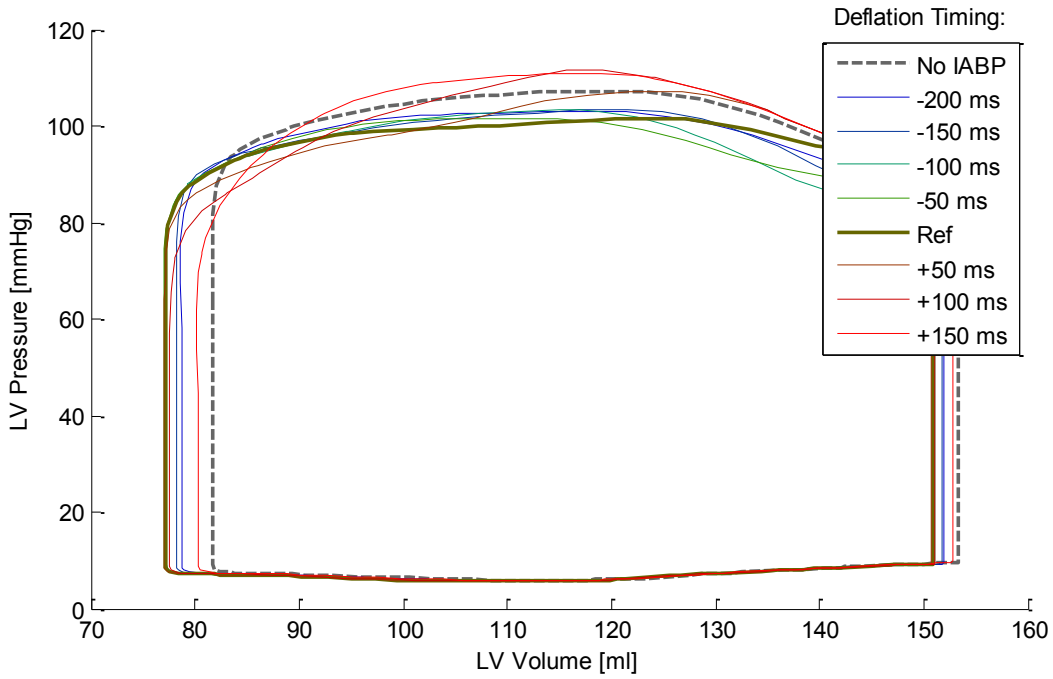

Chart 76: LV p-V Diagram (IABP Deflation Timing)

Cardiac power output and stroke work (Chart 77) have similar tendencies (and biases) as in case of adjusting inflation timing. The minimum is found at -100ms timing.

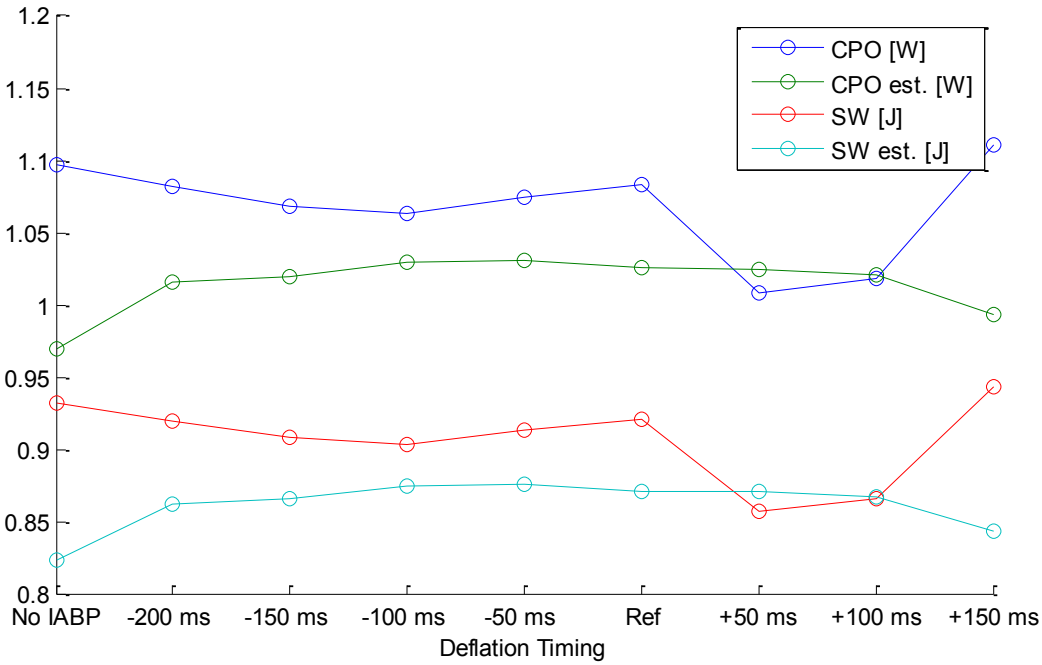

Chart 77: Cardiac Power Output and Stroke Work (IABP Deflation Timing)

Stroke volume and mean aortic pressure (Chart 78) reach maximum for -50 and -100ms timings.

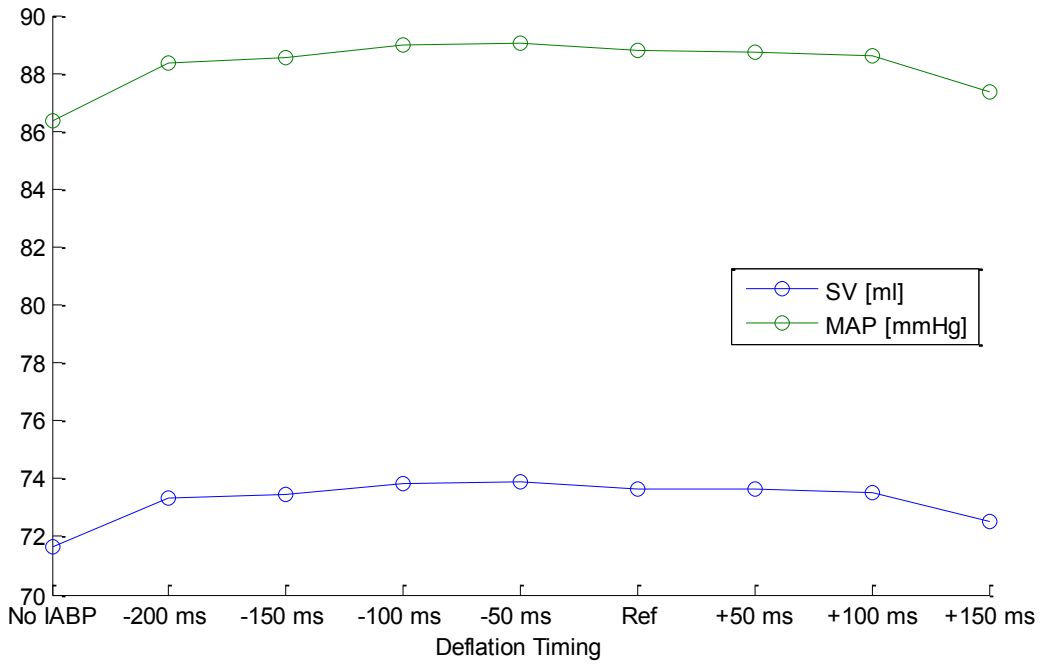

Chart 78: Stroke Volume and Mean Aortic Pressure (IABP Deflation Timing)

Flow through coronary arteries (Chart 79) is not affected by deflation timing.

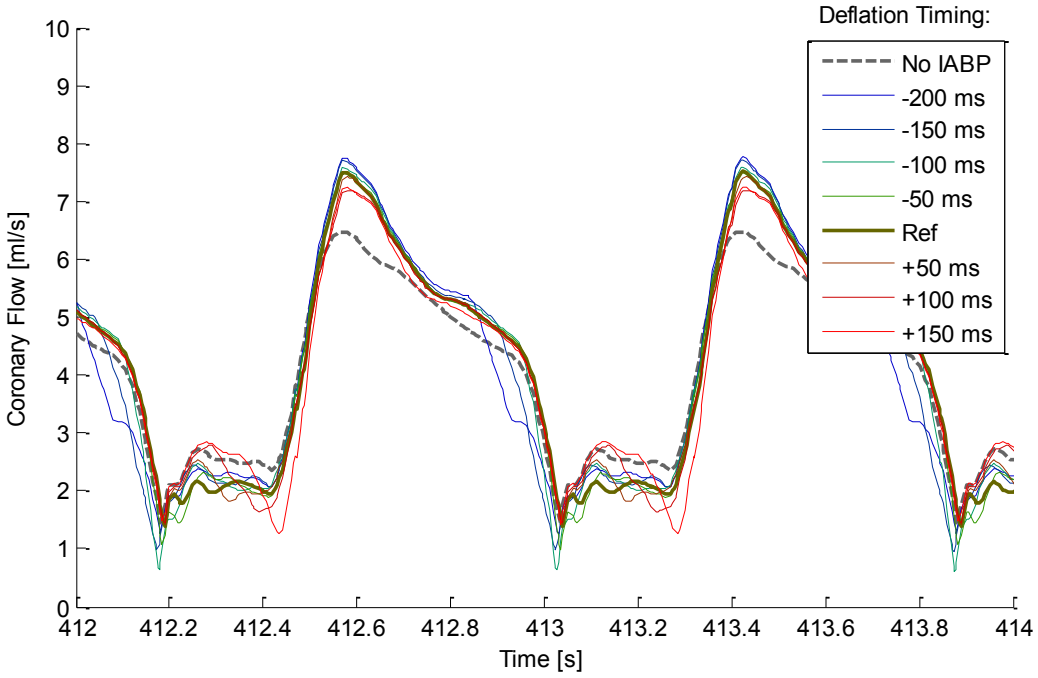

Chart 79: Coronary Flow (IABP Deflation Timing)

Flow through brachiocephalic artery (Chart 80) may be lower for earlier deflation timings.

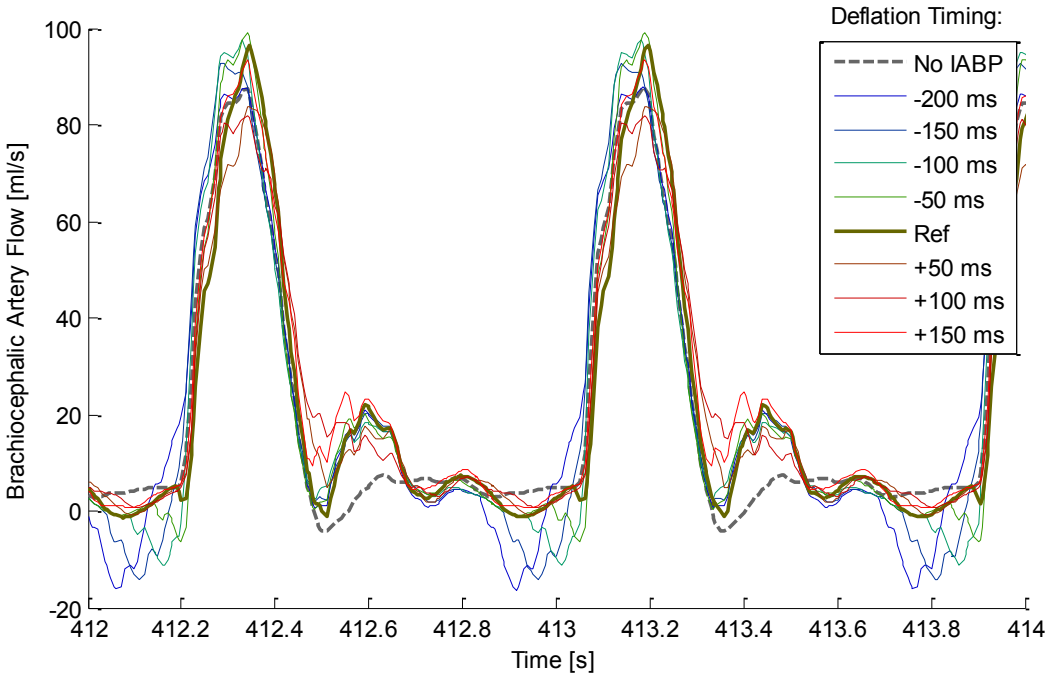

Chart 80: Brachiocephalic Artery Flow (IABP Deflation Timing)

On the other hand, flow through left common carotid (Chart 81) is higher for delayed timings and for the referential timing is minimal.

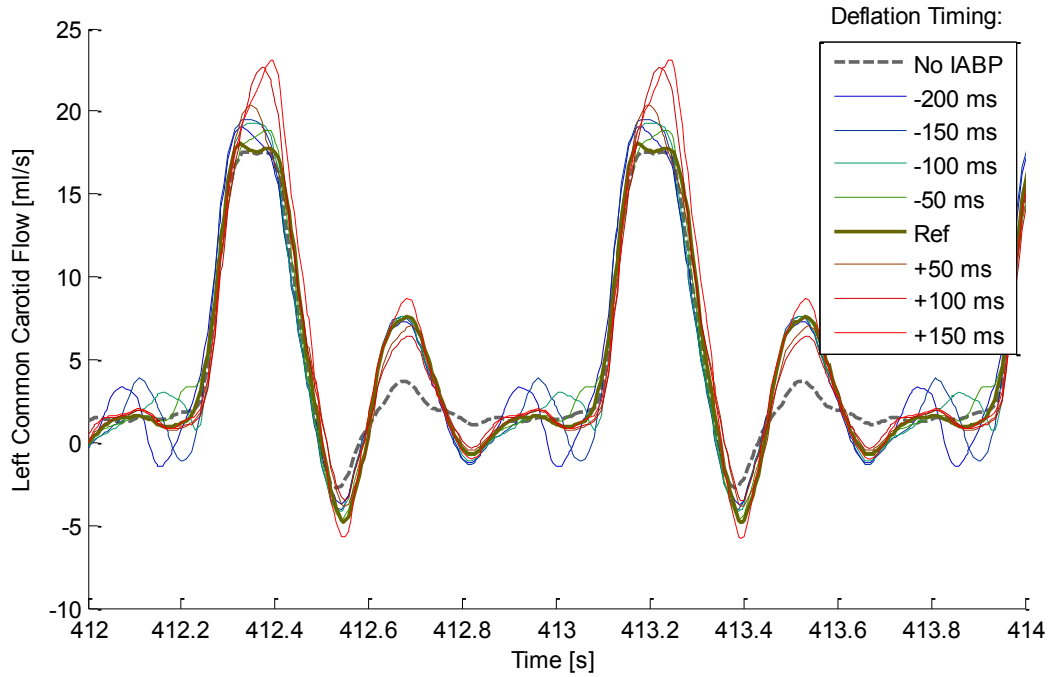

Chart 81: Left Common Carotid Flow (IABP Deflation Timing)

Flow through abdominal aorta (Chart 82) is decreased for all timings.

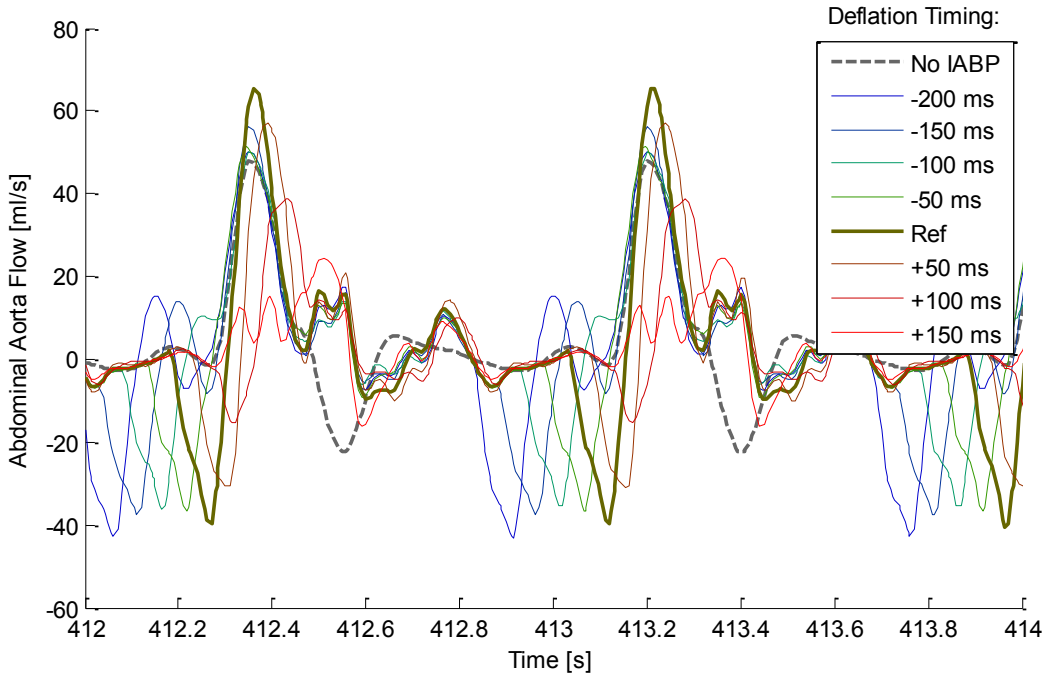

Chart 82: Abdominal Aorta Flow (IABP Deflation Timing)

Maximal cardiac output and minimal preload (Chart 83) are realized with the timing between -50 and +50 ms.

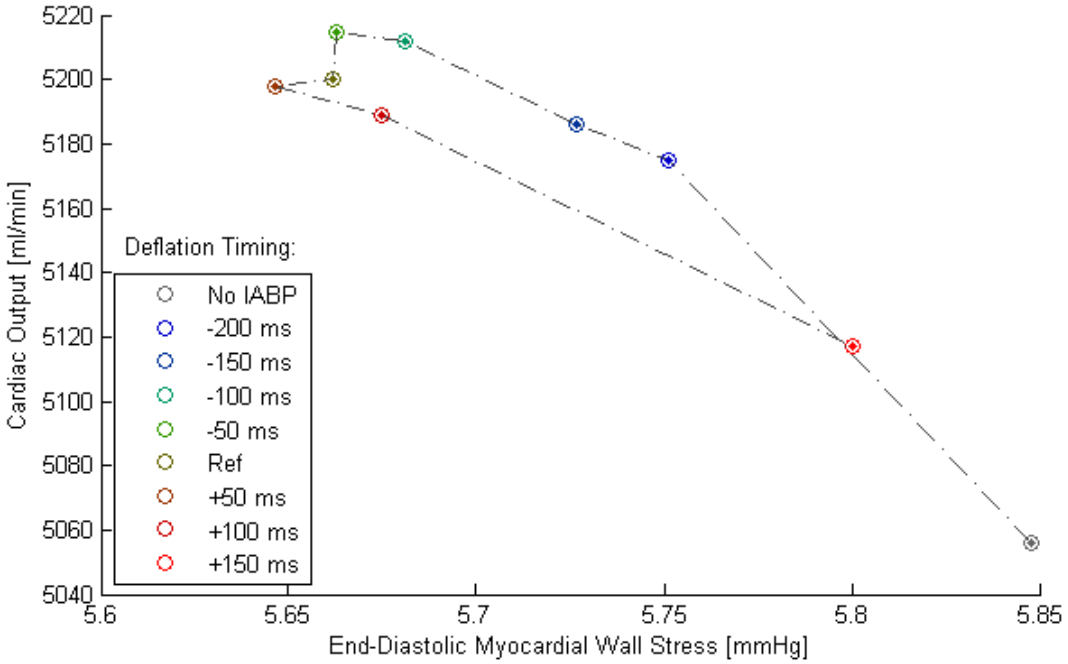

Chart 83: Cardiac Output and Preload Dependency (IABP Deflation Timing)

3.5.3) Summary

When using IABP, the right inflation timing is important for improvements in blood flow into coronaries and arteries in the aortal arch by synchronization of its pulse with the incoming reflection wave, and thus, combining their pressure effect. Improper timing can, on the other hand, result in reduction of blood flow through vital organs.

The deflation timing has impact on cardiac preload, for which the referential timing is optimal. The flow through left common carotid artery might be increased with later timings although it would be for the price of higher preload.

3.6) Cardiac Supports II: Effect of ECMO Settings

Testing the ECMO support was performed with a scenario of failing heart with contractility decreased to 30 % in all walls including atria walls.

3.6.1) Pulsatility and Placement

ECMO was set to the mean referential flow of 5 l/min and connected to either ascending aorta (AA) or thoracic aorta (TA) in both pulsatile and non-pulsatile modes. The pulsatile mode was simulated with parabolic-like pulses (as demonstrated in Chart 14) and a default timing (0 with respect to the cardiac cycle).

Aortal pressure waveform (Chart 84) appears to be recovered in the pulsatile mode. The systolic peak in ascending aorta is reduced in case of connection to thoracic aorta. The connection location is unimportant for the non-pulsatile mode.

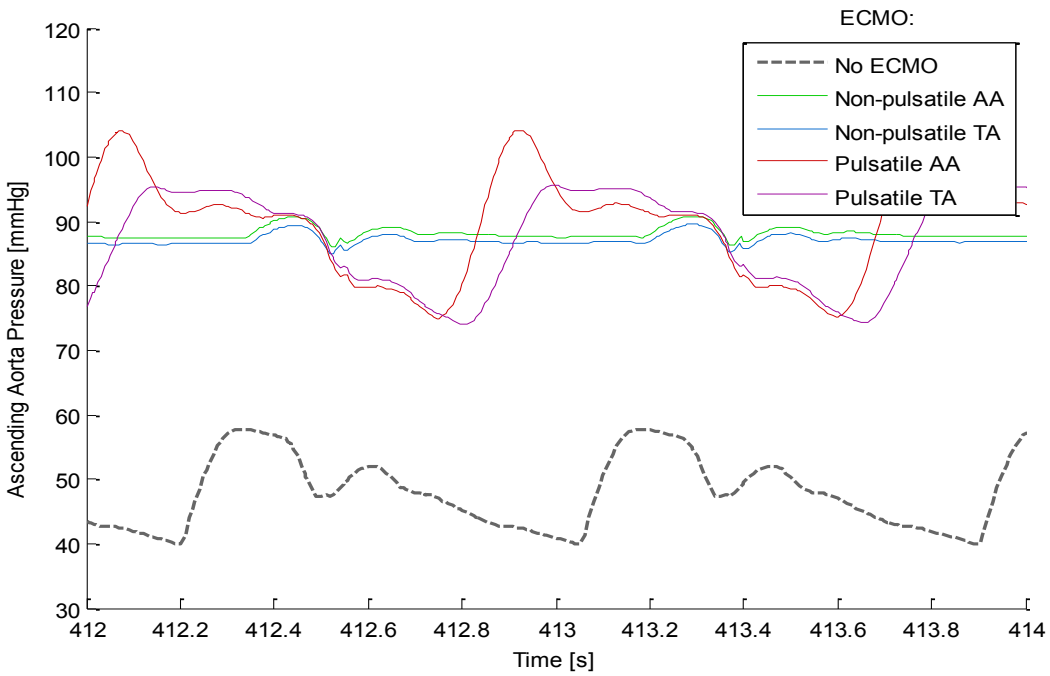

Chart 84: Aortic Pressure (ECMO Pulsatility and Placement)

Preload is almost doubled due to the pressure from the ECMO inflow (Chart 85), preventing the heart from ejection.

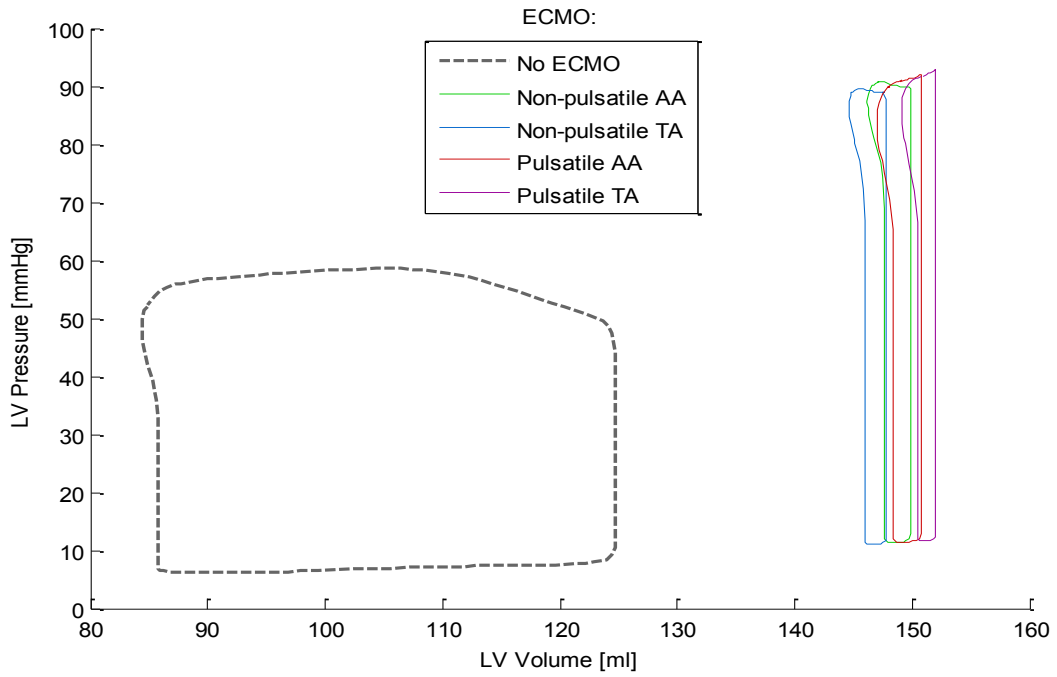

Chart 85: LV p-V Diagram (ECMO Pulsatility and Placement)

Sarcomeres (Chart 86) remain stretched, as the heart cannot pump and accumulates a larger volume of blood.

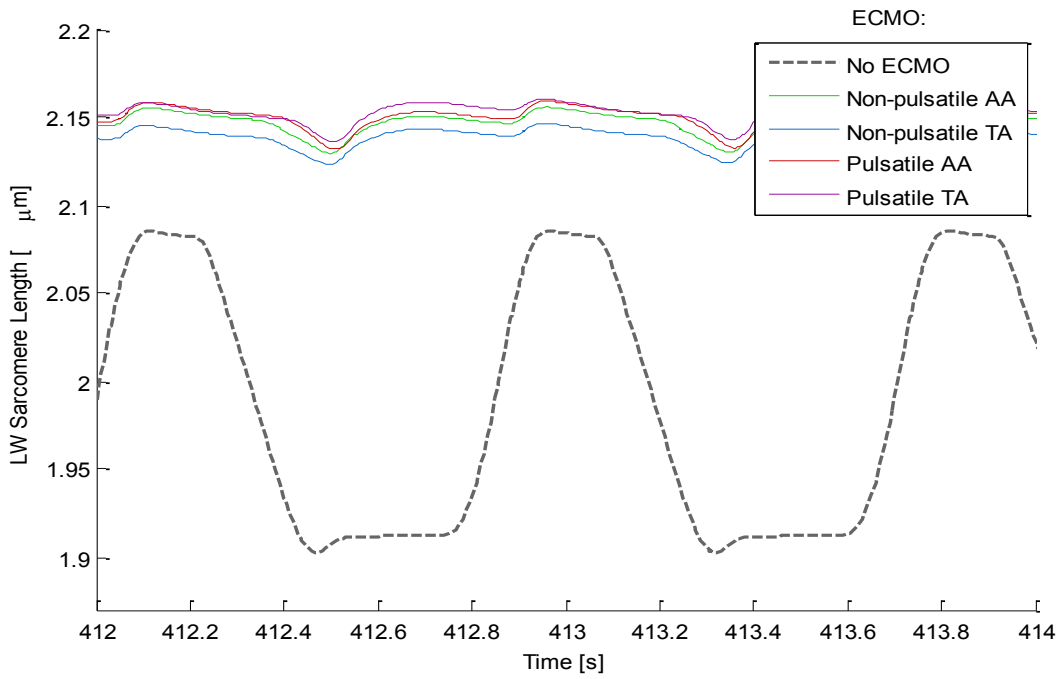

Chart 86: LW Sarcomere Length (ECMO Pulsatility and Placement)

Stroke volume (Chart 87) is almost zero and the mean aortic pressure returns to around 90 mmHg. There are no larger differences between the ECMO settings. If connected to ascending aorta, stroke volume is a little higher comparing to insertion into thoracic aorta.

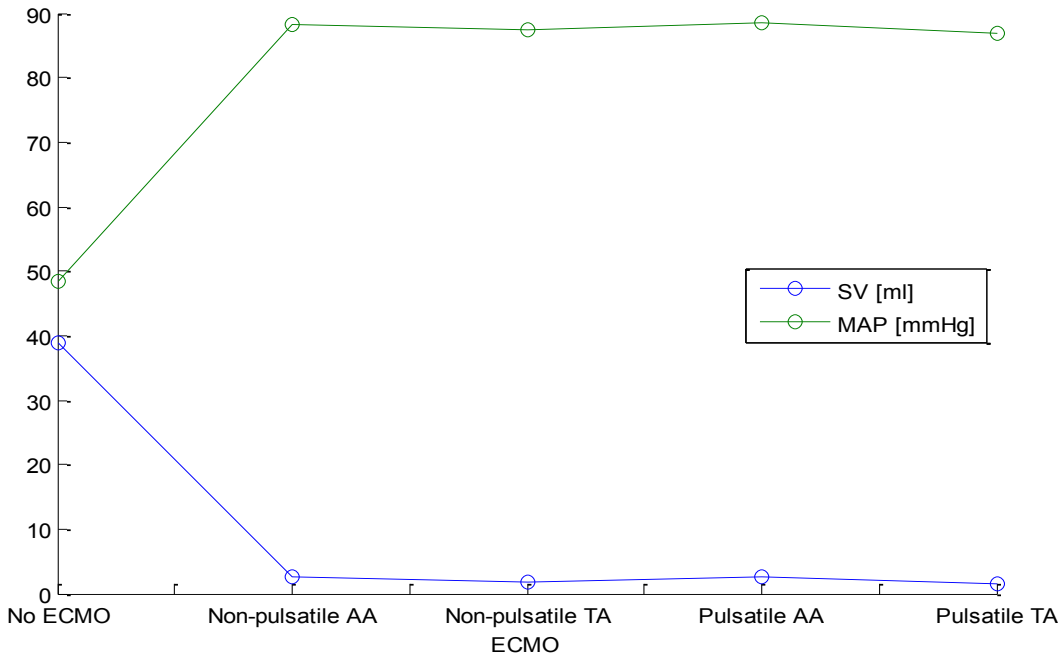

Chart 87: Stroke Volume and Mean Aortic Pressure (ECMO Pulsatility and Placement)

The trend in cardiac power output and stroke work (Chart 88) is similar to that of stroke volume.

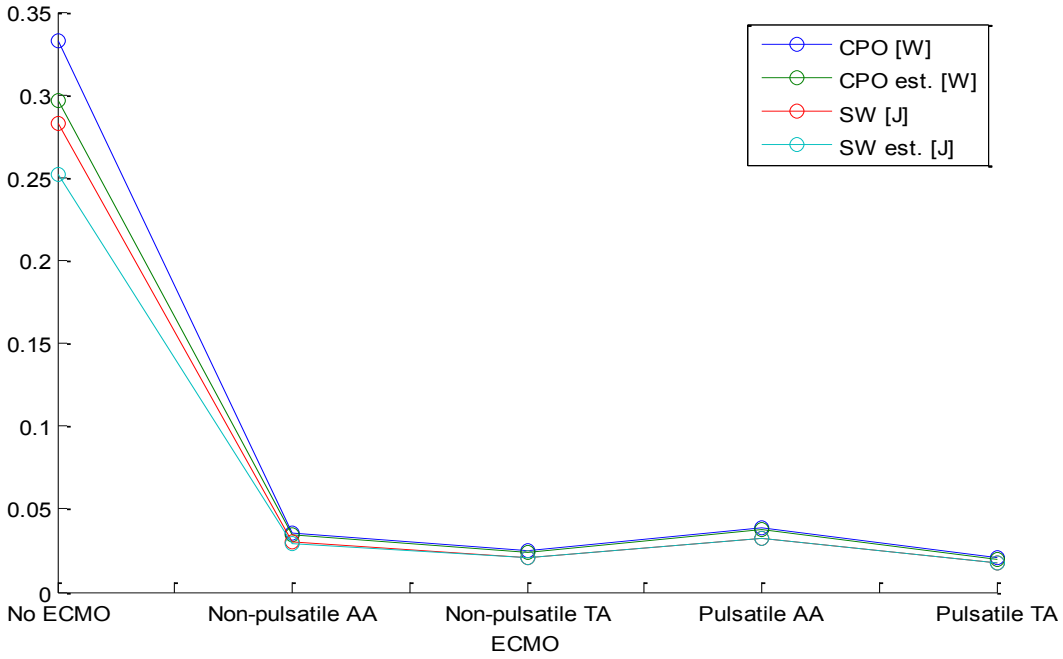

Chart 88: Cardiac Power Output and Stroke Work (ECMO Pulsatility and Placement)

Coronary flow (Chart 89) is improved in all cases. In case of the pulsatile ECMO connected to thoracic aorta, the improvement is a little lower.

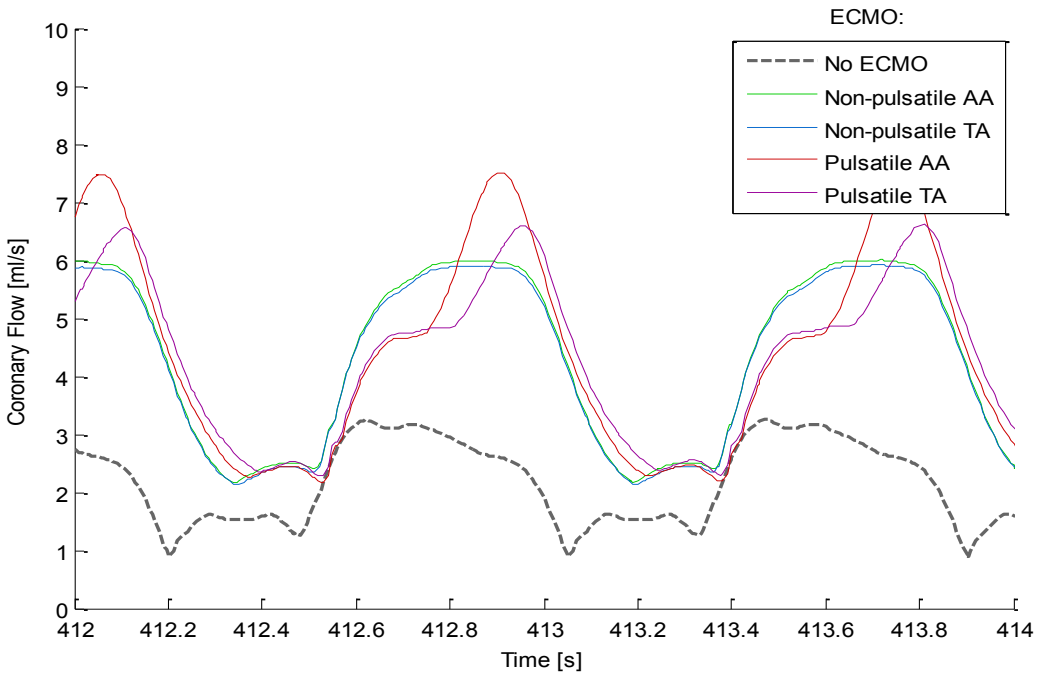

Chart 89: Coronary Flow (ECMO Pulsatility and Placement)

Flow through brachiocephalic artery (Chart 90) is improved only for a connection to ascending aorta. Plugging into thoracic aorta results in significantly decreased flow regardless of the ECMO mode.

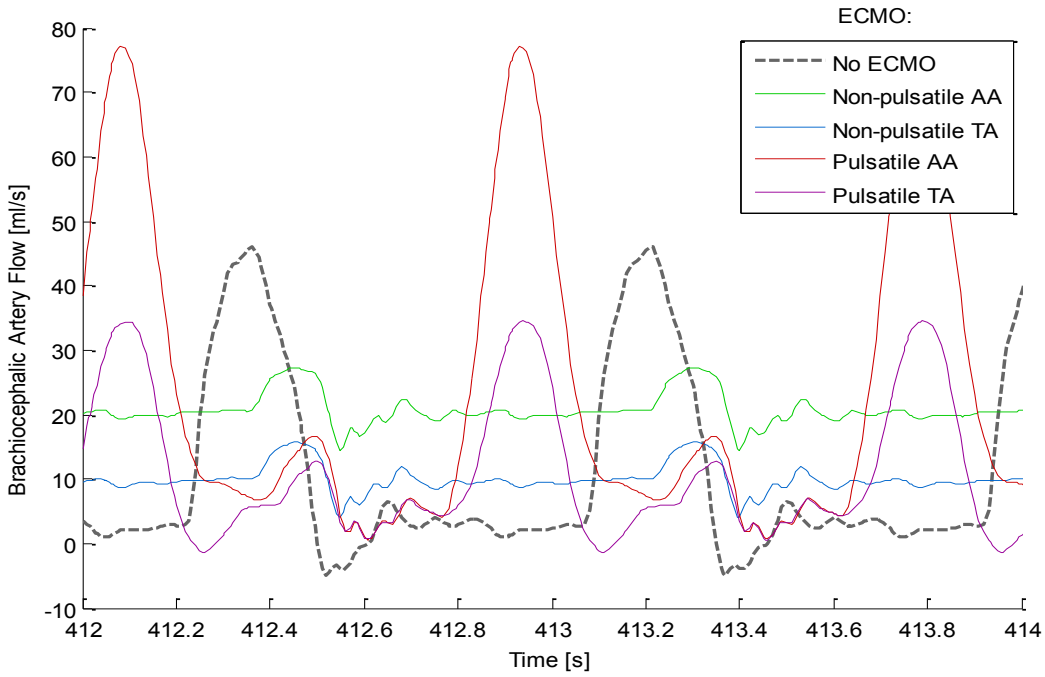

Chart 90: Brachiocephalic Artery Flow (ECMO Pulsatility and Placement)

Flow pattern through left common carotid (Chart 91) exhibits the equivalent trend as for brachiocephalic artery.

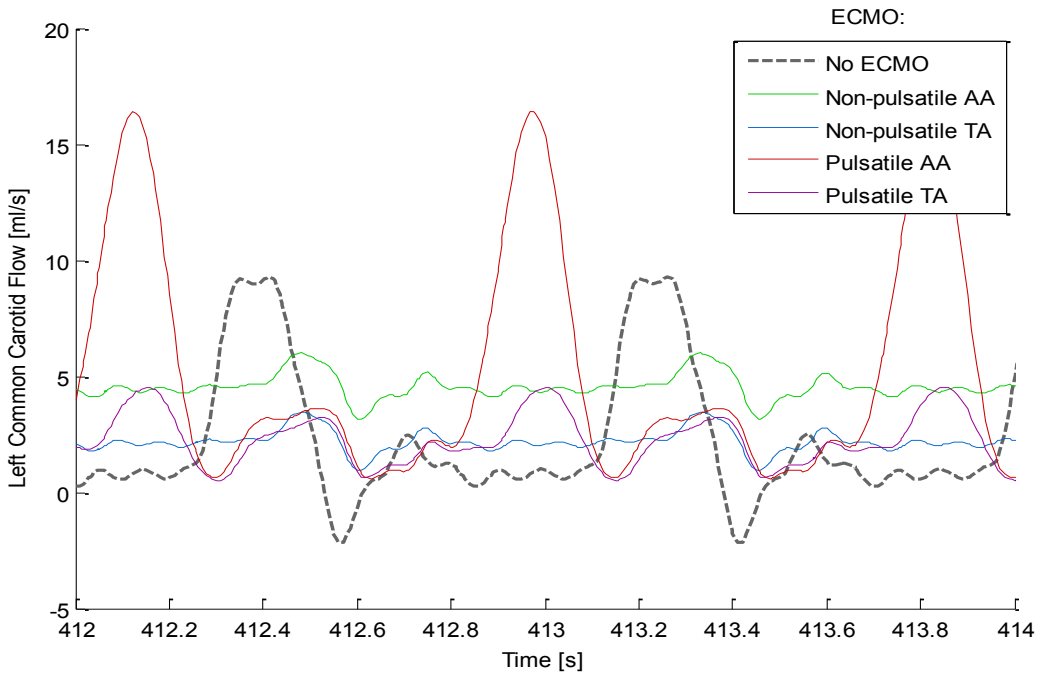

Chart 91: Left Common Carotid Flow (ECMO Pulsatility and Placement)

Flow in abdominal aorta (Chart 92) is a little improved, the rise is more apparent in case of connecting to thoracic aorta.

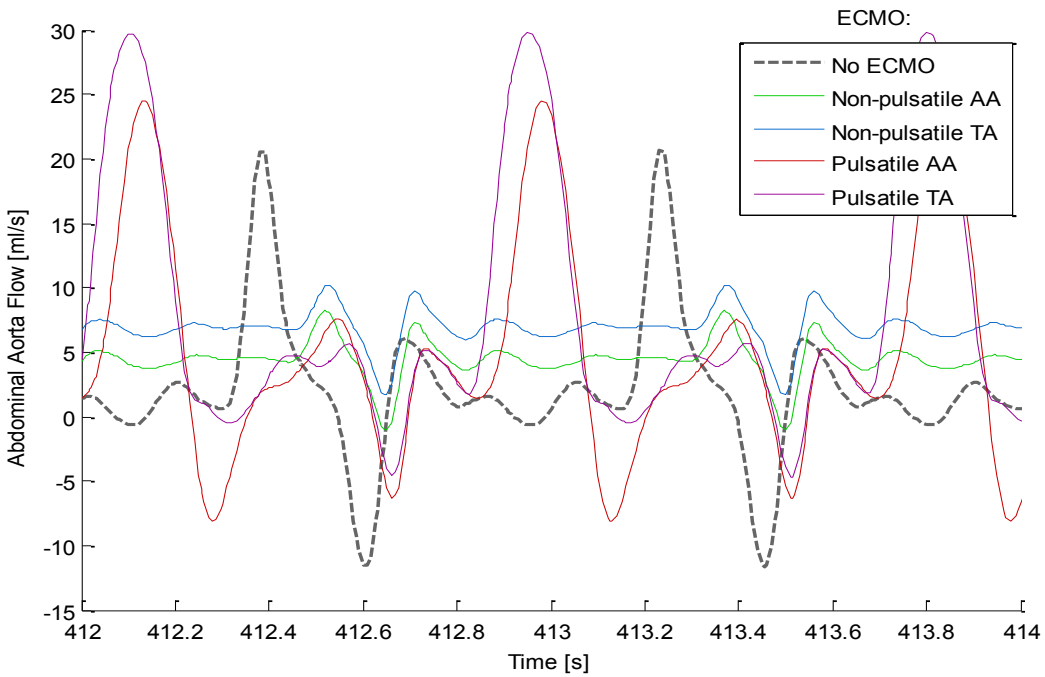

Chart 92: Abdominal Aorta Flow (ECMO Pulsatility and Placement)

3.6.2) Pulse Timing

Investigating an effect of pulse timing was realized with the same settings as for the pulsatile ECMO connected to ascending aorta from the previous pathological scenario. The timing is referenced to the beginning of the cardiac cycle and adjusted with 100ms increments to cover the whole period.

The aortic pressure waveforms (Chart 93) result from a combination of the ECMO pulse and the left ventricular systole. When synchronized with the dicrotic notch and the following wave reflection, the pressure peak is higher.

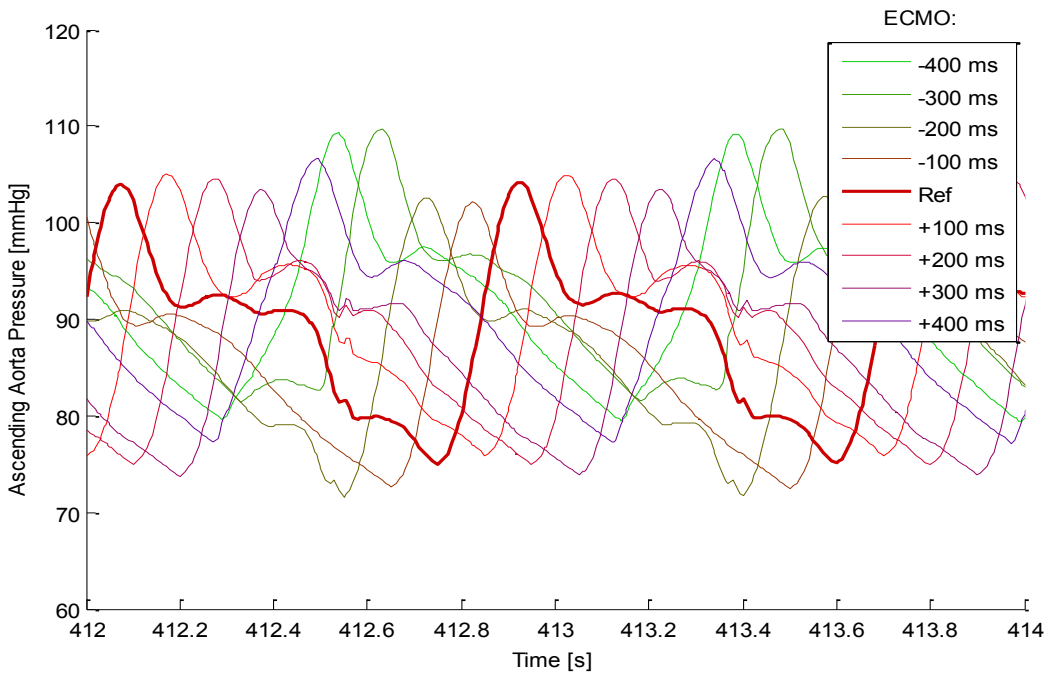

Chart 93: Aortic Pressure (ECMO Pulse Timing)

The p-V diagrams of left ventricle (Chart 94) differ for each timing. Filling volumes and preload are higher for later timings.

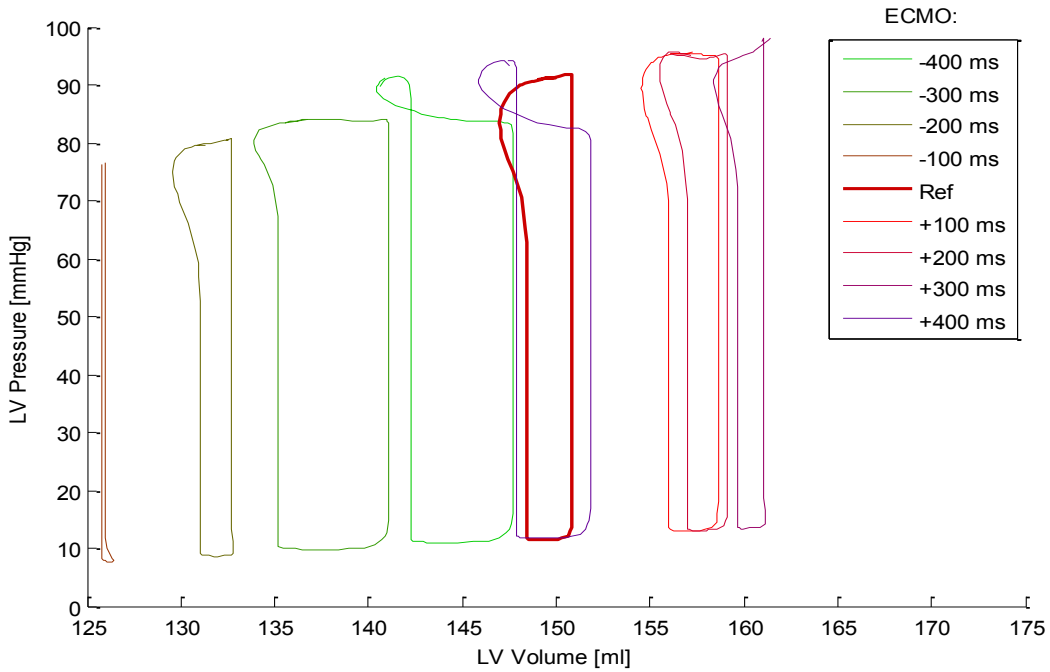

Chart 94: LV p-V Diagram (ECMO Pulse Timing)

Cardiac power output and stroke work (Chart 95) range between 0 and 0.1 W or J, respectively. Pulsating in the middle of left ventricular diastole (timing -100 ms) prevents the heart from pumping.

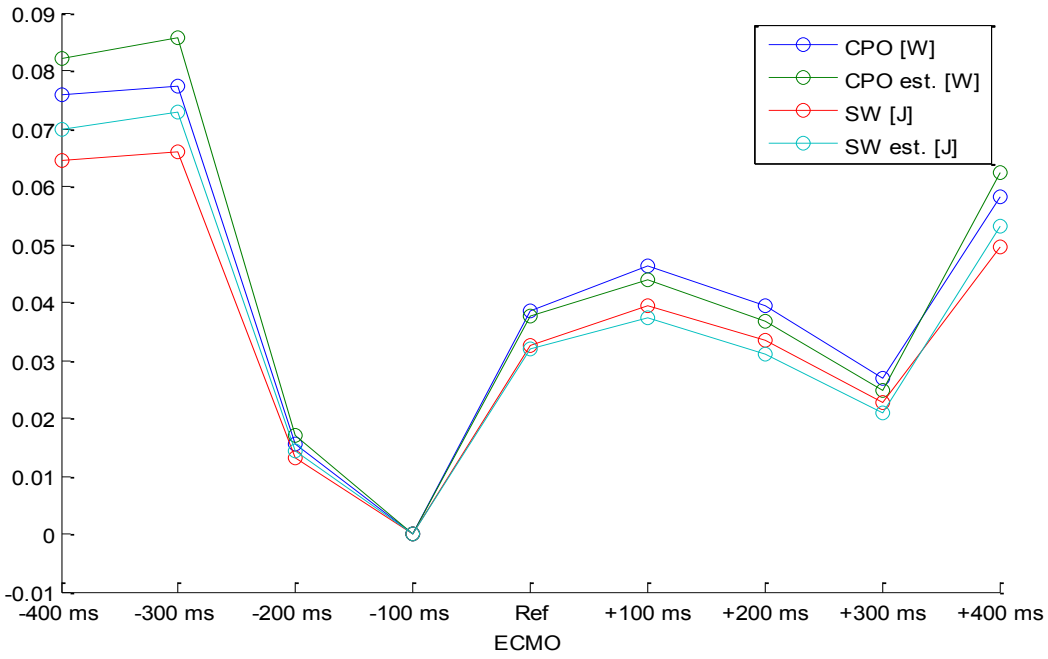

Chart 95: Cardiac Power Output and Stroke Work (ECMO Pulse Timing)

Stroke volume and mean aortic pressure (Chart 96) exhibit the same trend. The stroke volume ranges between 0 and 7 ml.

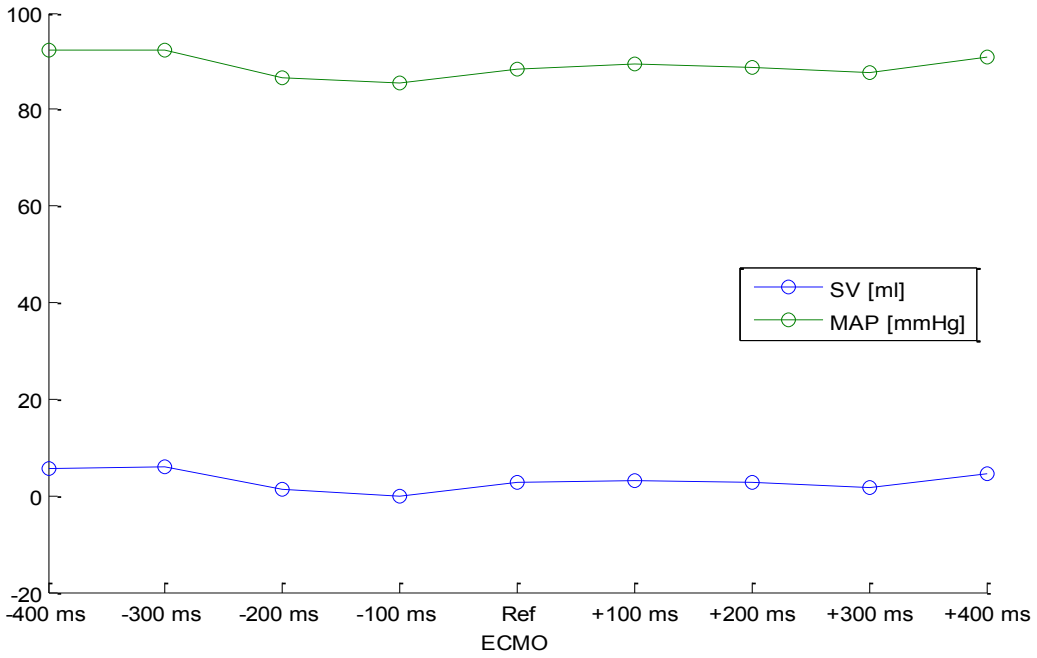

Chart 96: Stroke Volume and Mean Aortic Pressure (ECMO Pulse Timing)

Flow through various arteries (Figures 97 and 98) is also lower when the heart cannot eject against the ECMO pulse (-100 ms) and higher if the ECMO pulse is synchronized to the end of left ventricular systole (-300 ms).

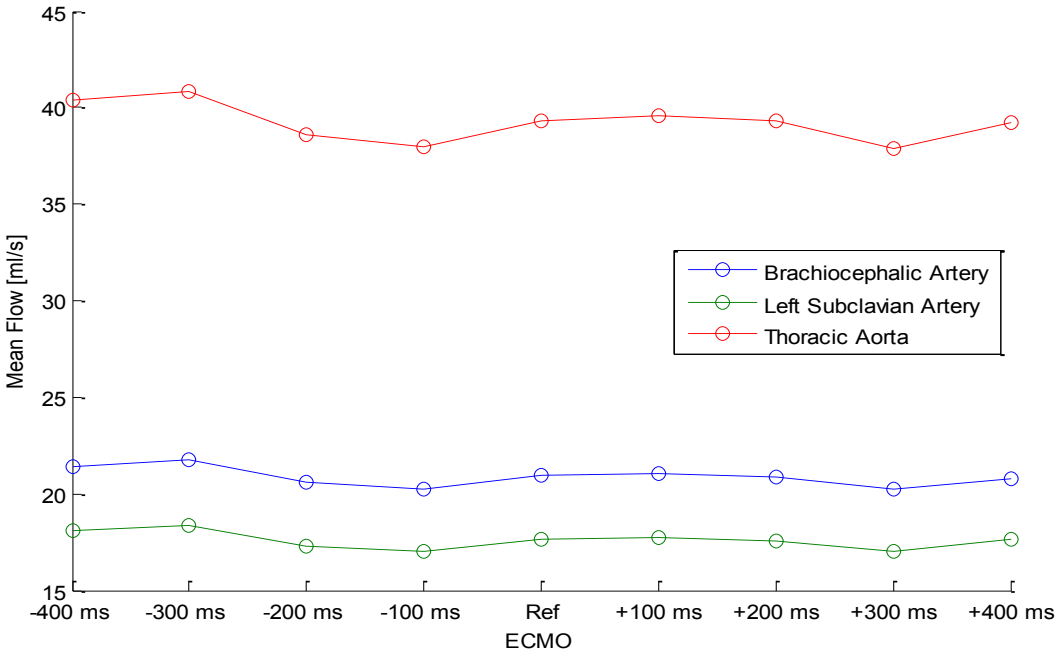

Chart 97: Mean Flow Through Main Arteries I (ECMO Pulse Timing)

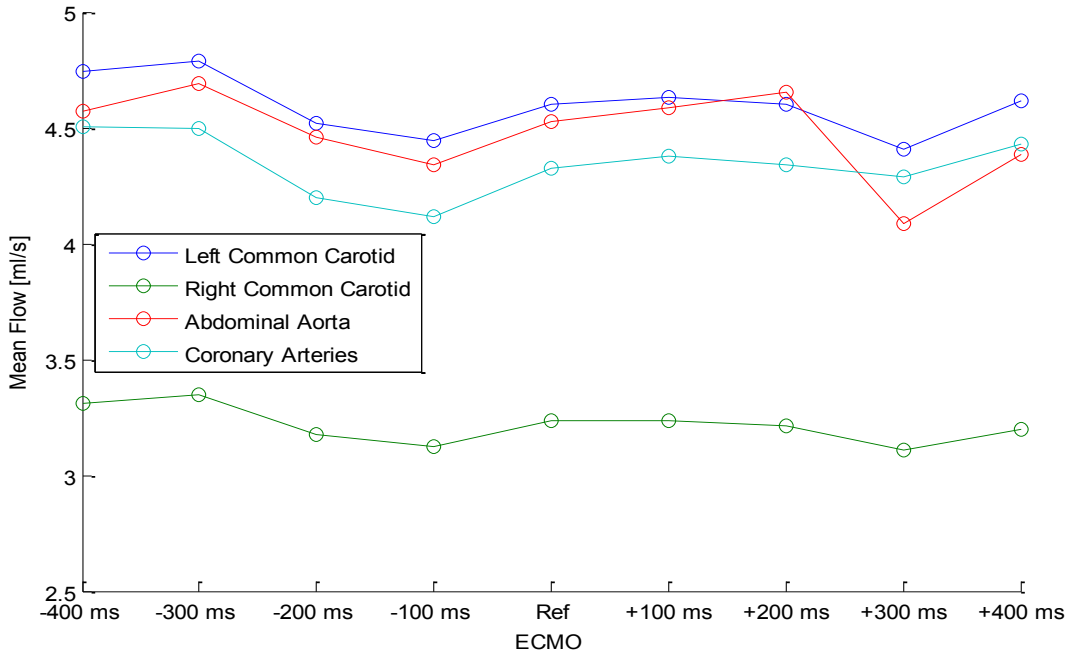

Chart 98: Mean Flow Through Main Arteries II (ECMO Pulse Timing)

The dependency of left ventricular preload and cardiac output (Chart 99) indicates a large variability across the individual timings – preload ranges between 4.5 and 8.5 mmHg and cardiac output can be adjusted between 0 and 450 ml.

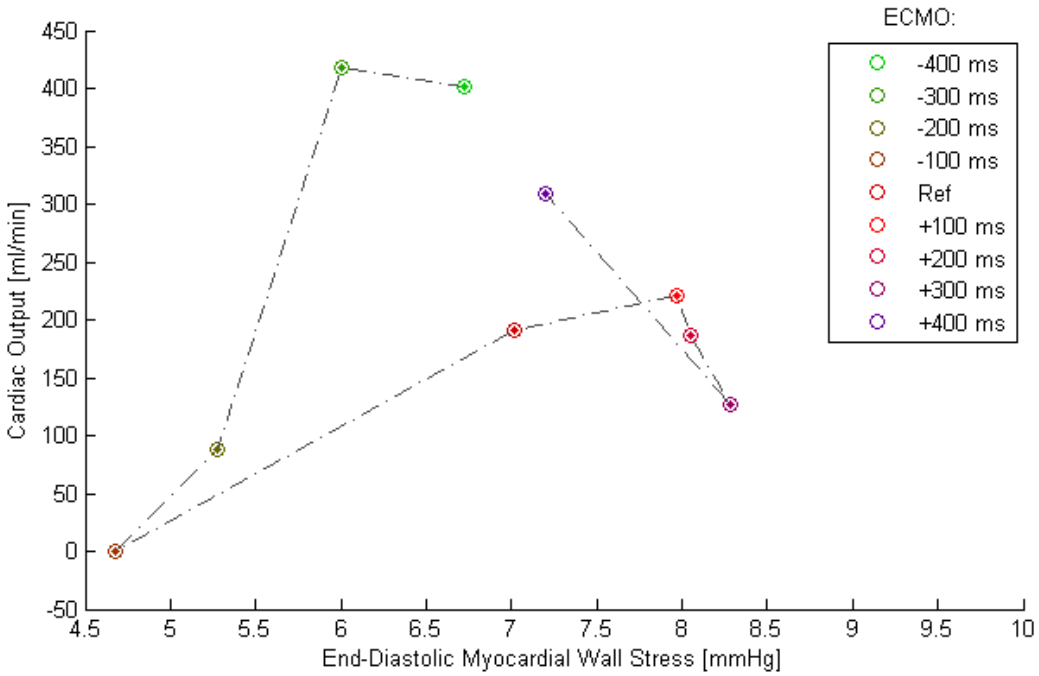

Chart 99: Cardiac Output and Preload Dependency (ECMO Pulse Timing)

Similarly for the preload of right ventricle represented by end-diastolic volume of right atrium (Chart 100) although the preload is minimal for the referential timing and the curve is of the opposite direction (clockwise with respect to increasing timing).

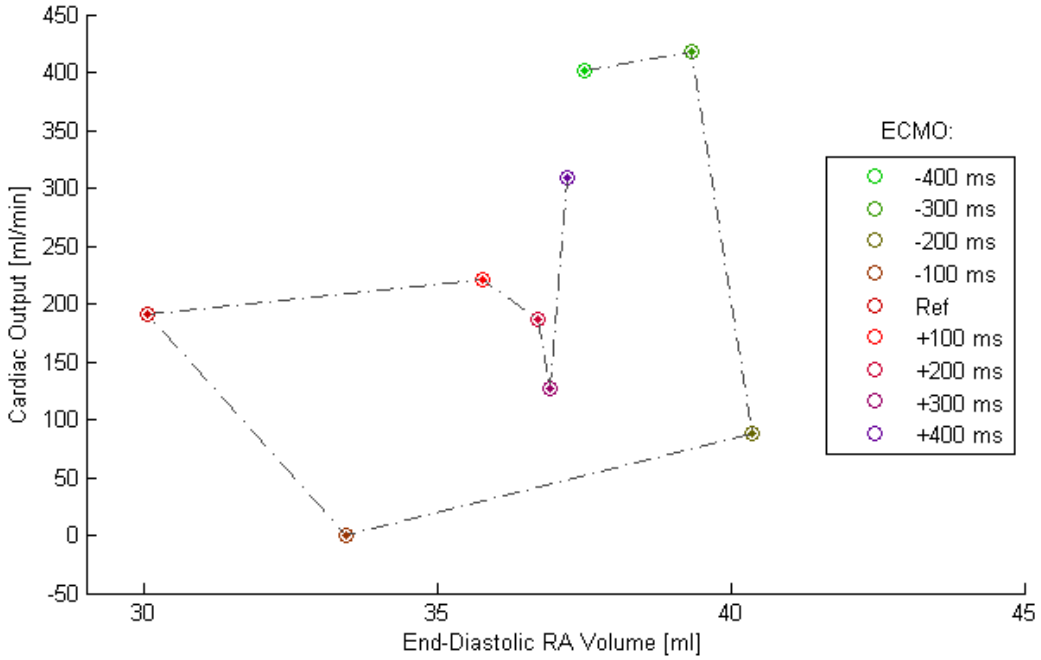

Chart 100: Cardiac Output and EDV-RA Dependency (ECMO Pulse Timing)

3.6.3) Summary

Connecting ECMO to thoracic aorta may have an inverse effect on the flow through the upper body including the brain. The pulsatile and non-pulsatile type of ECMO inflow is of no importance with respect to mean flow through arteries. The flow waveforms are, however, physiological in case of the pulsatile mode, which is not true for the non-pulsatile ECMO. This difference might have an impact.

It has been illustrated that using the pulsatile ECMO device is superior to the non-pulsatile ECMO in terms of its flexibility. By adjusting the timing, the heart can be fully prevented from contraction and ejection or the stroke volume and cardiac output can be double comparing to the non-pulsatile mode while maintaining the same arterial mean flow.

This could be practically applied, supposing a reliable synchronization with the cardiac cycle: Initially, the left ventricle would be completely stopped with respect to its ejection, protecting it from unnecessary energetic consumption and providing a more restful condition for its recovery. In later phases, the timing would be gradually shifted so that the heart could slowly adapt to a higher load before a decrease in the ECMO flow.

Should the ECMO support be required for a long period, regular changes in the timing would prevent heart myofibers from constant inactivity, which could otherwise result in their atrophy (Pokorný et al., 2014).

CONCLUSION

In accordance with the primary objective, a model of human cardiovascular system – Cardio – has been built. It is based on several independent parts, mostly defined by other authors, which were coupled into one unifying model, allowing for simulation of diverse pathological conditions as well as ECMO and IABP heart supports.

The adopted models have been selected carefully, ensuring that they are well validated. Indeed, simulated results of various scenarios appear to be very realistic. Mutual compatibility of the models suggests general validity regardless any specific conditions.

The ECMO device has been designed to comply in terms of resulting flow waves rather than its real structure (generally, the flow feedback control is not applied although it is certainly not inconceivable).

An arterial tree model has been derived for systemic arteries according to their physiological dimensions and real tree structure. This submodel also performs satisfactory.

Several well-known phenomena have been demonstrated, including the Frank-Starling law. The genuine ambition of the Cardio model, however, is aimed a little higher. It has a potential of producing valid predictions and solving new, topical questions, as started with a brief analysis of effects of the heart supports with respect to their settings.

First, the results should be quantitatively assessed by a medical expert. If successfully validated, the model will be suitable for application in both educational and research environment.

It could be also integrated with higher-dimensional models to provide a meaningful closed-loop circuit while investigating a desired part of the system with high resolution.

Limitations

The current version of the model Cardio is limited in several aspects. It comprises only stressed blood volume and does not consider any patient-specific parameters such as weight, height, and body surface area. These are not needed whenever there is a wish to obtain generalized results, although in some scenarios, they could be useful.

Energetic indicators of heart are based on the mechanical work exerted. No consumption index is calculated, and therefore, the real efficiency cannot be evaluated.

The derived tree consists of arteries with static RLC characteristics. This along with a heuristically obtained coefficient for branching resistance may lead to slight distortions in pressure and flow waveforms and mildly overestimated wave reflections. The overall tendencies in propagation, however, should not be affected.

Adaptation is supported by the original version of systemic arteries only. Utilization of the adaptation protocol with arterial trees is possible (as demonstrated in Section 3.4.2) although it might potentially lead to instabilities.

Further, the ECMO support is simplified, as already mentioned. It also incorporates only resistive elements, which could lead to overly steep flow derivations in case of square pulses despite simulated delays in the pressure control. For parabolic-like pulses, the resulting flow is reasonably smooth.

Future Work

There is a lot of space for various experiments by adjusting model parameters and studying the results. The model is also eligible for additional enhancements – either by embedding new modules or by direct modifications of its core components. For instance, implementation of oxygen-related indices would provide more information about the heart energy consumption.

Contractility modeled by an approximating function could be replaced with a more complete calcium model encompassing cell dynamics including ion channels and action potentials. This could cover simulation of other phenomena such as a heart reaction on potassium overdose etc.

Ultimately, the response of autonomic nervous system could be implemented so as to be really autonomic, similarly to the adaptation process for geometry of vessels and heart.

REFERENCES

ABDOLRAZAGHI, Mona, Mahdi NAVIDBAKHSH, and Kamran HASSANI. Mathematical Modelling and Electrical Analog Equivalent of the Human Cardiovascular System. *Cardiovascular Engineering* [online]. 2010, vol. 10, issue 2, pp. 45-51 [cit. 2015-05-10]. DOI: 10.1007/s10558-010-9093-0.

ARTS, Theo, Robert S. RENEMAN, and Peter C. VEENSTRA. A model of the mechanics of the left ventricle. *Annals of biomedical engineering*. 1979, vol. 7, issue 3-4, pp. 299-318.

ARTS, Theo, Peter H. BOVENDEERD, Frits W. PRINZEN, and Robert S. RENEMAN. Relation between left ventricular cavity pressure and volume and systolic fiber stress and strain in the wall. *Biophysical journal*. 1991, vol. 59, issue 1, pp. 93-102.

ARTS, Theo, Tammo DELHAAS, Peter BOVENDEERD, Xander VERBEEK, and Frits W. PRINZEN. Adaptation to mechanical load determines shape and properties of heart and circulation: the CircAdapt model. *AJP: Heart and Circulatory Physiology* [online]. 2004, vol. 288, issue 4, H1943-H1954 [cit. 2015-05-10]. DOI: 10.1152/ajpheart.00444.2004.

ARTS, Theo, Joost LUMENS, Wilco KROON, Tammo DELHAAS, and Andrew D. MCCULLOCH. Control of Whole Heart Geometry by Intramyocardial Mechano-Feedback: A Model Study. *PLoS Computational Biology*. 2012a, vol. 8, issue 2, e1002369. DOI: 10.1371/journal.pcbi.1002369. ISSN 1553-7358.

ARTS, Theo, Koen REESINK, Wilco KROON, and Tammo DELHAAS. Simulation of adaptation of blood vessel geometry to flow and pressure: Implications for arterio-venous impedance. *Mechanics Research Communications* [online]. 2012b, vol. 42, pp. 15-21 [cit. 2015-05-10]. DOI: 10.1016/j.mechrescom.2011.10.005.

AVOLIO, Albert P. Multi-branched model of the human arterial system. *Medical and Biological Engineering and Computing*. 1980, vol. 18, issue 6, pp. 709-718.

BHATTACHARYA-GHOSH, Benjamin, Silvia SCHIEVANO, and Vanessa DÍAZ-ZUCCARINI. A multi-physics and multi-scale lumped parameter model of cardiac contraction of the left ventricle: A conceptual model from the protein to the organ scale. *Computers in Biology and Medicine* [online]. 2012, vol. 42, issue 10, pp. 982-992 [cit. 2015-05-10]. DOI: 10.1016/j.compbiomed.2012.07.010.

BOVENDEERD, Peter H. M., Petra BORSJE, Theo ARTS, and Frans N. van De VOSSE. Dependence of Intramyocardial Pressure and Coronary Flow on Ventricular Loading and Contractility: A Model Study. *Annals of Biomedical Engineering* [online]. 2006, vol. 34, issue 12, pp. 1833-1845 [cit. 2015-05-10]. DOI: 10.1007/s10439-006-9189-2.

CARUEL, Matthieu, Radomir CHABINIOK, Philippe MOIREAU, Yves LECARPENTIER, and Dominique CHAPELLE. Dimensional Reduction of Cardiac Models for Effective Validation and Calibration. In: *Proceedings of the 7th International Conference, FIMH 2013*, London, UK, June 20-22, 2013, pp. 259-267. DOI: 10.1007/978-3-642-38899-6_31.

CENTERS FOR DISEASE CONTROL AND PREVENTION. Heart Disease Facts. 2015. *Centers for Disease Control and Prevention: CDC 24/7: Saving Lives, Protecting People* [online]. [cit. 2015-05-10]. Available from: http://www.cdc.gov/HeartDisease/facts.htm

COMBES, Alain, Matthew BACCHETTA, Daniel BRODIE, Thomas MÜLLER, and Vince PELLEGRINO. Extracorporeal membrane oxygenation for respiratory failure in adults. *Current Opinion in Critical Care* [online]. 2012, vol. 18, issue 1, pp. 99-104 [cit. 2015-05-10]. DOI: 10.1097/mcc.0b013e32834ef412.

CHAPELLE, Dominique, Miguel A. FERNÁNDEZ, Jean-Frédéric GERBEAU, Philippe MOIREAU, Jacques SAINTE-MARIE, and Nejib ZEMZEMI. Numerical Simulation of the Electromechanical Activity of the Heart. In: *Proceedings of the 5th International Conference, FIMH 2009*, Nice, France, June 3-5, 2009, pp. 357-365. DOI: 10.1007/978-3-642-01932-6_39.

DASSEN, Willem, Theo ARTS, Peter M. van DAM, Nico HL KUIJPERS, Evelien HERMELING, Eelco M. van DAM, and Tammo DELHAAS. The application of complex research simulation models in education; A generic approach. In: *Proceedings of Computing in Cardiology, 2011,* pp. 465-468.

DESERRANNO, Dimitri, Mohammad KASSEMI, and James D. THOMAS. Incorporation of Myofilament Activation Mechanics into a Lumped Model of the Human Heart. *Annals of Biomedical Engineering* [online]. 2007, vol. 35, issue 3, pp. 321-336 [cit. 2015-05-10]. DOI: 10.1007/s10439-006-9234-1.

FERRARI, G., A. NICOLETTI, C. De LAZZARI, F. CLEMENTE, G. TOSTI, M. GUARANGO, R. MIMMO, D. AMBROSI, and K. GORCZYNSKA. A physical model of the human systemic arterial tree. *International Journal of Artificial Organs*. 2000, vol. 23, issue 9, pp. 647-657.

FINCKE, Rupert, Judith S. HOCHMAN, April M. LOWE, Venu MENON, James N. SLATER, John G. WEBB, Thierry H. LEJEMTEL, and Gad COTTER. Cardiac power is the strongest hemodynamic correlate of mortality in cardiogenic shock: A report from the SHOCK trial registry. *Journal of the American College of Cardiology* [online]. 2004, vol. 44, issue 2, pp. 340-348 [cit. 2015-05-10]. DOI: 10.1016/j.jacc.2004.03.060.

GHOSH, Subrata, Satyajit SAHU, and Anirban BANDYOPADHYAY. Evidence of massive global synchronization and the consciousness. *Physics of Life Reviews* [online]. 2014, vol. 11, issue 1, pp. 83-84 [cit. 2015-05-10]. DOI: 10.1016/j.plrev.2013.10.007.

GU, Y. J., P. W. BOONSTRA, R. GRAAFF, A. A. RIJNSBURGER, H. MUNGROOP, and W. van OEVEREN. Pressure Drop, Shear Stress, and Activation of Leukocytes During Cardiopulmonary Bypass: A Comparison Between Hollow Fiber and Flat Sheet Membrane Oxygenators. *Artificial Organs* [online]. 2000, vol. 24, issue 1, pp. 43-48 [cit. 2015-05-10]. DOI: 10.1046/j.1525-1594.2000.06351.x.

HUXLEY, Hugh E. Fifty years of muscle and the sliding filament hypothesis. *European Journal of Biochemistry* [online]. 2004, vol. 271, issue 8, pp. 1403-1415 [cit. 2015-05-10]. DOI: 10.1111/j.1432-1033.2004.04044.x.

INSTITUTE OF PATHOLOGICAL PHYSIOLOGY, CHARLES UNIVERSITY IN PRAGUE. Physiolibrary: Modelica library for Physiology. 2015. *Physiolibrary* [online]. [cit. 2015-05-10]. Available from: http://www.physiolibrary.org/

JAGER, Gerard N., Nico WESTERHOF, and Abraham NOORDERGRAAF. Oscillatory flow impedance in electrical analog of arterial system: representation of sleeve effect and non-Newtonian properties of blood. *Circulation research*. 1965, vol. 16, issue 2, pp. 121-133.

KAYE, David, Sanjiv J. SHAH, Barry A. BORLAUG, Finn GUSTAFSSON, Jan KOMTEBEDDE, Spencer KUBO, Chris MAGNIN, Mathew S. MAURER, Ted FELDMAN, and Daniel BURKHOFF. Effects of an Interatrial Shunt on Rest and Exercise Hemodynamics: Results of a Computer Simulation in Heart Failure. *Journal*

of Cardiac Failure [online]. 2014, vol. 20, issue 3, pp. 212-221 [cit. 2015-05-10]. DOI: 10.1016/j.cardfail.2014.01.005.

KAWAHITO, Shinji, Tadashi MOTOMURA, Julie GLUECK, and Yukihiko NOSÉ. Development of a new hollow fiber silicone membrane oxygenator for ECMO: The recent progress. *Annals of thoracic and cardiovascular surgery*. 2002, vol. 8, issue 5, pp. 268-274.

KIM, Young-Tae, Jeong Sang LEE, Chan-Hyun YOUN, Jae-Sung CHOI, and Eun Bo SHIM. An Integrative Model of the Cardiovascular System Coupling Heart Cellular Mechanics with Arterial Network Hemodynamics. *Journal of Korean Medical Science* [online]. 2013, vol. 28, issue 8 [cit. 2015-05-10]. DOI: 10.3346/jkms.2013.28.8.1161.

KLABUNDE, Richard E. Stroke Work and Cardiac Work, 2014. *Cardiovascular Physiology Concepts* [online]. [cit. 2015-05-10]. Available from: http://cvphysiology.com/Cardiac%20Function/CF019.htm

KO, Wen-Je, Ching-Yuang LIN, Robert J CHEN, Shoei-Shen WANG, Fang-Yue LIN, and Yih-Sharng CHEN. Extracorporeal membrane oxygenation support for adult postcardiotomy cardiogenic shock. *The Annals of Thoracic Surgery*. 2002, vol. 73, issue 2, pp. 538-545. DOI: 10.1016/S0003-4975(01)03330-6. ISSN 00034975.

KRISHNA, Murli, and Kai ZACHAROWSKI. Principles of intra-aortic balloon pump counterpulsation. *Continuing Education in Anaesthesia, Critical Care & Pain* [online]. 2009, vol. 9, issue 1, pp. 24-28 [cit. 2015-05-10]. DOI: 10.1093/bjaceaccp/mkn051.

LANG, C. C., P. KARLIN, J. HAYTHE, T. K. LIM, and D. M. MANCINI. Peak Cardiac Power Output, Measured Noninvasively, Is a Powerful Predictor of Outcome in Chronic Heart Failure. *Circulation: Heart Failure* [online]. 2009, vol. 2, issue 1, pp. 33-38 [cit. 2015-05-10]. DOI: 10.1161/circheartfailure.108.798611.

LUMENS, Joost, Tammo DELHAAS, Borut KIRN, and Theo ARTS. Modeling Ventricular Interaction: A Multiscale Approach From Sarcomere Mechancis To Cardiovascular Systém Hemodynamics. In: *Biocomputing 2008 - Proceedings of the Pacific Symposium* [online]. 2008 [cit. 2015-05-10]. DOI: 10.1142/9789812776136_0037.

LUMENS, Joost, Tammo DELHAAS, Borut KIRN, and Theo ARTS. Three-Wall Segment (TriSeg) Model Describing Mechanics and Hemodynamics of Ventricular Interaction. *Annals of Biomedical Engineering* [online]. 2009, vol. 37, issue 11, pp. 2234-2255 [cit. 2015-05-10]. DOI: 10.1007/s10439-009-9774-2.

MAASTRICHT UNIVERSITY – DEPARTMENT OF BIOMEDICAL ENGINEERING. Downloads - CircAdapt: learning cardiovascular physiology. *CircAdapt: Advanced cardiovascular modeling and simulation* [online]. 2013 [cit. 2015-05-10]. Available from: http://www.circadapt.org/downloads

MENDOZA, Dorinna D., Howard A. COOPER, and Julio A. PANZA. Cardiac power output predicts mortality across a broad spectrum of patients with acute cardiac disease. *American Heart Journal* [online]. 2007, vol. 153, issue 3, pp. 366-370 [cit. 2015-05-10]. DOI: 10.1016/j.ahj.2006.11.014.

MEURS, Willem van. *Modeling and simulation in biomedical engineering: applications in cardiorespiratory physiology*. Ed. 1. New York: McGraw-Hill, 2011, xx, 193 p. ISBN 9780071714457.

MIRZAEE, Mohammad Reza, Omid GHASEMALIZADEH, and Bahar FIROOZABADI. Exact Simulating of Human Arteries using Lumped Model and Probing Constriction in Femoral and Carotid Arteries.

American Journal of Applied Sciences [online]. 2009, vol. 6, issue 5, pp. 834-842 [cit. 2015-05-10]. DOI: 10.3844/ajassp.2009.834.842.

MORLEY, Deborah, Kenneth LITWAK, Paul FERBER, Paul SPENCE, Robert DOWLING, Bart MEYNS, Bartley GRIFFITH, and Daniel BURKHOFF. Hemodynamic effects of partial ventricular support in chronic heart failure: Results of simulation validated with in vivo data. *The Journal of Thoracic and Cardiovascular Surgery* [online]. 2007, vol. 133, issue 1, 21-28.e4 [cit. 2015-05-10]. DOI: 10.1016/j.jtcvs.2006.07.037.

MYNARD, J. P., M. R. DAVIDSON, D. J. PENNY, and J. J. SMOLICH. A simple, versatile valve model for use in lumped parameter and one-dimensional cardiovascular models. *International Journal for Numerical Methods in Biomedical Engineering*. 2012, vol. 28, issue 6-7, pp. 626-641. DOI: 10.1002/cnm.1466. ISSN 20407939.

NAIK, Ketan B., and P. H. BHATHAWALA. Mathematical Modelling and Simulation of Human Systemic Arterial System. *International Journal of Engineering and Innovative Technology*. 2014, vol. 4, issue 1. ISSN 2277-3754.

NICHOLS, Melanie, Nick TOWNSEND, Peter SCARBOROUGH, and Mike RAYNER. Cardiovascular disease in Europe 2014: epidemiological update. *European Heart Journal* [online]. 2014, vol. 35, issue 42, pp. 2950-2959 [cit. 2015-05-10]. DOI: 10.1093/eurheartj/ehu299.

NORDSLETTEN, D.A., S.A. NIEDERER, M.P. NASH, P.J. HUNTER, and N.P. SMITH. Coupling multi-physics models to cardiac mechanics. *Progress in Biophysics and Molecular Biology* [online]. 2011, vol. 104, 1-3, pp. 77-88 [cit. 2015-05-10]. DOI: 10.1016/j.pbiomolbio.2009.11.001.

NORTON, James M. Toward consistent definitions for preload and afterload. *Advances in physiology education*. 2001, vol. 25, issue 1, pp. 53-61.

O'ROURKE, Michael F., and Albert P. AVOLIO. Pulsatile flow and pressure in human systemic arteries. Studies in man and in a multibranched model of the human systemic arterial tree. *Circulation Research*. 1980, vol. 46, issue 3, pp. 363-372.

OLUFSEN, Mette S., and Ali NADIM. On deriving lumped models for blood flow and pressure in the systemic arteries. *Mathematical Biosciences and Engineering*. 2004, vol. 1, issue 1, pp. 61-80.

PETTERSEN, Klas H., Scott M. BUGENHAGEN, Javaid NAUMAN, Daniel A. BEARD, Stig W. OMHOLT, and Feilim MAC GABHANN. Arterial Stiffening Provides Sufficient Explanation for Primary Hypertension. *PLoS Computational Biology*. 2014, vol. 10, issue 5, e1003634. DOI: 10.1371/journal.pcbi.1003634. ISSN 1553-7358.

PIRONET, Antoine, Pierre C. DAUBY, Sabine PAEME, Sarah KOSTA, J. Geoffrey CHASE, Thomas DESAIVE, and Kelvin Kian Loong WONG. 2013. Simulation of Left Atrial Function Using a Multi-Scale Model of the Cardiovascular System. *PLoS ONE*, vol. 8, isstue 6, e65146. DOI: 10.1371/journal.pone.0065146. ISSN 1932-6203.

POKORNÝ, Martin, L. ČERVENKA, I. NETUKA, J. PIRK, M. KOŇAŘÍK, and J. MALÝ. Ventricular assist devices in heart failure: how to support the heart but prevent atrophy? *Physiological Research*. 2014, vol. 63, pp. 147-156.

ROYAL CHILDREN'S HOSPITAL – VICTORIAN PAEDIATRIC CARDIAC SURGICAL UNIT. Perfusion Unit: Extracorporeal Membrane Oxygenation Protocol. 2004, Melbourne, Australia.

SAHU, Satyajit, Subrata GHOSH, Daisuke FUJITA a Anirban BANDYOPADHYAY. Live visualizations of single isolated tubulin protein self-assembly via tunneling current: effect of electromagnetic pumping during spontaneous growth of microtubule. *Scientific Reports* [online]. 2014, vol. 4 [cit. 2015-05-10]. DOI: 10.1038/srep07303.

SCHAMPAERT, Stéphanie, Marcel C.M. RUTTEN, Marcel van 't VEER, Lokien X. van NUNEN, Pim A. L. TONINO, Nico H. J. PIJLS, and Frans N. van de VOSSE. Modeling the Interaction Between the Intra-Aortic Balloon Pump and the Cardiovascular System. *ASAIO Journal* [online]. 2013, vol. 59, issue 1, pp. 30-36 [cit. 2015-05-10]. DOI: 10.1097/mat.0b013e3182768ba9.

SEGERS, Patrick, N. STERGIOPULOS, Pascal VERDONCK, and Ronny VERHOEVEN. Assessment of distributed arterial network models. *Medical and Biological Engineering and Computing*. 1997, vol. 35, issue 6, pp. 729-736.

SHI, Yubing, Patricia LAWFORD, and Rodney HOSE. Review of Zero-D and 1-D Models of Blood Flow in the Cardiovascular System. *BioMedical Engineering OnLine* [online]. 2011, vol. 10, issue 1 [cit. 2015-05-10]. DOI: 10.1186/1475-925x-10-33.

SHIM, Eun Bo, Hyung Min JUN, Chae Hun LEEM, Satoshi MATUSUOKA, and Akinori NOMA. A new integrated method for analyzing heart mechanics using a cell–hemodynamics–autonomic nerve control coupled model of the cardiovascular system. *Progress in Biophysics and Molecular Biology* [online]. 2008, vol. 96, 1-3, pp. 44-59 [cit. 2015-05-10]. DOI: 10.1016/j.pbiomolbio.2007.07.015.

STERGIOPULOS, Nikos, Berend E. WESTERHOF, and Nico WESTERHOF. Total arterial inertance as the fourth element of the windkessel model. *American Journal of Physiology-Heart and Circulatory Physiology*. 1999, vol. 276, issue 1, pp. H81-H88.

TALBOT, Hugo, Stéphanie MARCHESSEAU, Christian DURIEZ, Maxime SERMESANT, Stéphane COTIN, and Hervé DELINGETTE. Towards an interactive electromechanical model of the heart. *Interface Focus* [online]. 2013, vol. 3, issue 2 [cit. 2015-05-10]. DOI: 10.1098/rsfs.2012.0091.

TOBON-GOMEZ, Catalina, Georgina PALAU-CABALLERO, Marta SITGES, and Bart H. BIJNENS. Exercise Induced Inter-individual Variation of Right Ventricular Pressures: Simulations Using a Modular Model of the Cardiovascular System. In: *Statistical Atlases and Computational Models of the Heart. Imaging and Modelling Challenges – Third International Workshop, STACOM 2012, Held in Conjunction with MICCAI 2012*, Nice, France, October 5, 2012, Revised Selected Papers, pp. 336-344. DOI: 10.1007/978-3-642-36961-2_38.

VOSSE, Frans N. van de, and Nikos STERGIOPULOS. Pulse Wave Propagation in the Arterial Tree. *Annual Review of Fluid Mechanics* [online]. 2011, vol. 43, issue 1, pp. 467-499 [cit. 2015-05-10]. DOI: 10.1146/annurev-fluid-122109-160730.

WANG, J. J., and K. H. PARKER. Wave propagation in a model of the arterial circulation. *Journal of Biomechanics* [online]. 2004, vol. 37, issue 4, pp. 457-470 [cit. 2015-05-10]. DOI: 10.1016/j.jbiomech.2003.09.007.

WIKIMEDIA FOUNDATION. Starling RAP combined. 2010. *Wikimedia Commons: the free media repository* [online]. San Francisco (CA): Wikimedia Foundation [cit. 2015-05-10]. Available from: http://commons.wikimedia.org/wiki/File:Starling_RAP_combined.svg

WORLD HEALTH ORGANIZATION. Cardiovascular diseases: Data and statistics. 2015. *World Health Organization / Europe* [online]. [cit. 2015-05-10]. Available from: http://www.euro.who.int/en/health-topics/noncommunicable-diseases/cardiovascular-diseases/data-and-statistics

Appendix I: CLASS DIAGRAM OF COMPONENTS

In the following two pages, you can see a simplified class diagram (halved along the vertical axis) for the main package with components (packages Settings, Types, and Constants are not included).

Classes are represented by the little blocks framed within packages. Links with closed-capped arrows denote inheritance, links with open-capped arrows specify association (or composition, respectively). Note the multiple inheritance, which is permitted in Modelica (although it leads to a less clear organization of the diagram).

Class Diagram of Components

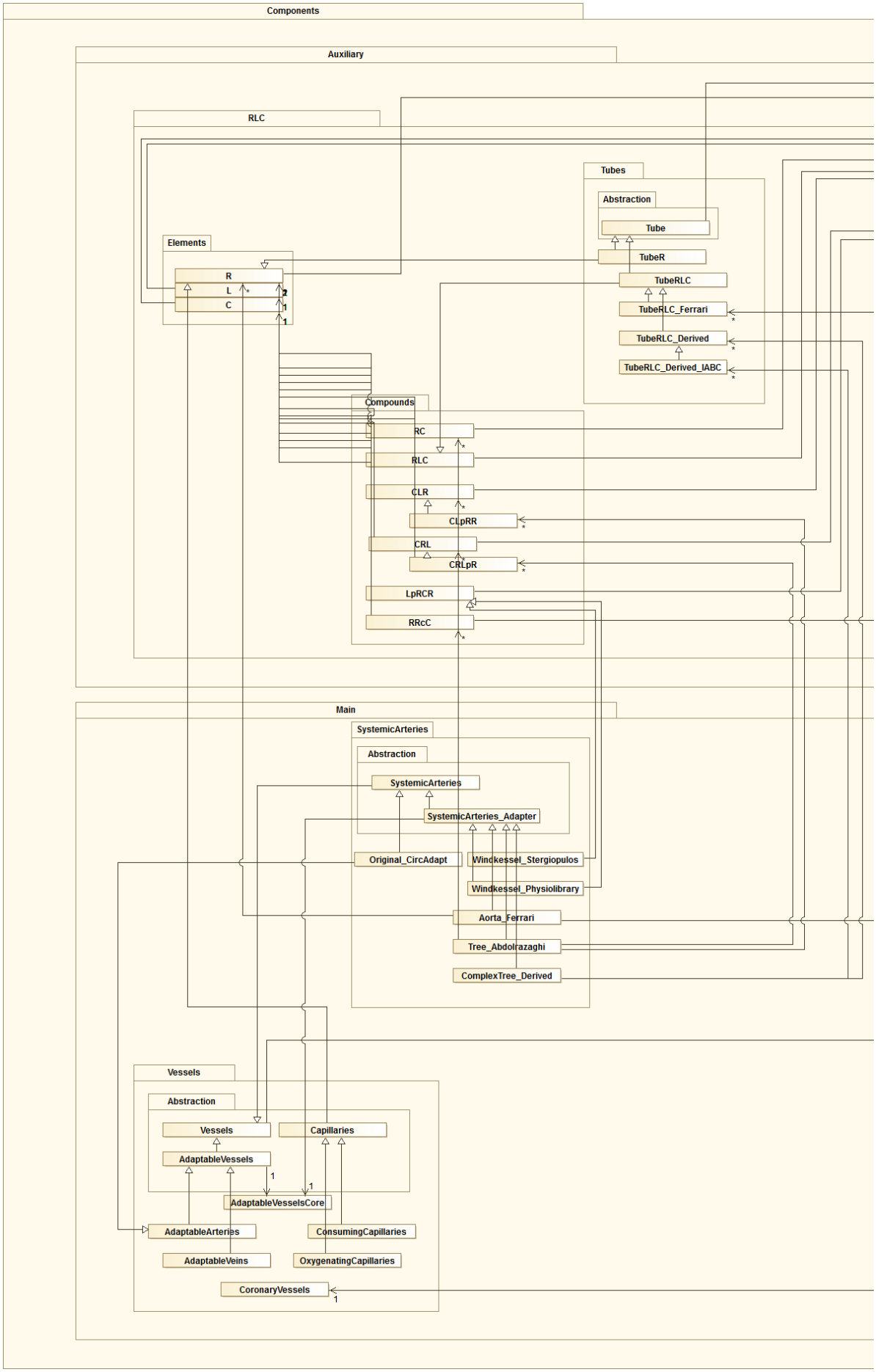

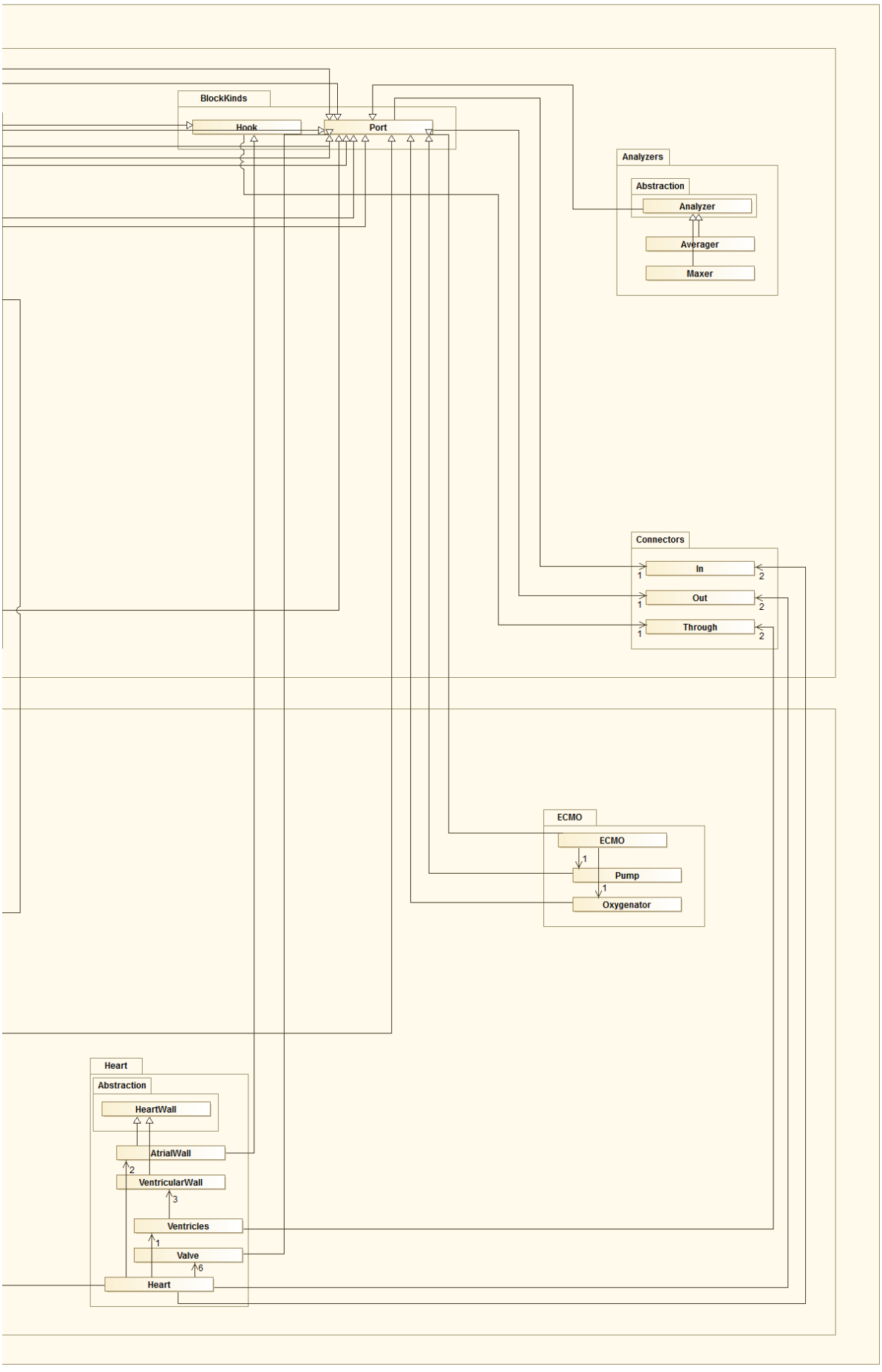
BlockKinds
Hook
Port
Analyzers
Abstraction
Analyzer
Averager
Maxer
Connectors
In
Out
Through
ECMO
ECMO
Pump
Oxygenator
Heart
Abstraction
HeartWall
AtrialWall
VentricularWall
Ventricles
Valve
Heart

Appendix II: DVD CONTENT

The DVD distributed along with this document contains:

- **Electronic copy of this thesis**
  "*Karel Kalecký – Relationship of Heart's Pumping Function and Pressure-Flow Patterns in Reduced Arterial Tree (2015).pdf*"
- **Complete version of the model Cardio**
  "*Cardio\Cardio.mo*"
- **Model documentation in the HTML Format** – contains class hierarchy, description of all elements and parameters including default values
  "*Cardio\Documentation**" (index "*Cardio.html*")
- **Simulated data** – data files with results of performed experiments
  "*Cardio\Data**"

Appendix III: Auxiliary Script for Adapted Values

The following script has been used to automatically extract adapted values from a data file generated with Dymola 2014 and translate them into a new Modelica class for initialization:

```
function GenerateInitialization (inputFile, outputFile)

    data = load (inputFile, 'name', 'data_2', 'dataInfo');
    names = cellstr (data. name);
    mapping = data. dataInfo (:, 2);
    data = data. data_2;
    [~, className, ~] = fileparts (outputFile);
    OutputSingle = @OutputSingleStart;

    file = fopen (outputFile, 'w');
    fprintf (file, 'record %s\r\n  extends Original(\r\n', className);
    OutputSet ({'SA', 'SV', 'PA', 'PV'}, {'pRef', 'ARef', 'AW'},
'%s.core.%s', '%s_%s');
    OutputSet ({'SC', 'PC'}, {'R'}, '%s.%s', '%s_%s');
    OutputSet ({'vLAV', 'vRAV', 'vSA', 'vPA', 'vSV', 'vPV'}, {'ARef'},
'heart.%s.%s', '%s_%s');
    OutputSet ({'RA', 'LA'}, {'AmRef', 'Am0', 'VW', 'sigmaPRef'},
'heart.%s.%s', '%s_%s');
    OutputSet ({'LW', 'SW', 'RW'}, {'AmRef', 'Am0', 'VW', 'sigmaPRef',
'EAmRef'}, 'heart.ventricles.%s.%s', '%s_%s');
    OutputSingle ('heart.VPRef', 'peri_VRef');
    fprintf (file, ');\r\nend %s;', className);
    fclose (file);

    function OutputSet (components, variables, inputFormat, outputFormat)
        try
            for component = components
                for variable = variables
                    OutputSingle (sprintf (inputFormat, component{:},
variable{:}), sprintf (outputFormat, component{:}, variable{:}));
                end
            end
        catch
        end
    end

    function OutputSingleStart (inputName, outputName)
        fprintf (file, '    %s = %d', outputName, data (end, mapping
(strncmp (inputName, names, length (inputName) + 1))));
        OutputSingle = @OutputSingleContinue;
    end
    function OutputSingleContinue (inputName, outputName)
        fprintf (file, ',\r\n    %s = %d', outputName, data (end, mapping
(strncmp (inputName, names, length (inputName) + 1))));
    end

end
```